Ducted
Axisymmetric
Propulsor
Evaluation
(DuctAPE)
Theory Document

Judd Mehr
October 13, 2025

Table of Contents

List of Figures

List of Tables

Chapter 1
Preliminary Concepts

In this chapter, we cover various preliminary concepts that will show up or be referenced regularly in the rest of this work.

1.1 Fundamental Theorems, Relations, etc.

1.1.1 Stokes' Theorem

Sir George Gabriel Stokes' fundamental theorem for curls is that the integral of the curl of the vector field, $\boldsymbol{V}$ over some surface, $\mathcal{S}$, is equal to the line integral of the vector field around the boundary of the surface, $\delta\mathcal{S}$. Mathematically, this is stated as

$$\iint_{\mathcal{S}} \nabla \times \boldsymbol{V} \mathrm{d}^2\mathcal{S} = \oint_{\delta\mathcal{S}} \boldsymbol{V} \mathrm{d}s \tag{1.1}$$

1.1.2 Relationship between Velocity and Circulation

Another name for the curl of the velocity just seen in Stokes' theorem (in addition to vorticity) is the circulation density. Thus the left hand side of Stokes' theorem as written in equation (1.1) is equivalent to the circulation, Γ, on the surface:

$$\Gamma = \oint_{\delta\mathcal{S}} \boldsymbol{V} \mathrm{d}s \tag{1.2}$$

1.1.3 Kelvin's Circulation Theorem

William Thomson, 1st Baron Kelvin's circulation theorem (which can be taken from the general conservation of circulation) states that: In a barotropic (we often consider incompressible cases, a special case of a barotropic fluid), ideal (the special case here we typically consider is the inviscid case) fluid with conservative body forces (no Coriolis affect, shear stresses, turbulence, etc.), the circulation around a closed curve moving with the fluid (and enclosing the same fluid elements through time) remains constant with time. In perhaps more understandable terms, if you follow a closed contour over time (by following all the contents of the contour), the circulation of that contour stays constant as long as the fluid is, for our purposes, incompressible and inviscid. To state it mathematically, the material derivative of circulation is zero for an incompressible, inviscid fluid:

$$\frac{D\Gamma}{Dt} = \frac{\partial \Gamma}{\partial t} + \boldsymbol{V} \cdot \nabla \Gamma = 0. \tag{1.3}$$

1.1.4 Helmholtz's Vortex Theorems

Hermann von Helmholtz' three vortex theorems are commonly described as:

1. The strength of a vortex line is constant along its length.
2. A vortex line cannot end in a fluid; it must extend to the boundaries of the fluid or form a closed path.
3. A fluid element that is initially irrotational remains irrotational.

1.1.5 The Biot-Savart Law

Based on experiments by Jean-Baptiste Biot and Félix Savart, the Biot-Savart law describes the magnetic field induced by a constant electric current. Applied to aerodynamic applications, it describes the velocity induced by a filament of constant vorticity. A basic derivation of the Biot-Savart law is informative as we will see various pieces of it throughout this dissertation.

Let us begin by defining some vector potential, $\boldsymbol{\psi}$, such that[a]

[a] remembering the vector identity $\nabla \cdot \nabla \times \boldsymbol{\psi} = 0$.

$$\boldsymbol{V} = \nabla \times \boldsymbol{\psi}, \tag{1.4}$$

and

$$\nabla \cdot \boldsymbol{\psi} = 0, \tag{1.5}$$

or in other words, $\boldsymbol{\psi}$ is a divergence free vector field.[b]

[b] Therefore automatically satisfying continuity.

Next we take the definition of vorticity (**??**) and plug in our expression for $\boldsymbol{\psi}$:

$$\begin{aligned} \boldsymbol{\omega} &= \nabla \times \boldsymbol{V} \\ &= \nabla \times \left(\nabla \times \boldsymbol{\psi} \right) \\ &= \nabla \left(\nabla \cdot \boldsymbol{\psi} \right) - \nabla^2 \boldsymbol{\psi} \quad \text{(vector identity)}. \end{aligned} \tag{1.6}$$

Since we defined $\boldsymbol{\psi}$ to be divergence free (see equation (1.31)), our expression for vorticity simplifies to the Poisson equation

$$\boldsymbol{\omega} = -\nabla^2 \boldsymbol{\psi}. \tag{1.7}$$

We can apply a Green's function in order to solve for $\boldsymbol{\psi}$ in three dimensions, where the known Green's function[c] takes the form of

[c] See nearly any math text covering partial differential equation solution methods.

$$\mathcal{G} = \frac{-1}{4\pi |\boldsymbol{r}|}, \tag{1.8}$$

where $|\boldsymbol{r}| = |\boldsymbol{q} - \boldsymbol{s}|$ is the Euclidean distance from the point along the vortex filament of influence, $\boldsymbol{s}$, and the point of interest, $\boldsymbol{q}$. Applying this Green's function to the solution of $\boldsymbol{\psi}$ yields

$$\psi = \frac{1}{4\pi} \iiint_{\mathcal{V}} \frac{\boldsymbol{\omega}(\boldsymbol{q})}{|\boldsymbol{r}|} \mathrm{d}^3 s. \tag{1.9}$$

If we now apply equation (1.30), by taking the curl of equation (1.36), we arrive at the Biot-Savart law:

$$\begin{aligned} \boldsymbol{V} &= \nabla \times \frac{1}{4\pi} \iiint_{\mathcal{V}} \frac{\boldsymbol{\omega}(\boldsymbol{q})}{|\boldsymbol{r}|} \mathrm{d}^3 s \\ &= \frac{1}{4\pi} \iiint_{\mathcal{V}} \frac{\boldsymbol{\omega}(\boldsymbol{q}) \times \boldsymbol{r}}{|\boldsymbol{r}|^3} \mathrm{d}^3 s. \end{aligned} \tag{1.10}$$

1.1.6 Kutta-Joukowski Theorem

The Kutta-Joukowski theorem, name for Martin Kutta and Nikolai Zhukovsky, relates circulation, $\boldsymbol{\Gamma}$, and velocity, $\boldsymbol{V}$, to the force generated, which is lift, $\boldsymbol{L}$, (due to being the force perpendicular to the flow by definition).

$$\boldsymbol{L} = \rho_\infty \boldsymbol{V} \times \boldsymbol{\Gamma} \tag{1.11}$$

where ρ_∞ is the freestream density.

1.2 Numerical Integration (quadrature)

In general, quadrature is a process by which the calculus problem of determining the integral of a curve is cast as a linear algebra problem whereby a weighted sum of intelligently chosen samples approximates the true value of the integral.

$$\int_a^b f(x) \mathrm{d}x \approx \sum_{k=1}^{N} w_k f(x_k) \tag{1.12}$$

where the main task of the any quadrature method is to decide where along the integration interval to place the sample points, x_k, and what weights, w_k, to apply to those samples. Undergraduate calculus and numerical methods courses often cover rectangle, trapezoid, and simpson's quadrature schemes, and will therefore not be covered here. We will focus on the basics of Gauss-Legendre quadrature, a powerful method allowing the exact approximation of polynomial functions.

1.2.1 Basic Theory of Gauss-Legendre quadrature

In Gauss-Legendre quadrature, we obtain the abscissae at which we sample the curve in question using points derived from the Legendre polynomials, and weights chosen wisely to get the best possible approximation given a certain number of degrees of freedom.

Legendre polynomials

Legendre polynomials are a set of polynomials forming a basis of the polynomial space up to degree n, where n is the order of the highest order polynomial in the set. To obtain the Legendre polynomials we start with the orthogonal set:

$$\{1, x, x^2, \ldots, x^n\}; \tag{1.13}$$

and through the Gram-Schmidt orthogonalization process, with respect to the inner product,

$$\langle p, q \rangle = \int_{-1}^{1} p(x)q(x)\mathrm{d}x, \tag{1.14}$$

we obtain a new set of orthogonal polynomials that spans the same function space. We then apply constant scalings to the polynomials so that $p_n(1) = 1$. These polynomials (scaling included) can also be calculated using Rodrigues' formula:

$$p_n(x) = \frac{1}{2^n n!} \frac{\mathrm{d}^n}{\mathrm{d}x^n} \left(x^2 - 1\right)^n. \tag{1.15}$$

Legendre polynomials have several attractive properties. Here we mention just a few that will be shown to be important momentarily. First, Legendre polynomials of degree n have exactly n real roots. Second, all the roots of Legendre polynomials fall in the range $(-1, 1)$.

Gaussian Weights

Given a polynomial, $p(x)$, of degree $2n - 1$, we express $p(x)$ in terms of a polynomial division:

$$p(x) = q(x)L_n(x) + r(x), \tag{1.16}$$

where $L_n(x)$ is the nth degree Legendre polynomial, and $q(x)$ is some polynomial of degree $\leq n - 1$; and $r(x)$ is the remainder of the division of q and L and is also of degree $\leq n - 1$. Integrating, we have

$$\int_{-1}^{1} p(x)\mathrm{d}x = \int_{-1}^{1} q(x)L_n(x)\mathrm{d}x + \int_{-1}^{1} r(x)\mathrm{d}x. \tag{1.17}$$

Note that the definition of our inner product (equation (1.14)) has appeared. Because q and L are, by definition, orthogonal, this first term on the right side equals zero. We can therefore approximate the first term *exactly* by choosing the abscissae at which to sample the curve to be the roots of the Legendre polynomial of degree n which are all real and conveniently fall between the bounds of integration.

Next, we can also approximate the second term on the right side *exactly* by intelligently choosing weights. With n degrees of freedom, we can approximate exactly any polynomial of order $\leq n - 1$ (noting that the order of r is $n - 1$). We do this by applying the Vandermonde matrix in this manner:

$$\begin{bmatrix} 1 & 1 & \dots & 1 \\ x_1 & x_2 & \dots & x_n \\ x_1^2 & x_2^2 & \dots & x_n \\ \vdots & \vdots & \vdots & \vdots \\ x_1^{n-1} & x_2^{n-1} & \dots & x_n^{n-1} \end{bmatrix} \begin{bmatrix} w_1 \\ w_2 \\ w_3 \\ \vdots \\ w_n \end{bmatrix} = \begin{bmatrix} 2 \\ 0 \\ \frac{2}{3} \\ \vdots \\ \int_{-1}^{1} x^{n-1} \end{bmatrix} \tag{1.18}$$

where x_n are the nth roots of the nth degree Legendre polynomial, w_n is the nth weighting value, and the right hand side are the true values of the integrals with bounds $[-1, 1]$ from degree zero up to $n-1$.

We can also calculate the weights using the following formula:

$$w_i = \frac{2(1-x_i^2)}{(n+1)^2[p_{n+1}(x_i)]^2}, \tag{1.19}$$

where again x_i are the roots of the nth degree Legendre polynomial. Thus with the intelligent choice of both abscissae and weights, we can approximate *exactly* any polynomial of degree $2n-1$ with only n points. This is the power of Gaussian quadrature.

Transforming the Bounds of Integration

Above we have shown that the integral of any polynomial of degree $2n-1$ with bounds $[-1, 1]$ can be approximated exactly using n points. With a simple transformation, we can evaluate the integral with arbitrary bounds $[a, b]$ in the following manner:

$$\int_a^b f(x)\mathrm{d}x \approx \frac{b-a}{2} \sum_{i=1}^{n} w_n f(\xi_n). \tag{1.20}$$

where

$$\xi_n = \frac{b-a}{2} x_n + \frac{a+b}{2}. \tag{1.21}$$

1.2.2 Application to Strongly Singular Integrals

When applying quadrature to boundary element methods (as will be done in this dissertation), we often find ourselves evaluating singular integrals. Even though evaluating strongly singular integrals is impossible directly, we can get a very good approximation by evaluating the Cauchy principal value using a subtraction of singularity technique. The definition with the Cauchy principal value denoted by $⨍$ is given as

$$⨍_\Gamma f(s)\mathrm{d}s = \lim_{\varepsilon \to 0^+} \left[\int_{s_i}^{s_p-\varepsilon} f(s)\mathrm{d}s + \int_{s_p+\varepsilon}^{s_f} f(s)\mathrm{d}s \right]. \tag{1.22}$$

As we can see, this allows us to approximate the integral over a range Γ from s_i to s_f with a singularity present at s_p where s are curvilinear abscissae along a curve, Γ.

The main thrust of the subtraction of singularity technique is to subtract from the integrand the value at its singular point and then add

an analytic solution for the singular point back on to the final integral. In the general case, we could take a function, $G(s)/s$, which is singular at the point $s = 0$, and re-write it as

$$\frac{G(s)}{s} = \frac{G(s) - G(0)}{s} + \frac{G(0)}{s} \tag{1.23}$$

Then, having removed the singularity from the first term, we could integrate the first term numerically using techniques covered earlier in this section. We could also integrate analytically (or determine an analytic approximation for) the integral of the singular second term, and add the results together:

$$\oint_{s_i}^{s_f} \frac{G(s)}{s} \mathrm{d}s \approx \int_{s_i}^{s_f} \frac{G(s) - G(0)}{s} \mathrm{d}s + G(0) \log \left| \frac{s_f}{s_i} \right| \tag{1.24}$$

In practice, the integrand may not be as simple as the general case shown here, but as long as the singular parts of the integral can be subtracted out and analytically evaluated, this subtraction of singularity method is easily applied.

1.3 Potential Flow Theory

The vortex methods developed and/or used in this work are built on concepts rooted in potential flow theory. Potential flow theory deals with the analysis of flow fields that are simplified representations of real fluid flows. The simplifications only approximate real flows, but allow for much better computational efficiency than high fidelity computational fluid dynamic methods. Despite the approximate nature of potential flow fields, there are many realistic cases in which the approximation is quite good. In this section we will cover the basics of potential flow theory and introduce several elementary flows used in this work upon which we will continue to build the concepts underpinning the analysis methods of this work.

Potential flow refers to velocity fields that can be expressed as the gradient of a scalar function called the velocity potential,[d] ϕ:

[d] Thus the name potential flow theory

$$\boldsymbol{V} = \nabla\phi. \tag{1.25}$$

Do define the velocity in terms of a scalar potential, we require the field to differentiable and irrotational.

Assumption 1.1

The velocity field is irrotational, such that

$$\boldsymbol{\omega} = \nabla \times \boldsymbol{V} = 0$$

everywhere in the field except for the axes of free vortices.

Limitations: We cannot directly model viscous effects in the flow such as boundary layers and viscous wake phenomena .

Justification: For the ranges of Reynolds numbers seen in this work, the majority of the flow field is accurately approximated as inviscid.

Here, ω represents the vorticity, which is the curl of the velocity vector. The assumption of irrotational flow by definition results in inviscid flow.[e] For this work, we will work with incompressible potential flow theory, which also requires an assumption of incompressible flow.

[e] An irrotational flow is always inviscid, but an inviscid flow is not necessarily irrotational

Assumption 1.2

The velocity field is incompressible, such that

$$\nabla \cdot \boldsymbol{V} = 0.$$

Limitations: This excludes highly compressible flows, such as those with strong shocks or Mach numbers well above 0.3.

Justification: In the external aerodynamics analyses in this work, the Mach number is low enough that density changes are negligible.

Substituting in the definition of velocity from equation (1.25) into the expression in assumption 1.2, we get:

$$\nabla \cdot \nabla\phi = \nabla^2\phi = 0, \tag{1.26}$$

which is the Laplace equation. Along with the implication of assumption 1.1 that our flow is inviscid, the fact that the Laplace equation is a linear operator is a major key to the reduction in required computational expense for potential flow methods. Because the Laplace equation is a linear operator, we can model relatively complicated flow features (such as a duct and center body) using a superposition of well-studied solutions to the Laplace equation. In an aerodynamic context, we call these solutions to the Laplace equation: elementary flows.

1.3.1 Elementary Flows

The following are a handful of useful elementary flows we will use in this work.

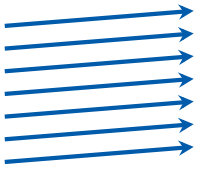

Uniform Flow

Uniform flow is precisely that, a flow that uniformly moves in a single direction without variation in the flow field. Often, the free stream is modeled as a uniform flow. Mathematically, we describe the potential of a uniform flow as

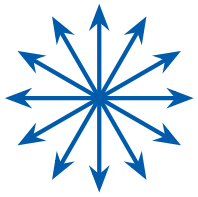

$$\phi_u = V_\infty \hat{r} \tag{1.27}$$

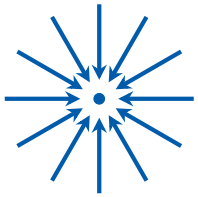

where V_∞ is the magnitude of the flow and $\hat{r}$ in a vector indicating the direction of the flow.

Source/Sink Flow

Source and sink flows are mathematically identical, with the exception of sign. The defining characteristics of these flows are that they have only radial, and no tangential, components, with sources oriented radially outward, and sinks oriented radially inward. Expressed mathematically, the velocity potential for source/sink flow is

$$\phi_s = \frac{\pm\Lambda}{2\pi}\ln(r) \tag{1.28}$$

where Λ is the strength of the source (positive) or sink (negative), and r is the radial distance from the origin of the source/sink.

Vortex Flow

The final elementary flow that we will discuss here is the free vortex. Vortex flow characteristics have the opposite characteristic of source/sink flows in that there is no radial, only tangential components to the flow. The mathematical expression for the free vortex velocity potential is:

$$\phi_v = \frac{\Gamma}{2\pi}\theta \tag{1.29}$$

where Γ is the vortex strength and θ is the polar angle.

1.4 The Biot-Savart Law

While potential flow theory is quite useful, on its own it is insufficient for most of the interesting external aerodynamic phenomena which typically require the presence of circulation to model things like lift. Circulation is a measure of vorticity[f] in a fluid volume. In order to incorporate the effects of vorticity into our irrotational potential flow field, we introduce the Biot-Savart law.

[f] see assumption 1.1

Based on experiments by Jean-Baptiste Biot and Félix Savart, the Biot-Savart law describes the magnetic field induced by a constant electric current. With a few changes in nomenclature from electro-magnetics to fluid dynamics, the Biot-Savart law describes the velocity induced by a filament of constant vorticity. In words, the Biot-Savart law tells us the magnitude and direction of the velocity induced at a field point from a give vortex filament in 3-D space. Figure 1.1 shows a visual example of this process and then we proceed with a quick derivation of the Biot-Savart law in a format that is useful for applications in this work.

To understand how vorticity induces velocity, we introduce a vector potential, $\boldsymbol{\psi}$, such that the curl of the vector potential is velocity:

$$\boldsymbol{V} = \nabla \times \boldsymbol{\psi}, \tag{1.30}$$

and the vector potential is defined on a divergence-free field (in other words, continuity is satisfied):

$$\nabla \cdot \boldsymbol{\psi} = 0. \tag{1.31}$$

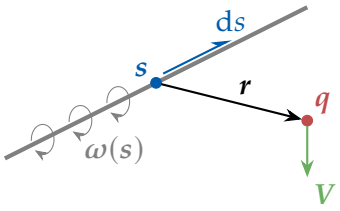

Figure 1.1: A vortex filament with a vorticity distribution $\boldsymbol{\omega}(\boldsymbol{s})$ induces a velocity at a field point, $\boldsymbol{q}$, from points, $\boldsymbol{s}$. The induced velocity is orthogonal to the filament vorticity and the vector $\boldsymbol{r} = \boldsymbol{q}$-$\boldsymbol{s}$ according to the right-hand rule.

Next we take the definition of vorticity (see assumption 1.1) and plug in our expression for $\boldsymbol{\psi}$:

$$\begin{aligned} \boldsymbol{\omega} &= \nabla \times \boldsymbol{V} \\ &= \nabla \times \left(\nabla \times \boldsymbol{\psi} \right) \end{aligned} \tag{1.32}$$

Applying a vector identity, we are left with:

$$\boldsymbol{\omega} = \nabla \left(\nabla \cdot \boldsymbol{\psi} \right) - \nabla^2 \boldsymbol{\psi}. \tag{1.33}$$

Since we defined $\boldsymbol{\psi}$ to be divergence free (see equation (1.31)), our expression for vorticity simplifies to the Poisson equation

$$\boldsymbol{\omega} = -\nabla^2 \boldsymbol{\psi}. \tag{1.34}$$

We can apply a Green's function in order to solve for $\boldsymbol{\psi}$ in three dimensions. For a source point, $\boldsymbol{s}$ along a vortex filament, and a field point, $\boldsymbol{q}$, being influenced, we use a well known Green's function[g] in terms of the vector from $\boldsymbol{s}$ to $\boldsymbol{q}$:

[g] See nearly any math text covering partial differential equation solution methods.

$$\mathcal{G} = \frac{-1}{4\pi |\boldsymbol{r}|}, \tag{1.35}$$

where $\boldsymbol{r} = \boldsymbol{q} - \boldsymbol{s}$ is the vector from the source point to the field point and $|\boldsymbol{r}|$ is the Euclidean distance from the point along the vortex filament of influence, $\boldsymbol{s}$, and the point of interest, $\boldsymbol{q}$. Applying this Green's function to the solution of $\boldsymbol{\psi}$ yields

$$\boldsymbol{\psi} = \frac{1}{4\pi} \iiint_{\mathcal{V}} \frac{\boldsymbol{\omega}(\boldsymbol{s})}{|\boldsymbol{r}|} \mathrm{d}^3 s. \tag{1.36}$$

where the integral is taken over a finite volume, or in our applications, a filament.

If we now apply equation (1.30), by taking the curl of equation (1.36), we arrive at

$$\boldsymbol{V} = \nabla \times \frac{1}{4\pi} \iiint_{\mathcal{V}} \frac{\boldsymbol{\omega}(\boldsymbol{s})}{|\boldsymbol{r}|} \mathrm{d}^3 s. \tag{1.37}$$

Applying the identity:

$$\nabla \times \frac{\boldsymbol{\omega}(\boldsymbol{s})}{|\boldsymbol{r}|} = \frac{\boldsymbol{\omega}(\boldsymbol{s}) \times \boldsymbol{r}}{|\boldsymbol{r}|^3} \tag{1.38}$$

where $\boldsymbol{\omega}(\boldsymbol{s})$ is constant relative to the differential operator, we arrive at an expression for the velocity induced at point $\boldsymbol{q}$ from a vortex filament integrated along s, in other words, the form of the Biot-Savart law especially useful in this work.

$$\boldsymbol{V} = \frac{1}{4\pi} \iiint_{\mathcal{V}} \frac{\boldsymbol{\omega}(\boldsymbol{s}) \times \boldsymbol{r}}{|\boldsymbol{r}|^3} \mathrm{d}^3 s. \tag{1.39}$$

This relationship between vorticity and induced velocity is foundational to nearly all of the aerodynamic analysis methods in this work, especially the vortex particle method and vortex panel method discussed in the next few chapters.

1.5 Optimization

Many of the studies in this dissertation involve the use of optimization techniques. In this section, we will cover the basics of the major concepts of the optimization techniques used in this dissertation.

1.5.1 Gradient-based Optimization

All of the optimization in this work is done with gradient-based optimization techniques. In general, gradient-based optimization can be described as any optimization method which utilizes the design space gradient in order to select which direction to search for the optimum. The main limitation of gradient-based methods is that they require differentiable design spaces. On the other hand, if the design space is differentiable, then gradient-based methods tend to be more efficient that gradient-free methods as problem size grows.

1.6 Automatic Differentiation

There are several modern tools that help in the implementation of gradient-based optimization methods. One such type of tool is automatic differentiation (AD), also called algorithmic differentiation among other names. AD allows for the computation of exact (relative to the function tolerance) derivatives through a given code, assuming the code is compatible with the AD tool being used.[h] The fundamental principle of AD is the application of the chain rule to composite functions in order to multiplicatively accumulate intermediate partial derivatives and obtain the final derivatives of the overall function outputs relative to the inputs.

[h] AD typically requires some up front development work to ensure that the code being differentiated is compatible with the AD tool being used. Such development work is part of the contributions of the work described in this dissertation as mentioned in **??**.

1.6.1 Forward-mode AD

There are several methods for obtaining derivatives with AD, one of which is known as forward-mode AD an was introduced as a computational method in 1964[1]. In forward-mode AD, we accumulate partial derivatives of expressions as we move forward through the computations. Any complex computational function is a composite of some number elementary functions with known derivatives. For a given function, $f(x_1, x_2, \ldots)$, the partial derivative of the output(s) with respect to an

1 Wengert, "A simple automatic derivative evaluation program," 1964.

input can be determined through the accumulation of partials through the chain rule. Written out, $\partial f / \partial x_i$ would be:

$$\begin{aligned}\frac{\partial f}{\partial x_i} &= \frac{\partial f}{\partial w_{n-1}} \frac{\mathrm{d}w_{n-1}}{\mathrm{d}x_i} \\ &= \frac{\partial f}{\partial w_{n-1}} \left(\frac{\partial w_{n-1}}{\partial w_{n-2}} \frac{\mathrm{d}w_{n-2}}{\mathrm{d}x_i} \right) \\ &= \frac{\partial f}{\partial w_{n-1}} \left(\frac{\partial w_{n-1}}{\partial w_{n-2}} \left(\frac{\partial w_{n-2}}{\partial w_{n-3}} \frac{\mathrm{d}w_{n-3}}{\mathrm{d}x_i} \right) \right) \\ &= \cdots ,\end{aligned} \tag{1.40}$$

where w_{n-j} indicate sub-functions of the composite function,

$$f(w_{n-1}(w_{n-2}(w_{n-3}(\ldots(x))))).$$

For multiple independent variables, we can generalize this process as the matrix products of Jacobians.

Dual Numbers

In practice, forward-mode AD is accomplished along side the nominal computations. This can be done when variables are defined as dual types which are based on dual numbers taking the form

$$a + b\epsilon, \tag{1.41}$$

where ϵ satisfies the condition $\epsilon^2 = 0$ where $\epsilon \neq 0$. In practice, we define a dual type that contains a primal (a) and partial (b) component, $\langle a, b \rangle$. For each elementary (addition, multiplication, trigonometric, exponential, logarithmic, etc.) operations, dual numbers are treated with an augmentation of the algebra of real numbers where the primal value of the dual is calculated with nominal arithmetic, and the partial component is calculated with first order differentiation. Thus the operations on the dual number type behave as:

$$f(a + b\epsilon) = f(a) + f'(a)b\epsilon. \tag{1.42}$$

1.6.2 ImplicitAD.jl

There are several shortcuts that can be used to make the computation of derivatives with AD more efficient[2]. The most-used of these in this work is implemented in the ImplicitAD.jl package[3], and is a method for obtaining the derivatives of the outputs of a solver without having to pass AD derivatives through the actual solver. This becomes especially advantageous for iterative solvers and large linear systems that would otherwise require a great deal of computational effort to obtain derivatives through every step using a direct method. In the following subsections, we follow closely the methodologies laid out by Ning *et al.* for efficiently obtaining derivatives of non-linear and linear system solves.

2 Martins *et al.*, *Engineering Design Optimization*, 2022.

3 Ning *et al.*, *Automating Steady and Unsteady Adjoints: Efficiently Utilizing Implicit and Algorithmic Differentiation*, 2023.

Non-linear Solves

We apply this AD shortcut to any non-linear system solver expressed in residual form as

$$r(x, y(x)) = 0 \tag{1.43}$$

where the function, r is the residual, y are the state variables, and x are the input variables. In the context of AD, we are looking for the derivatives

$$\dot{y} = \frac{\mathrm{d}y}{\mathrm{d}x}\dot{x}. \tag{1.44}$$

Applying the chain rule to equation (1.43) we see that

$$\frac{\mathrm{d}r}{\mathrm{d}x} = \frac{\partial r}{\partial x} + \frac{\partial r}{\partial y}\frac{\mathrm{d}y}{\mathrm{d}x} = 0, \tag{1.45}$$

which we rearrange to get

$$\frac{\mathrm{d}y}{\mathrm{d}x} = \left(\frac{\partial r}{\partial y}\right)^{-1}\frac{\partial r}{\partial x}. \tag{1.46}$$

Now we don't actually want to compute $\mathrm{d}y/\mathrm{d}x$ as this would require passing AD through all of the solver iterations, so we want to determine a way to obtain $\dot{y}$ in a shortcut manner. We will do so by first multiplying both sides of equation (1.45) by $\dot{x}$:

$$\begin{aligned}\frac{\partial r}{\partial y}\frac{\mathrm{d}y}{\mathrm{d}x}\dot{x} &= -\frac{\partial r}{\partial x}\dot{x},\\ \frac{\partial r}{\partial y}\dot{y} &= -\frac{\partial r}{\partial x}\dot{x}.\end{aligned} \tag{1.47}$$

For the right-hand side Jacobian vector product (JVP), $b = -(\partial r/\partial x)\dot{x}$, we can use the fact that it is equivalent to the directional derivative in the direction of $-\dot{x}$ and apply a single pass of forward-mode AD, using $-\dot{x}$ as the seed vector.[i]

With the right-hand side computed, we simply need to obtain $\partial r/\partial y$—which is either already available from the solver if it is a jacobian-based method, or can be had quickly with AD. We can then determine $\dot{y}$ through a linear solve of

$$\frac{\partial r}{\partial y}\dot{y} = b, \tag{1.48}$$

which is much more direct than attempting to pass AD through all of the solver iterations.

[i] In the actual implementation, a single evaluation of the residual at the converged solution y is done using the dual typed input, $x \equiv \langle x, \dot{x}\rangle$. Then b is set to be the partial of the result.

Linear Solves

For a given linear system, $Ay = b$ where A and/or b are functions of inputs, x, and have known derivatives, we can solve the system for y generally by

$$y = A^{-1}b \tag{1.49}$$

where we will want to solve for y by applying some factorization to A, say LU decomposition. To obtain a shortcut expression for the derivative, $\dot{y}$, we will start by applying the chain rule to equation (1.49):

$$\dot{y} = \dot{A}^{-1}b + A^{-1}\dot{b}. \tag{1.50}$$

Note that we already have $\dot{b}$ from AD at the time it was computed, so we just need $\dot{A}^{-1}$. If we take the definition of a matrix inverse, $AA^{-1} = I$, where I is the identity matrix, and differentiate both sides, we have

$$\dot{A}A^{-1} + A\dot{A}^{-1} = 0; \tag{1.51}$$

which we can solve for the derivative of the matrix inverse

$$\dot{A}^{-1} = -A^{-1}\dot{A}A^{-1}. \tag{1.52}$$

Substituting into equation (1.50) we have

$$\dot{y} = -A^{-1}\dot{A}A^{-1}b + A^{-1}\dot{b}; \tag{1.53}$$

where which we can simplify[j] to

[j] remembering that $y = A^{-1}b$.

$$\dot{y} = A^{-1}\left(\dot{b} - \dot{A}y\right). \tag{1.54}$$

Remembering that we already have y and a factorization for A^{-1} from the primal solve, as well as the values for $\dot{b}$ and $\dot{A}$ from AD at their original computation, we can easily compute the derivative, $\dot{y}$, without having to do more passes through the original linear system solve. This becomes more advantageous the larger the linear system becomes.

Chapter 1 References

1 Wengert, R. E., "A simple automatic derivative evaluation program," *Commun. ACM*, vol. 7, no. 8, August 1964, pp. 463–464. DOI: 10.1145/355586.364791 cited on p. 10

2 Martins, J. R. R. A. and Ning, A., *Engineering Design Optimization*. Cambridge University Press, January 2022. DOI: 10.1017/9781108980647 cited on p. 11

3 Ning, A. and McDonnell, T., *Automating Steady and Unsteady Adjoints: Efficiently Utilizing Implicit and Algorithmic Differentiation*, 2023.URL: https://arxiv.org/abs/2306.15243. cited on p. 11

4 Fredholm, I., "Sur une classe d'équations fonctionnelles," *Acta Mathematica*, vol. 27, no. none, 1903, pp. 365–390. DOI: 10.1007/bf02421317 cited on p. 15

cited on pp. 17–19

5 Lewis, R. I., *Vortex Element Methods for Fluid Dynamic Analysis of Engineering Systems*, ser. Cambridge engine technology series 1. Cambridge ; New York: Cambridge University Press, 1991.

6 Martensen, E., "Die Berechnung der Druckverteilung an dicken Gitterprofilen mit Hilfe von Fredholmschen Integralgleichungen zweiter Art," *Archive for Rational Mechanics and Analysis*, vol. 3, 1959, pp. 235–270. cited on pp. 17, 30

7 Courant, R. and Hilbert, D., *Methods of Mathematical Physics*. Interscience Publishers, 1962, vol. 2. cited on p. 17

A Vortex-based Axisymmetric Panel Method

Chapter 2

One of the major pieces of the DuctAPE solver is an axisymmetric panel method. The implementation for an axisymmetric panel method is similar to the implementation of typical planar panel methods, but there are a few differences. We include here details for the axisymmetric panel method used.

In section 1.3 we introduced potential flow theory. The elementary flows we introduced have limited use on their own, but in this chapter we will show how applying the theory beyond simple cases becomes a powerful tool in modeling the flow about aerodynamic bodies. As mentioned in section 1.3, the major key making potential flow theory particularly useful is the fact that elementary flows are solutions to the Laplace equation and can therefore be superimposed to represent relatively complex geometry. In particular, the superposition of any number of elementary flows of unknown strength can be assimilated into a single linear system of equations and the strengths can be solved for directly. In our application, we are mostly concerned with determining the strengths of elementary flows distributed along imaginary boundaries we define based on useful shapes (such as the surfaces of ducts and center bodies) that induce a potential flow field that matches what we would see for an actual solid body in reality.[a] We call problems dealing with values on boundaries boundary value problems (for obvious reasons). A common way to approach the solution of boundary value problem is with a boundary integral equation.

[a] In reality, flow is neither irrotational, nor incompressible, but we find that in many cases it is close enough that potential flow theory provides a good approximation.

2.1 Beyond the Basics of Potential Flow Theory: A Boundary Integral Equation

For a given aerodynamic body, representable by a simply connected contour (for example, S as shown in figure 2.1) we want to be able to find the velocity distribution on that body surface as well as its influence on the remainder of the flow field. To do so, we can construct a boundary integral equation describing the influence of distributions of elementary flows along a given boundary. We can then use this boundary integral equation with appropriate boundary conditions to solve the boundary value problem for the unknown distribution. Fortunately, Erik Ivar Fredholm developed a set of integral equations for application to boundary value problems[4]. For our application, we will use a Fredholm integral equation of the second kind:

4 Fredholm, "Sur une classe d'équations fonctionnelles," 1903.

$$f(t) = \vartheta(t) + \oint_{\mathcal{S}} K(s,t)\varphi(s)\mathrm{d}s. \tag{2.1}$$

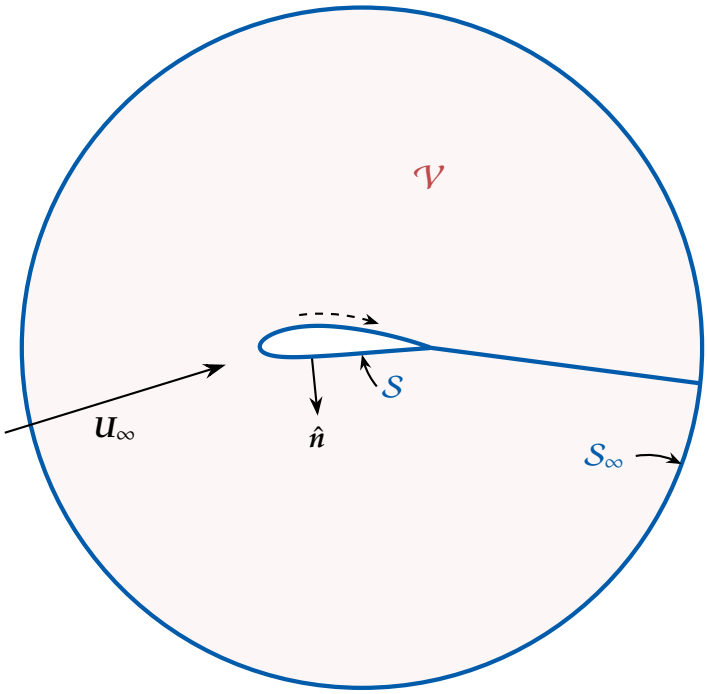

Figure 2.1: An example of a simply connected contour, $\mathcal{S}$, representing, in this case, an airfoil. The dashed arrow represent the direction about which the contour is traversed, with $\hat{\boldsymbol{n}}$ being the unit surface normal associated with the direction of travel.

We will construct this integral equation using vortex distributions and a Neumann boundary condition often referred to as the "no flow through" condition. We choose vortices since they inherently allow us to obtain circulation, and therefore lift about the bodies we model. In contrast sources do not provide the same benefit. A Neumann boundary condition is also not the only option, a Dirichlet condition could also be used, but the Neumann condition tends to be more intuitive and straightforward to apply. Given that context, let us look at each term individually. Starting with the integral term, which represents the influence of a distribution of elementary flows[b] along the boundary, we have the kernel K which in our case will be the expression for the unit induced velocities of vorticies distributed along the surface segment, $\mathrm{d}s$, acting normal to the surface at point t. Mathematically, we can state this as

[b] Such as those introduced in section 1.3

$$\begin{aligned} K(s,t) &= \frac{\partial \hat{\boldsymbol{\phi}}(s,t)}{\partial \hat{\boldsymbol{n}}_t} \\ &= \nabla \hat{\boldsymbol{\phi}}(s,t) \cdot \hat{\boldsymbol{n}}(t) \\ &= \hat{\boldsymbol{V}}(s,t) \cdot \hat{\boldsymbol{n}}(t). \end{aligned} \tag{2.2}$$

where $\hat{\boldsymbol{\phi}}$ is the unit velocity potential, $\hat{\boldsymbol{V}}$ is the unit velocity, and $\hat{\boldsymbol{n}}$ is the unit normal to the surface (see figure 2.1). The other term in the integrand, $\varphi(s)$, is the distribution of strengths of elementary flows along the boundary. As mentioned, we choose to use free vortices as our elementary flows and we represent their strengths with the symbol γ going forward.

The other term on the right hand side, $\vartheta(t)$ represents the jump in velocity across the boundary. It can be shown that the jump in tangential velocity associated with a vortex distribution along the boundary is $\vartheta(t) = -\gamma/2$.[5–7] And for the orthogonal case of the normal velocity (which we are concerned with at this point), the jump term is zero.

Lastly, the term on the left hand side, $f(t)$, represents any externally induced velocity in the negative normal direction[c] on the boundary at point t. The typical externally induced velocity is due to (but not limited to) a uniform free stream.[d] Mathematically we state the externally induced velocity as

$$\begin{aligned}\varphi(t) &= \frac{\partial \boldsymbol{\phi}_{\text{ext}}}{\partial \hat{\boldsymbol{n}}_t} \\ &= \nabla \boldsymbol{\phi}_{\text{ext}} \cdot \hat{\boldsymbol{n}}(t) \\ &= \boldsymbol{V}_{\text{ext}} \cdot \hat{\boldsymbol{n}}(t).\end{aligned} \tag{2.3}$$

All together our Fredholm integral equation of the second kind, applied to the Neumann problem for an unknown distribution of free vortices along a chosen boundary is

$$\oint_S \gamma(s) \frac{\partial \hat{\boldsymbol{\phi}}(s,t)}{\partial \hat{\boldsymbol{n}}} \mathrm{d}s = -\frac{\partial \boldsymbol{\phi}_\infty}{\partial \hat{\boldsymbol{n}}} \tag{2.4a}$$

– or –

$$\oint_S \gamma(s) \hat{\boldsymbol{V}}(s,t) \cdot \hat{\boldsymbol{n}} \mathrm{d}s = -\boldsymbol{V}_{\text{ext}} \cdot \hat{\boldsymbol{n}}. \tag{2.4b}$$

We now have a boundary integral equation that we want to use to solve for the unknown distribution of vortex strengths, $\gamma(s)$.

Before moving on, we should define the coordinate system as well as the fundamental boundary induced velocities we will be using to develop our solution method. The bodies which we would like to model in our application are axisymmetric bodies of revolution (such as the center body) and annular airfoils (such as the duct comprised of a casing and nacelle) of a ducted rotor. This means that rather than using the planar free vortex from section 1.3, we will need to use axisymmetric ring vortices. This does not particularly complicate the method, but does require a different equation for the induced velocity than would be derived from equation (1.29). For a ring vortex, we'll first assume that:

Assumption 2.1

5 Lewis, *Vortex Element Methods for Fluid Dynamic Analysis of Engineering Systems*, 1991.

6 Martensen, "Die Berechnung der Druckverteilung an dicken Gitterprofilen mit Hilfe von Fredholmschen Integralgleichungen zweiter Art," 1959.

7 Courant *et al.*, *Methods of Mathematical Physics*, 1962.

[c] Remember that we want the total normal velocity at the boundary to be zero, so adding this term to both sides should give us zero.

[d] Note that a uniform flow is another of the elementary flows satisfying the Laplace equation.

The vortex ring is circular, such that the ring radius is constant.

$$r_o = \text{constant}$$

Assumption 2.2

The vortex ring circulation is constant and in the tangential direction

$$\boldsymbol{\Gamma} = \gamma \hat{\boldsymbol{e}}_\theta$$

These assumptions formalize our axisymmetric assumption somewhat, and from them we can conclude that the vortex ring has no influence in the tangential direction, $\hat{\boldsymbol{e}}_\theta$.

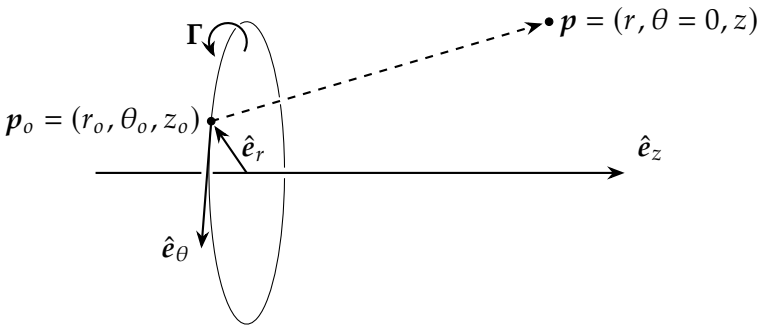

Figure 2.2: Coordinate system for vortex ring induced velocity.

In figure 2.2 we see the coordinate system we will be using going forward. Given this coordinate system, the unit induced velocity components from a ring vortex located coincident with point $\boldsymbol{p}_o$ (analogous to s in equation (2.4)) on a point $\boldsymbol{p}$ (analogous to t in equation (2.4)) lying on the r-z plane are[e]

$$v_z^\gamma = \frac{1}{2\pi r_o}\frac{1}{D_1}\left[\mathcal{K}(m) - \left(1 + \frac{2(\rho-1)}{D_2}\right)\mathcal{E}(m)\right] \tag{2.5a}$$

$$v_r^\gamma = -\frac{1}{2\pi r_o}\frac{\xi/\rho}{D_1}\left[\mathcal{K}(m) - \left(1 + \frac{2\rho}{D_2}\right)\mathcal{E}(m)\right] \tag{2.5b}$$

where the superscript, γ, indicates a unit vortex induced velocity.[5,8] In addition, $\mathcal{K}(m)$ and $\mathcal{E}(m)$ are complete elliptic integrals of the first and second kind, respectively, and

[e] In this and the next chapter, we will use blue shaded boxes around expressions that are major results of the derivations in these chapters and/or that are used directly in code implementations.

5 Lewis, *Vortex Element Methods for Fluid Dynamic Analysis of Engineering Systems*, 1991.

8 Ryall *et al.*, "Design and Test of a Series of Annular Aerofoils," 1967.

$$m = \left(\frac{4\rho}{\xi^2 + (\rho+1)^2}\right) \tag{2.6}$$

$$\xi = \frac{z - z_o}{r_o} \tag{2.7}$$

$$\rho = \frac{r}{r_o} \tag{2.8}$$

$$D_1 = \left[\xi^2 + (\rho+1)^2\right]^{1/2} \tag{2.9}$$

$$D_2 = \xi^2 + (\rho-1)^2. \tag{2.10}$$

A detailed derivation of these ring vortex induced velocities built on the Biot-Savart law introduced in section 1.4 is provided in Appendix A.

For easy reference, we also include here the unit induced velocities of ring sources, though we won't need them until a later chapter:

$$v_z^\sigma = \frac{1}{2\pi r_o}\frac{\xi}{D_1}\left(\frac{2}{D_2}\mathcal{E}(m)\right) \tag{2.11a}$$

$$v_r^\sigma = \frac{1}{2\pi r_o}\frac{1/\rho}{D_1}\left[\mathcal{K}(m) - \left(1 - \frac{2\rho(\rho-1)}{D_2}\right)\mathcal{E}(m)\right], \tag{2.11b}$$

where the superscript, σ, indicates a unit source induced velocity.[5,8] The other variables in equation (2.11) are as defined for the vortex ring expressions.

5 Lewis, *Vortex Element Methods for Fluid Dynamic Analysis of Engineering Systems*, 1991.

8 Ryall *et al.*, "Design and Test of a Series of Annular Aerofoils," 1967.

2.2 Discretizing Fredholm's Equation

2.2.1 Discretizing bodies into panels

Despite the seeming simplicity of equation (2.4), solving the boundary integral equation over an entire boundary all at once is not usually a tractable approach. Instead, we approximate the boundary as a series of segments and sum the integrals over those individual segments. We often approximate the boundary as a polygon, discretizing the boundary using flat segments over which the surface integral is simplified. These flat segments are often referred to as panels, thus the name "panel method."

Our first step in discretization is to look at the surface over which we want to take the boundary integral. We begin with the assumption that:

Assumption 2.3

Smooth bodies can be reasonably represented by a discrete number of flat panels.

Limitations: By approximating the geometry as a polygon, rather than a single continuous curve, we lose some accuracy in our computation.

Justification: As mentioned, it is much easier to solve the problem through the sum of individual components of the boundary, and especially if we simplify those sections into pieces over which the integral is simpler to solve. In addition, with a sufficient number of panels, we obtain a close approximation of the body curvature and therefore the solution of the continuous integral over the entire boundary.

According to assumptions 2.2 and 2.3 we can model the geometry as axisymmetric bands, as shown in figure 2.3(a). Furthermore, we may reduce the geometry for analysis to two dimensions without loss of generality after applying axisymmetry, modeling the geometry with representative cross sections in the r-z plane in cylindrical coordinates.The discretized boundary in our implementation then takes the form of 2D panels (representing the axisymmetric bands). Figure 2.3(a) shows what is intended by a flat, axisymmetric band, and figure 2.3(b) shows the panel representation of said band.

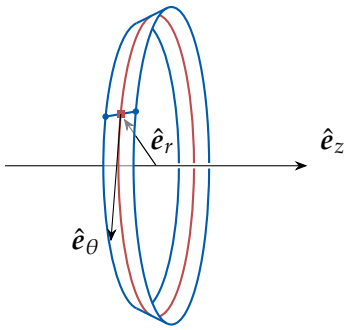

(a) Axisymmetric Band Coordinate System.

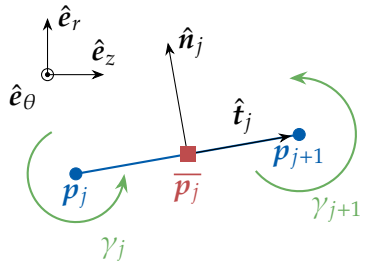

(b) Panel representing axisymmetric band; $\hat{e}_\theta$ out of the page.

Figure 2.3: Axisymmetric band and panel geometry definitions.

One of the convenient traits of a panel method is that we simply need to know the geometry and relative position of each of the panels to calculate the unit induced velocities presented in equation (A.126). As an overview of the panel geometry we need to know, we refer to figure 2.3(b) in which we see a panel defined from the point, $\boldsymbol{p}_j$, to the point, $\boldsymbol{p}_{j+1}$. We take the midpoint of the panel to be $\overline{\boldsymbol{p}}_j = (\boldsymbol{p}_j + \boldsymbol{p}_{j+1})/2$; and we define the unit normal, $\hat{\boldsymbol{n}}_j$, as shown in figure 2.3(b), such that $\hat{\boldsymbol{n}}_j = \hat{\boldsymbol{e}}_\theta \times \hat{\boldsymbol{t}}_j$, where $\hat{\boldsymbol{e}}_\theta$ is the unit vector tangent to the vortex band in the positive θ-direction according to the right hand rule, and $\hat{\boldsymbol{t}}_j$ is the unit tangent to the panel from $\boldsymbol{p}_j$ to $\boldsymbol{p}_{j+1}$ such that $\hat{\boldsymbol{t}}_j = (\boldsymbol{p}_{j+1} - \boldsymbol{p}_j)/||\boldsymbol{p}_{j+1} - \boldsymbol{p}_j||$. In other words, we will assume that the discretized panels are defined such that increasing panel indices lead to the curve being traversed in a clockwise direction.

2.2.2 Applying boundary conditions

As mentioned, we will be using a Neumann boundary condition. Looking at equation (2.4), we do not integrate over t; rather, we apply equation (2.4)

(and therefore the boundary condition) at a set of control points along the boundary. Specifically, we will apply the boundary condition at control points placed at the midpoint of each panel ($\overline{\boldsymbol{p}}$ in figure 2.3(b)). Since the boundary condition states that the normal velocity, due to all contributions, is zero at the control points, we also need to include the freestream contribution to our boundary condition. Putting the surface influence and external influences together, we can, for the ith control point, state our approximate boundary integral equation as

$$\sum_{j=1}^{N} \left[\boldsymbol{K}_{ij} \cdot \hat{\boldsymbol{n}}_i\right] \varphi_j + \boldsymbol{V}_{\text{ext}} \cdot \hat{\boldsymbol{n}}_i = 0, \tag{2.12}$$

Though we often put the external velocity component on the right hand side for convenience, leaving us with

$$\sum_{j=1}^{N} \left[\boldsymbol{K}_{ij} \cdot \hat{\boldsymbol{n}}_i\right] \varphi_j = -\boldsymbol{V}_{\text{ext}} \cdot \hat{\boldsymbol{n}}_i \tag{2.13}$$

where $\boldsymbol{K}$ is comprised of what the unit induced velocities on the ith control point[f] from the jth segment of the surface (the jth panel in our case). Similarly, φ_j are the strengths of the vortices distributed along the jth panel. It is the set of equation (2.13) for each of the control points that will comprise the bulk of of the system of equations we are assembling to solve the boundary value problem.

[f] Note that the ith control point here is synonymous with the point represented by the variable t in equation (2.4).

2.2.3 Calculating Panel Induced Velocities

In order to calculate the panel induced velocities, we want to discretize the vortex distribution along the boundary in a similar fashion to our discretization of the geometry above. In fact, as mentioned, we will split the integral of our boundary integral equation into segments—integrating over each panel. Along each panel then, we need to define a distribution of vortex strengths. There are several options for how we might choose to discretize the vortex distributions along each panel. For example, we may choose to not distribute the strengths and simply use discrete ring vortices along the boundary. Alternatively, we may select the strength of the distribution to be constant along each panel. We may instead select the strength of the distribution to vary linearly along each panel. We could even choose a higher order distribution. For our use case, we will select a linear distribution scheme along each panel, with the panel end points acting as "nodes" between which we will integrate. Discretizing the vorticity distribution along the surface into linear segments then gives us an unknown vorticity magnitude, γ_j, at each panel endpoint (node).

We choose a linear distribution along each panel primarily because discrete distributions and constant distributions have or introduce issues[g] that are solved by moving to a linear distribution[9]. An added benefit is

[g] Specifically, as mentioned by Katz and Plotkin, discrete distributions are "inadequate near the stagnation points of a thick airfoil," and in practice are used for zero thickness airfoils rather than for closed surfaces. Additionally, constant vortex distributions introduce several issues also discussed by Katz and Plotkin that are solved by moving to a linear distribution scheme.

9 Katz *et al.*, *Low speed aerodynamics*, 2001.

that a linear distribution allows a more accurate solution for a coarser discretization of the geometry than constant strength panels do. We choose not to utilize a higher order method mainly due to the diminishing returns of going to higher order panels.

Because the surface integrals of velocities induced by axisymmetric vortex rings are exceptionally difficult to solve analytically, we will take a numerical approach. Specifically, we will utilize Gauss-Legendre quadrature which was introduced in section 1.2. In the nominal case when a panel induces velocity on the surface, but not on itself, we set things up as follows for a given panel and surface point, t: We start with the portion of the surface integral associated with the jth panel

$$\int_{\boldsymbol{p}_j}^{\boldsymbol{p}_{j+1}} \gamma(s) \frac{\partial \hat{\boldsymbol{\phi}}(s,t)}{\partial \hat{\boldsymbol{n}}_t} \mathrm{d}s. \tag{2.14}$$

Because the unit normal applies at t, it is a constant in this integral. As such, we can express the integral in terms of the integration of velocities only, which are then multiplied by the components of the normal vector after integration.

$$\begin{aligned} \boldsymbol{v}_{tj} &= \int_{\boldsymbol{p}_j}^{\boldsymbol{p}_{j+1}} \gamma(s) \frac{\partial \hat{\boldsymbol{\phi}}(s,t)}{\partial \hat{\boldsymbol{n}}_t} \mathrm{d}s \\ &= \left(\int_{\boldsymbol{p}_j}^{\boldsymbol{p}_{j+1}} \gamma(s) \nabla \hat{\boldsymbol{\phi}}(s,t) \mathrm{d}s \right) \cdot \hat{\boldsymbol{n}}_t \\ &= \left(\int_{\boldsymbol{p}_j}^{\boldsymbol{p}_{j+1}} \gamma(s) \hat{\boldsymbol{V}}(s,t) \mathrm{d}s \right) \cdot \hat{\boldsymbol{n}}_t. \end{aligned} \tag{2.15}$$

To get the integral in terms of components of velocity, we can split up the integral into its components

$$v_{z_{tj}} = \left(\int_{\boldsymbol{p}_j}^{\boldsymbol{p}_{j+1}} \gamma(s) v_z(s,t) \mathrm{d}s \right) n_{i_z}, \tag{2.16a}$$

$$v_{r_{tj}} = \left(\int_{\boldsymbol{p}_j}^{\boldsymbol{p}_{j+1}} \gamma(s) v_r(s,t) \mathrm{d}s \right) n_{i_r}. \tag{2.16b}$$

Since we are working toward assembling a system of equations, and we have introduced the unknown vortex magnitudes, γ_j, which define the vorticity distribution along the boundary, we need to obtain the integrals over the panels in terms of each of the panel node strengths (γ_j). As we perform our numerical integration, the quadrature procedure selects sample points along the range of integration as already mentioned. To make things easier to implement, we will transform our integrals such that the integrator will integrate on the range (0,1) and we will introduce the transformed variable ζ as the variable of integration.

$$v_{z_{t_j}} = \left(\Delta s \int_0^1 \gamma(s(\zeta))v_z(s(\zeta),t)\mathrm{d}\zeta\right) n_{i_z}, \tag{2.17a}$$

$$v_{r_{t_j}} = \left(\Delta s \int_0^1 \gamma(s(\zeta))v_r(s(\zeta),t)\mathrm{d}\zeta\right) n_{i_r}. \tag{2.17b}$$

where Δs is the length of the range of integration, or panel length. Referencing figure 2.4, we see that the quadrature function samples can be split into the influences of each of the panel nodes by a simple geometric weighting:[h]

[h] This is made possible due to the linear vortex distribution along a flat panel.

$$f_j(x_k) = w_k f(s(\zeta_k),t) \qquad (1-\zeta_k) \qquad \text{due to } \gamma_j \tag{2.18a}$$

$$f_{j+1}(x_k) = w_k f(s(\zeta_k),t) \qquad \zeta_k \qquad \text{due to } \gamma_{j+1}. \tag{2.18b}$$

In other words, we return a piece of the integral weighted according to the sample point location along the range of integration. Because we transformed the range of integration to (0,1), we can simply take these geometrically proportional weights to be $1-\zeta$ and ζ where $\zeta \in (0,1)$ for the jth and $(j+1)$th nodes, respectively. Note that the γ_j values are also constant relative to ζ and are therefore not included in the integrand expressions of equation (2.18). This allows us to pull out all of the γ_j terms which are the unknowns for which we want to solve using the system of equations we are assembling. All together, the unit velocities normal to the ith panel, induced by the jth panel (defined by the jth and $(j+1)$th nodes), or what we term the influence coefficients, IC, are

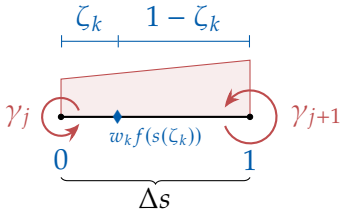

Figure 2.4: Visual representation of splitting the integral into the portions for each panel node.

$$\begin{aligned} IC_{ij} &= \left(\Delta s_j \sum_k^N w_k v_z(s(\zeta_k),t)(1-\zeta_k)\right) n_{i_z} + \left(\Delta s_j \sum_k^N w_k v_r(s(\zeta_k),t)(1-\zeta_k)\right) n_{i_r} \\ IC_{i(j+1)} &= \left(\Delta s_j \sum_k^N w_k v_z(s(\zeta_k),t)\zeta_k\right) n_{i_z} + \left(\Delta s_j \sum_k^N w_k v_r(s(\zeta_k),t)\zeta_k\right) n_{i_r}, \end{aligned} \tag{2.19}$$

for the jth and $(j+1)$th nodes, respectively.

In the singular case, where the panel induces velocity on itself, more consideration is required. We first need to remember that we chose the midpoint of each panel to be the control point. Because the expression for induced velocity is singular when the distance between the point of influence and the point being influenced is zero, there is a singularity at the panel midpoint of a panel inducing velocity on its own control point. Knowing beforehand exactly where the singularity lies makes things somewhat easier to approach, but we still need to address the singularity. We will take the separation of singularity approach also introduced in section 1.2 to calculate the self-induced case. The separation of singularity method is, in brief, to subtract out the singular piece of the integral while

solving the integral, then afterward adding back in the singular piece solved analytically to avoid the computational issues associated with the computer attempting to divide by zero. Basically, as the integral tends to positive and negative infinity on either side of the singular point, we cancel out the non-convergent values on either side of the singular point and replace them with an analytic approximation. Mathematically we have the integral

$$v_{jj} = \int_{p_j}^{p_{j+1}} \gamma(s) I(s) \mathrm{d}s, \tag{2.20}$$

where

$$I(s) = \frac{\partial \hat{\phi}(s, \overline{p}_j)}{\partial \hat{n}_j}$$

We need to subtract off the singular part, S, (inside the integral), and then add back an analytical expression, A, for the integral of subtracted singular part (outside the integral). To avoid evaluating the integral at the singular point, we also will need to split the integration range in two, integrating from the start of the integration range to the singular point, then from the singular point to the end of the integration range.[i]

[i] Note that the sample points associated with the Gauss-Legendre polynomials do not actually sample the integration range at its endpoints.

$$v_{jj} = \int_{p_j}^{p_{j+1}} \gamma(\zeta)(\Big(I(s(\zeta), \overline{p}_j) - S(s(\zeta), \overline{p}_j)\Big) \, \mathrm{d}\zeta + \gamma A(\overline{p}_j). \tag{2.21}$$

After these modifications to account for the singularity, the procedure for applying the quadrature is the same as before giving us the influence coefficients for the panel on itself to be

$$\begin{aligned}
IC_{ii} =& \Delta s_i \left(\sum_k^N w_k \left[\left(v_z(s(\zeta_k), \overline{p}_i) \right) (1 - \zeta_k) - \frac{1}{2} S_z(s(\zeta_k), \overline{p}_i) \right] + \frac{1}{2} A_z(\overline{p}_i) \right) n_{i_z} \\
&+ \Delta s_i \left(\sum_k^N w_k \left[\left(v_r(s(\zeta_k), \overline{p}_i) \right) (1 - \zeta_k) - \frac{1}{2} S_r(s(\zeta_k), \overline{p}_i) \right] + \frac{1}{2} A_r(\overline{p}_i) \right) n_{i_r} \\
IC_{i(i+1)} =& \Delta s_i \left(\sum_k^N w_k \left[\left(v_z(s(\zeta_k), \overline{p}_i) \right) \zeta - \frac{1}{2} S_z(s(\zeta_k), \overline{p}_i) \right] + \frac{1}{2} A_z(\overline{p}_i) \right) n_{i_z} \\
&+ \Delta s_i \left(\sum_k^N w_k \left[\left(v_r(s(\zeta_k), \overline{p}_i) \right) \zeta - \frac{1}{2} S_r(s(\zeta_k), \overline{p}_i) \right] + \frac{1}{2} A_r(\overline{p}_i) \right) n_{i_r}
\end{aligned} \tag{2.22}$$

where

$$
\begin{aligned}
S_z(\boldsymbol{p}_o, \boldsymbol{p}) =& \frac{r_o - r}{2\pi\left[(z - z_o)^2 + (r - r_o)^2\right]} - \frac{1}{8\pi r_o}\left[\ln\left(\frac{(z - z_o)^2 + (r - r_o)^2}{64 r_o^2}\right)\right] \\
S_r(\boldsymbol{p}_o, \boldsymbol{p}) =& \frac{z - z_o}{2\pi\left[(z - z_o)^2 + (r - r_o)^2\right]},
\end{aligned}
\tag{2.23}
$$

and

$$
\begin{aligned}
A_z(\boldsymbol{p}) =& \frac{1}{4\pi r}\left(1 + \ln\frac{8r}{\Delta s}\right) \\
A_r(\boldsymbol{p}) =& 0;
\end{aligned}
\tag{2.24}
$$

and the multiplication by $1/2$ on the singular and analytic terms is due to the fact that the singular point is half way between the nodes, so each node is responsible for exactly half of the influence.

2.3 Assembling and Solving the Linear System

To find the strengths of each vortex node that result in a vortex distribution inducing a flow field matching our prescribed body geometry, we need to assemble a system composed of equation (2.13) for each panel. Note, however, that currently our expression for $\boldsymbol{K}$ is indexed according to panel, and contains information about more than one panel node, which we need to remedy in order to get expressions for the individual strengths at each node. This is precisely why we separated out the node influences in the previous subsection. Thus each node has a component of influences associated with each panel to which it is an edge point. For the jth node then, we can add the contributions due to the $(j-1)$th and jth panels for which it is an edge point. This allows us to assemble the influence coefficient matrix based on a node-control point scheme rather than a panel-control point scheme:

$$
\boldsymbol{G}_{ij} = \begin{cases} IC_{ij} & \text{for } j = 1, N+1 \\ IC_{ij} + IC_{i(j-1)} & \text{for } 2 \leq j \leq N \end{cases}
\tag{2.25}
$$

where $\boldsymbol{G}$ is the $N \times N+1$ matrix whose elements, $\boldsymbol{G}_{ij}$, are the influence coefficients of the jth node ($N+1$ total) on the ith control point (N total); and the influence components, IC, are defined in equations (2.19) and (2.22) for the nominal and self-induced cases, respectively. Since $\boldsymbol{G}$ is not square, as it has one more unknown than boundary conditions, we cannot solve the system directly as is. Fortunately, we also require an additional condition to make things work.

2.3.1 The Kutta Condition

One of the shortcomings of using potential flow theory is that by itself, it lacks inherent mechanisms for ensuring the flow leaves the surface of lifting bodies at the correct location and in the correct direction. One

solution to this problem is known as the Kutta condition, which can be stated in several equivalent ways. However it may be stated, the Kutta condition requires the flow over a lifting body with a sharp trailing edge to leave the body at the trailing edge in a manner roughly tangent to the trailing edge. Therefore we can artificially enforce conditions that are observed in real, viscous flows at relatively low angles of attack.

Just as there are several equivalent ways to state the Kutta condition, there are several ways that the Kutta condition may be implemented. One method is to require zero circulation at the trailing edge. We can enforce this by setting the strengths of the first and last panel nodes to be equal[j] and opposite such that

$$\gamma_1 + \gamma_N = 0. \tag{2.26}$$

[j] Note that for a sharp trailing edge, where the nodes are coincident, they really should be equal anyway since they occupy the same point in space.

In order to make our system square, we simply add the Kutta condition as the $N+1$th equation.

By itself, this version of the Kutta condition can lead to spurious spikes in surface velocity near the trailing edge. In order increase the numerical robustness of the panel method, we apply an additional, indirect Kutta condition used in the panel method of the Ducted Fan Design Code.[10] It entails placing an additional control point just inside the interior of the duct trailing edge and define an associated unit normal oriented such that the unit normal is effectivelyin the direction of the bisection angle of the trailing edge panels. We also place an additional control point inside the center body if it has a blunt trailing edge.[k]

10 Drela *et al.*, *Ducted Fan Design Code (DFDC)*, 2005.

[k] We will discuss shortly the case where the center body has a sharp trailing edge.

We apply the same boundary condition on these control point as the other control points in that we set the normal velocity induced by the freestream to be equal and opposite to the tangential velocity induced by the body boundaries on the control point.

$$\sum_{j=1}^{N+1} \gamma_j \boldsymbol{G}^{\circ-}_{kj} = -\boldsymbol{V}_\infty \cdot \hat{\boldsymbol{n}}_k. \tag{2.27}$$

where the elements of $\boldsymbol{G}^{\circ-}$ are the expressions defined in equation (2.19).

Upon the addition of this equation, however, we find ourselves with insufficient unknowns (one for each body being modeled). To remedy this insufficiency, we simply apply a dummy strength, τ_k, for the kth body and set all of its associated influence coefficients, $\mathcal{T}$, to 1 for the panels of the body it is applied to and zero elsewhere (including itself).

$$\mathcal{T}_{ik} = \begin{cases} 1 & \text{if } i = k \\ 0 & \text{otherwise} \end{cases} \tag{2.28}$$

We mentioned placing the additional control point just inside the trailing edge. This is done (rather than right at the middle of the trailing edge gap between the trailing edge nodes) to avoid numerical issues if

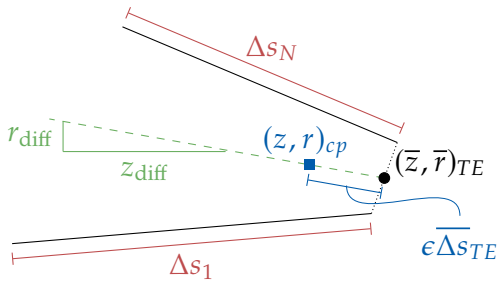

Figure 2.5: Geometric explanation of internal control point placement.

the trailing edge is indeed sharp. We specifically place the node along the line bisecting the trailing edge angle and passing through the point halfway between the trailing edge nodes. The position is calculated as follows

$$z_{cp} = \overline{z}_{TE} - \epsilon\overline{\Delta s}_{TE}\frac{z_{\text{diff}}}{s_{\text{diff}}} \tag{2.29a}$$

$$r_{cp} = \overline{r}_{TE} - \epsilon\overline{\Delta s}_{TE}\frac{r_{\text{diff}}}{s_{\text{diff}}} \tag{2.29b}$$

$$\hat{n}_{z_{cp}} = \frac{z_{\text{diff}}}{s_{\text{diff}}} \tag{2.29c}$$

$$\hat{n}_{r_{cp}} = \frac{r_{\text{diff}}}{s_{\text{diff}}} \tag{2.29d}$$

where

$$\epsilon = 0.05 \tag{2.30}$$

$$\overline{z}_{TE} = \frac{z_1 + z_{N+1}}{2} \tag{2.31}$$

$$\overline{r}_{TE} = \frac{r_1 + r_{N+1}}{2} \tag{2.32}$$

$$\overline{\Delta s}_{TE} = \frac{\Delta s_1 + \Delta s_N}{2} \tag{2.33}$$

$$z_{\text{diff}} = \Delta z_N - \Delta z_1 \tag{2.34}$$

$$r_{\text{diff}} = \Delta r_N - \Delta r_1 \tag{2.35}$$

$$s_{\text{diff}} = \left[z_{\text{diff}}^2 + r_{\text{diff}}^2\right]^{1/2} \tag{2.36}$$

where the $\Delta(\cdot)$ lengths are calculated in the clockwise direction as before, and ϵ is chosen for generally good numerical behavior.

2.3.2 Additional Considerations for Open Bodies

The Kutta condition we have applied assumes that the trailing edge is both sharp and thin. This approximation tends to be relatively good for a large variety of geometries, and is well behaved numerically, but eventually breaks down. Specifically in the case of blunt trailing edges, when the trailing edge panel nodes are not coincident, the flow field

can tend to flow into the inside of the body through the open trailing edge. To prevent this, we will add a trailing edge panel with distribution strengths determined from the adjacent panels, similar to the method used by XFOIL[11,12] for blunt trailing edges.

For any trailing edge panel, we will set a vortex and source distribution along the panel based on its orientation to the adjacent panels and the distribution strengths at the shared node locations:

$$\gamma_{TE_j} = \left(\hat{\boldsymbol{n}}_{TE_j} \cdot \hat{\boldsymbol{n}}_{\text{adj}_j}\right) \gamma_{\text{adj}_j} \tag{2.37}$$

$$\sigma_{TE_j} = -\left|\hat{\boldsymbol{n}}_{TE_j} \times \hat{\boldsymbol{n}}_{\text{adj}_j}\right| \gamma_{\text{adj}_j}. \tag{2.38}$$

where the "adj" subscript indicates the adjacent panel. Based on these definitions of strength distributions across the trailing edge panels, we can take the unit strengths (relative to the unknown distribution strengths on the shared nodes) to be

$$\hat{\gamma}_{TE_j} = \hat{\boldsymbol{n}}_{TE_j} \cdot \hat{\boldsymbol{n}}_{\text{adj}_j} \tag{2.39}$$

$$\hat{\sigma}_{TE_j} = -\left|\hat{\boldsymbol{n}}_{TE_j} \times \hat{\boldsymbol{n}}_{\text{adj}_j}\right|. \tag{2.40}$$

The vortex term here enforces smooth streamlines off the upper and lower surfaces, despite the trailing edge gap. The source term enforces the no flow through condition at the trailing edge.

For trailing edge panels which have a node on the axis of rotation, for example, in the case of a center body with a blunt trailing edge, we set the strength (γ_{TE_j}) and derivative ($\partial\gamma_{TE_j}/\partial\gamma$) of the vortex distribution at the axis to zero. Since we do not have an adjacent panel on the axis side of such a trailing edge panel, we will simply use the same adjacent panel to calculate values for both source nodes of the trailing edge panel.

To add the trailing edge panels to the linear system we do not want to add any more equations, because we have defined the trailing edge panel strengths according to unknowns we already have in the system. As such, we simply need to augment the influence coefficients for the panels adjacent to the trailing edge panels, since all the trailing edge panel information comes directly from those adjacent panels. For each panel with a node bordering a trailing edge panel, we add the following to the unit induced velocity on every control point

$$\hat{\boldsymbol{V}}^{\gamma}_{iTE_j} \stackrel{+}{=} \hat{\boldsymbol{V}}^{\gamma}_{iTE_j} \hat{\gamma}_{TE_j} + \hat{\boldsymbol{V}}^{\sigma}_{iTE_j} \hat{\sigma}_{TE_j}. \tag{2.41}$$

In other words, we add the unit induced velocity associated with the trailing edge node to the panel sharing that node scaled by how aligned the trailing edge and adjacent panel are. As an example, if the duct had a blunt trailing edge, we would define a trailing edge panel spanning the gap from the first to the last node in the airfoil geoemetry. We would then define the strengths and changes in strength relative to the first and

11 Drela, "XFOIL: An Analysis and Design System for Low Reynolds Number Airfoils," 1989.

12 Fidkowski, "A Coupled Inviscid–Viscous Airfoil Analysis Solver, Revisited," 2022.

last panels of the geometry (those at the trailing edge). Finally, we would augment the unit induced velocity due to the first and last nodes by the above expressions for the trailing edge gap panel we defined. We can apply this to the velocity directly, or we can simply add the velocities dotted with the control point normal vectors to the influence coefficient matrix after the fact.

$$\boldsymbol{G}_{ij} \stackrel{+}{=} \left[\hat{\boldsymbol{V}}^{\gamma}_{iTE_j}\hat{\gamma}_{TE_j} + \hat{\boldsymbol{V}}^{\sigma}_{iTE_j}\hat{\sigma}_{TE_j}\right]\cdot\hat{\boldsymbol{n}}_i, \tag{2.42}$$

where the jth components of unit induced velocity, $\hat{\boldsymbol{V}}$, are calculated from equation (2.19).[l]

[l] Exchanging the vortex ring induced unit velocities for those induced by source rings for the source terms in equation (2.42).

2.3.3 Additional Considerations for Nodes on the Axis of Revolution

As we have already discussed, annular airfoils with non-zero cambered cross-sections require the addition of a Kutta condition. Bodies of revolution do not require such a condition in an axisymmetric scheme, but rather have other unique features to consider. Specifically, bodies of revolution will have a panel node on the axis of revolution (at the leading edge). As we can see in the definition of unit induced velocity (equation (A.126)), if an influence point lies on the axis, that is if $r_o = 0$, then the induced velocity becomes infinite. In reality, the induced velocity from such a point is zero. Therefore in our system, we will need to prescribe the strengths of panel nodes on the axis of rotation to be zero strength. In order to achieve this, we take an approach similar to applying the Kutta condition: we simply add the equation

$$\gamma^{cb}_{LE} = 0 \tag{2.43}$$

to the system, where γ^{cb}_{LE} is the prescribed node strength for the center body leading edge. This additional equation also solves the issue of the matrix not being square due to there still being $N+1$ nodes and only N panels for a body of revolution. If the center body trailing edge is sharp, then we have an additional node on the axis of rotation and also need to prescribe its strength to zero. As it turns out, we do not actually need the additional internal control point for bodies of revolution, but it doesn't hurt us to have it implemented. In the case of a closed trailing edge, we will effectively remove the internal control point and substitute its equation with an equation prescribing the trailing edge node strength to be zero like the leading edge node:

$$\gamma^{cb}_{TE} = 0. \tag{2.44}$$

Since we still have an additional equation, we will keep the dummy variable in place simply to keep the system square. Note that we could

have instead removed equations from the system rather than adding equations, but it turns out to be more convenient for consistent bookkeeping purposes to put things together as we have described.

2.3.4 Solving the linear system

To avoid confusion, we will let $\boldsymbol{G}^*$ represent the influence matrix augmented by the Kutta condition, additional trailing edge control point equations, and any prescribed node equations. Because the overall coupled solver in DuctAPE will need to solve the linear system for the panel method many times, it is advantageous to do as much precomputation as possible for the panel method. The first thing that we will note is that the body geometry will not change throughout the coupled solve. This means that the influence matrix $\boldsymbol{G}^*$ can be fully precomputed and stored. Due to this fact, we can also speed up the multiple linear solves by performing a Lower-Upper (LU) decomposition of $\boldsymbol{G}^*$ such that

$$\boldsymbol{G}^* = \boldsymbol{L}\boldsymbol{U} \tag{2.45}$$

where $\boldsymbol{L}$ and $\boldsymbol{U}$ are the lower and upper triangular matrices of the LU decomposition. By precomputing the LU decomposition, we can speed up the solution process of the linear system, which can now be expressed as

$$\boldsymbol{L}\boldsymbol{U}\boldsymbol{\gamma} = \boldsymbol{b} \tag{2.46}$$

where $\boldsymbol{b} = (-\boldsymbol{V}_{\text{ext}} \cdot \hat{n})$. We can solve this system through the forward and backward substitution in two steps:

1. Solve $\boldsymbol{L}\boldsymbol{y} = \boldsymbol{b}$ for $\boldsymbol{y}$.
2. Solve $\boldsymbol{U}\boldsymbol{\gamma} = \boldsymbol{y}$ for $\boldsymbol{\gamma}$.

Although this is a two-step process, it ends up being numerically more efficient than a more direct system solve method, and again has the benefit of being able to be precomputed and used repeatedly.

2.4 Post-processing the Panel Method Solution

2.4.1 Velocity Tangent to the Body Surface

After we have solved for the node strengths, $\boldsymbol{\gamma}$, that coincide with our selected body geometry, we desire to use those strengths to find the velocity somewhere in the field. We are especially interested in finding the surface velocity on the body and using it to determine the pressure distribution on the body surface. In order to obtain the surface velocity, we need to find the velocity induced tangent to the panels. We can do so by applying the same kind of Fredholm integral expression, but this time taking the tangential derivative, and remembering that the jump term across the boundary for the tangential velocity is $-\gamma/2$ outward and $\gamma/2$ inward[6]:

6 Martensen, "Die Berechnung der Druckverteilung an dicken Gitterprofilen mit Hilfe von Fredholmschen Integralgleichungen zweiter Art," 1959.

$$v_{\tan}(t) = \pm\frac{\gamma(t)}{2} + \oint_S \gamma(s)\frac{\partial\hat{\boldsymbol{\phi}}(s,t)}{\partial\hat{\boldsymbol{t}}_t}\mathrm{d}s + \frac{\partial\boldsymbol{\phi}_{\text{ext}}}{\partial\hat{\boldsymbol{t}}_t} \tag{2.47a}$$

– or –

$$v_{\tan}(t) = \pm\frac{\gamma(t)}{2} + \oint_S \gamma(s)\hat{\boldsymbol{V}}(s,t)\cdot\hat{\boldsymbol{t}}(t)\mathrm{d}s + \boldsymbol{V}_{\text{ext}}\cdot\hat{\boldsymbol{t}}(t). \tag{2.47b}$$

We can therefore use the same discretization scheme and induced velocity expressions as we did to create our linear system. To simplify things further, we can also simply take the sum of the full induced velocities on the control points and the magnitude will be the surface velocity. This is due to the fact that we solved for the vortex strengths based on the boundary condition of zero flow normal to the control points; therefore when all the velocity components are summed, all that is left is the velocity tangent to the surface.[m]

[m] Remember that the jump term is a jump in tangential velocity and the linear system solution only gave us a magnitude, so before adding the jump term in, we need to make sure to separate it into components tangent to the panel.

$$v_{\tan_i} = \left|\pm\frac{\overline{\gamma}_i}{2}\hat{\boldsymbol{t}}_i + \sum_{j=1}^{N+1}\left[\gamma_j\boldsymbol{M}_{ij}\right] + \boldsymbol{V}_{\text{ext}}\right|, \tag{2.48}$$

where

$$\overline{\gamma}_i = \frac{\gamma_i + \gamma_{i+1}}{2}, \tag{2.49}$$

and

$$\boldsymbol{M}_{ij} = \begin{cases} IC^t_{ij} & \text{for } j = 1, N+1 \\ IC^t_{ij} + IC^t_{i(j-1)} & \text{for } 2 \le j \le N, \end{cases} \tag{2.50}$$

where for the nominal case, the components of the influence coefficients are defined identically to equation (2.19), but we keep them in vector format for simplicity:

$$\begin{aligned} IC^t_{ij} &= \left(\Delta s_j \sum_k^N w_k v_z(s(\zeta_k),t)(1-\zeta_k)\right) + \left(\Delta s_j \sum_k^N w_k v_r(s(\zeta_k),t)(1-\zeta_k)\right) \\ IC^t_{i(j+1)} &= \left(\Delta s_j \sum_k^N w_k v_z(s(\zeta_k),t)\zeta_k\right) \qquad + \left(\Delta s_j \sum_k^N w_k v_r(s(\zeta_k),t)\zeta_k\right). \end{aligned} \tag{2.51}$$

For the self-induced case, again, the expressions are identical to equation (2.22), but again we keep things in vector format rather than dotting with the normal:

$$
\begin{aligned}
IC^t_{ii} &= \left(\Delta s_i \sum_k^N w_k \left[v_z(s(\zeta_k), \overline{\boldsymbol{p}}_i) - S_z(s(\zeta_k), \overline{\boldsymbol{p}}_i) + \frac{A_z(\overline{\boldsymbol{p}}_i)}{\Delta s_i}\right](1-\zeta_k)\right) \\
&\quad + \left(\Delta s_i \sum_k^N w_k \left[v_r(s(\zeta_k), \overline{\boldsymbol{p}}_i) - S_r(s(\zeta_k), \overline{\boldsymbol{p}}_i) + \frac{A_r(\overline{\boldsymbol{p}}_i)}{\Delta s_i}\right](1-\zeta_k)\right) \\
IC^t_{i(i+1)} &= \left(\Delta s_i \sum_k^N w_k \left[v_z(s(\zeta_k), \overline{\boldsymbol{p}}_i) - S_z(s(\zeta_k), \overline{\boldsymbol{p}}_i) + \frac{A_z(\overline{\boldsymbol{p}}_i)}{\Delta s_i}\right]\zeta_k\right) \\
&\quad + \left(\Delta s_i \sum_k^N w_k \left[v_r(s(\zeta_k), \overline{\boldsymbol{p}}_i) - S_r(s(\zeta_k), \overline{\boldsymbol{p}}_i) + \frac{A_r(\overline{\boldsymbol{p}}_i)}{\Delta s_i}\right]\zeta_k\right).
\end{aligned}
\tag{2.52}
$$

Note that the coefficients, $\boldsymbol{M}$, along with the system influence coefficients, $\boldsymbol{G}^*$, can be precomputed and stored, although there is really no need for an LU-decomposition for $\boldsymbol{M}$ as there is no linear solve, but rather a direct matrix-vector multiplication to calculate the tangential velocity. In addition, the procedure in the presence of a trailing edge gap panel is identical to that presented for the normal induced velocities, with the exception already discussed here: that no dot product need be taken.

2.4.2 Velocity at Arbitrary Points in Space

For arbitrary points in space, the procedure for obtaining velocities is nearly identical, with the exceptions that there will be no self-induced or jump terms off the body surface, and we need not dot the components with any unit vector, as we typically want to know the velocity components in the global reference frame.

$$
\boldsymbol{V}_{\text{field}}(\boldsymbol{q}) = \oint_S \gamma(s) \nabla \boldsymbol{\phi}(s, \boldsymbol{q}) \mathrm{d}s + \nabla \boldsymbol{\phi}_{\text{ext}} \tag{2.53a}
$$

– or –

$$
\boldsymbol{V}_{\text{field}}(\boldsymbol{q}) = \oint_S \gamma(s) \boldsymbol{V}(s, \boldsymbol{q}) \mathrm{d}s + \boldsymbol{V}_{\text{ext}}. \tag{2.53b}
$$

We can still use the same discretization scheme and induced velocity expressions as we did to create our linear system, and body surface velocity calculations, but this time, instead of dotting the velocity vector with some vector, we will keep things in a vector format. In other words, we will keep the axial and radial components of induced velocity separate:

$$
\boldsymbol{V}_{\text{field}}(\boldsymbol{q}) = \boldsymbol{M}\boldsymbol{\gamma} + \boldsymbol{V}_{\text{ext}}. \tag{2.54}
$$

where

$$\boldsymbol{M}_j = \begin{cases} IC_j^f & \text{for } j = 1, N+1 \\ IC_j^f + IC_{j-1}^f & \text{for } 2 \leq j \leq N, \end{cases} \tag{2.55}$$

where

$$\begin{aligned} IC_j^f &= \left[\Delta s_j \sum_k^N w_k v_z(s(\zeta_k), \boldsymbol{q})(1-\zeta_k), \Delta s_j \sum_k^N w_k v_r(s(\zeta_k), \boldsymbol{q})(1-\zeta_k) \right] \\ IC_{j+1}^f &= \left[\Delta s_j \sum_k^N w_k v_z(s(\zeta_k), \boldsymbol{q})\zeta_k, \Delta s_j \sum_k^N w_k v_r(s(\zeta_k), \boldsymbol{q})\zeta_k \right]. \end{aligned} \tag{2.56}$$

2.4.3 Body Forces

Due to assumption 2.2, the net radial pressure forces on the body cancel; we also assume there are no tangential forces induced due to the bodies. We therefore sum the forces due to pressure in the axial direction to obtain drag (or thrust) of the bodies.

$$T_{\text{bod}} = \frac{1}{2}\rho_\infty V_{\text{ref}}^2 f_z \tag{2.57}$$

where the non-dimensional force coefficient, f_z, is the integral of the pressure force coefficient in the axial direction about the body surfaces:

$$f_z = \sum_{i=1}^{N_b} 2\pi \int_{S_i} r(s_i) c_p(s_i) \hat{\boldsymbol{n}}_z(s_i) \mathrm{d}s_i. \tag{2.58}$$

In the case of a blunt trailing edge, the trailing edge gap panel is also included in the integral for the total axial force coefficient, though the pressure coefficient values used in that case are simply the average of the adjoining panels in the duct case, and the last panel in the center body case.

For a ducted rotor, the pressure coefficient on the body surface changes aft of any rotor planes due to the enthalpy and entropy jumps across the rotor plane as well as the addition of swirl velocity. We will see in the next chapter (specifically equation (3.61)) that the steady state pressure coefficient changes due to the disk jumps across the rotor as

$$\begin{aligned} \Delta c_{p_{hs}} &= \frac{\widetilde{p}_t}{\frac{1}{2}\rho V_{\text{ref}}^2} \\ &= \frac{\rho\left(\widetilde{h} - \widetilde{S}\right)}{\frac{1}{2}\rho V_{\text{ref}}^2} \\ &= \frac{\widetilde{h} - \widetilde{S}}{\frac{1}{2} V_{\text{ref}}^2} \end{aligned} \tag{2.59}$$

The pressure is also altered by the addition of swirl velocity due to the rotor. We treat this in the same manner as we do for the nominal, steady pressure coefficient based on the surface velocity. For the nominal case, we only look at the velocity in the axial and radial directions, obtaining the velocity tangent to the body surfaces. The pressure coefficient, is given by

$$c_p = \frac{p - p_\infty}{\frac{1}{2}\rho V_{\text{ref}}^2} \tag{2.60}$$

By assumption 1.2, we can apply Bernoulli's equation

$$p_\infty + \frac{1}{2}\rho V_\infty^2 = p + \frac{1}{2}\rho V_{\text{tan}}^2 \tag{2.61}$$

$$p - p_\infty = \frac{1}{2}\rho V_\infty^2 - \frac{1}{2}\rho V_{\text{tan}}^2 \tag{2.62}$$

where V_{tan} is the velocity tangent to the body surface, and substitute into the numerator and cancel to obtain

$$c_p = \frac{V_\infty^2 - V_{\text{tan}}^2}{V_{\text{ref}}^2} \tag{2.63}$$

Aft of the rotor, inside the duct, and on the outer side of the body surfaces V_{tan} contains a swirl component that is not present upstream of the rotor. Since the $V_{\theta_\infty} = 0$, the change in pressure coefficient aft of the rotor due to the addition of swirl velocity is simply

$$\Delta c_{p_\theta} = -\frac{V_\theta^2}{V_{\text{ref}}^2} \tag{2.64}$$

All together the outer surface pressure coefficient rise aft of a rotor is then:

$$\begin{aligned} \Delta c_p &= \Delta c_{p_{hs}} + \Delta c_{p_\theta} \\ &= \frac{2(\widetilde{h} - \widetilde{S}) - V_\theta^2}{V_{\text{ref}}^2}. \end{aligned} \tag{2.65}$$

2.5 Beyond the Inviscid Assumption: An Integral Boundary Layer Model for Viscous Drag

Since panel methods are developed on an assumption of inviscid flow, they are inherently unable to model viscous drag effects on the boundaries they model. Fortunately, we can combine inviscid panel methods with additional boundary layer models in order to capture viscous drag along the body surfaces. To do so, we will need to assume that:

Assumption 2.4

The Reynolds number of the inviscid flow is large.

Limitations: We can't model very slow flows.

Justification: For all the applications in this work, we will have large Reynolds numbers.

By assumption 2.4 we can split the flow into an approximate invisicd outer flow and a viscous layer close to the body surface (or boundary of the boundary element method), which we call the boundary layer. The typical approach to modeling boundary layers in conjunction with panel methods is to use three models: a laminar boundary layer model, a turbulent boundary layer model, and a model for transition from laminar to turbulent. For our purposes here, we will assume:

Assumption 2.5

The boundary layer can be modeled as fully turbulent.

Limitations: We are over-predicting the viscous drag as we are not modeling any laminar region in the boundary layer.

Justification: It is beyond the scope of this work to develop a continuous boundary layer transition model, and our over-prediction should be relatively small.

We will also assume the following:

Assumption 2.6

There is no heat transfer across the body surfaces; in other words, an adiabatic wall condition.

Limitations: We will not be modeling thermal effects on the boundary layer, which may be somewhat important especially for the center body which houses the motor.

Justification: We are not including a motor/heat model in this work anyway, and due to the presence of the rotor, boundary layer transition would likely occur before thermal effects influence the boundary layer.

Assumption 2.7

The flow is isentropic.

Limitations: Again, we won't be including any heat transfer, and no energy transformations due to friction or viscosity.

Justification: This is a suitable simplifying assumption for the level

of fidelity of the models in this work, especially since we don't have any thermal models.

In modeling the boundary layer, we will want to think in terms of several idealized thicknesses. We first define the boundary layer thickness to be the length from the body surface to the point normal to the surface where the velocity equals the inviscid velocity. We will call this the boundary layer thickness, δ. The idealized thickness with equivalent mass flow is called the displacement thickness, δ_1 (many use the symbol δ^*). Mathematically, the displacement thickness is defined at a specific location along the surface as

$$\delta_1 = \int_0^\infty \left(1 - \frac{\rho u}{\rho_e U_e}\right) dy, \tag{2.66}$$

where ρu is the density and velocity inside the boundary layer, $\rho_e U_e$ is the density and velocity at the edge of the boundary layer, and y is in the direction normal to the surface. Another idealized thickness with equivalent momentum flow rate is called the momentum thickness, δ_2 (many use the symbol θ). Mathematically, the momentum thickness is defined as

$$\delta_2 = \int_0^\infty \frac{\rho u}{\rho_e U_e}\left(1 - \frac{u}{U_e}\right) dy. \tag{2.67}$$

Based on these idealized thicknesses, we can define shape parameters that will determine the "health" of the boundary layer:

$$H_1 = \frac{\delta - \delta_1}{\delta_2}; \tag{2.68}$$

$$H_{12} = \frac{\delta_1}{\delta_2}. \tag{2.69}$$

Viscous effects are very difficult to model analytically, so most boundary layer models are semi-empirical in nature. For this work, we will be using a well-known, widely used, semi-empirical method for our boundary layer model.

2.5.1 Head's Turbulent Boundary Layer Model

For the turbulent boundary layer, we use Head's well-known entrainment method[13]. The governing equations of the method are:

13 Head, "Entrainment in the Turbulent Boundary Layer," 1958.

$$\frac{dH_1}{ds} = \frac{0.0306}{\delta_2}(H_1 - 3)^{-0.6169} - \frac{dU_e}{ds}\frac{H_1}{U_e} - \frac{d\delta_2}{ds}\frac{H_1}{\delta_2} \tag{2.70a}$$

$$\frac{d\delta_2}{ds} = \frac{c_f}{2} - \frac{dU_e}{ds}\frac{\delta_2}{U_e}(H_{12} + 2) \tag{2.70b}$$

where H_{12} is a function of H_1 such that

$$H_{12} = \begin{cases} 0.86\,(H_1 - 3.3)^{-0.777} + 1.1 & H_1 \geq 5.3 \\ 1.1538\,(H_1 - 3.3)^{-0.326} + 0.6778 & H_1 < 5.3. \end{cases} \tag{2.71}$$

Also, c_f is defined to be

$$c_f = 0.246 \times 10^{-0.678 H_{12}} Re_{\delta_2}^{-0.268} \tag{2.72}$$

where Re_{δ_2} is the Reynolds number based on local edge velocity and momentum thickness.

2.5.2 Solving the turbulent boundary layer

We can use a standard ODE solver to determine the solution of the turbulent boundary layer system of equations, for example a 2nd order Runge-Kutta method. We determine initial conditions by starting with the momentum thickness value from the Schlichting empirical fit for a flat plate:

$$\delta_2 = \frac{0.036 s}{Re_s^{1/5}} \tag{2.73}$$

We initialize H_{12} to the value for a turbulent flat plate, 1.28, which gives us an initial H_1 of 10.6. Separation takes place as H_{12} becomes large, so a typical cutoff value for separation is 3, at which point the ODE solve is terminated.

2.5.3 Viscous Drag

Squire-Young Formula

The Squire-Young formula[14] is a well-known method for approximating the 2D viscous drag of airfoils. They show that the airfoil viscous drag coefficient can be determined from the momentum thickness of the wake far downstream of the airfoil trailing edge as

14 Squire *et al.*, "The Calculation of the Profile Drag of Aerofoils," 1937.

$$c_d = \frac{2\delta_{2_{\text{wake}}}}{c}. \tag{2.74}$$

They then derive an expression for the downstream wake momentum thickness based on values at the airfoil trailing edge:

$$\delta_{2_{\text{wake}}} = \delta_{2_{TE}} \left(\frac{U_{e_{TE}}}{U_\infty} \right)^{\frac{5+H_{12_{TE}}}{2}}. \tag{2.75}$$

Putting equations (2.74) and (2.75) together, we have the Squire-Young formula:

$$c_d = \frac{2\delta_{2_{TE}}}{c}\left(\frac{U_{e_{TE}}}{U_\infty}\right)^{\frac{5+H_{12_{TE}}}{2}}. \tag{2.76}$$

Note that equation (2.76) applies to just one side of the airfoil at a time, so we add the values associated with the top and bottom together to obtain the complete drag estimate.

Total Drag Force

To obtain the total, dimensional drag force on the duct, we apply the definition of drag coefficient to get the dimensional drag per unit length:

$$D' = \frac{1}{2}\rho V_\infty^2 c\left(c_{d_{\text{upper}}} + c_{d_{\text{lower}}}\right) \tag{2.77}$$

where c is the chord length of the duct. We then integrate the drag per unit length about the circumference of the duct, using the duct exit diameter as the characteristic length

$$D = D'\pi d_{\text{exit}} \tag{2.78}$$

2.5.4 A Simplified Drag Model for Center Bodies

Since integral boundary layer methods are developed on the assumption of 2-D bodies, those assumptions break down when we consider relatively narrow bodies of revolution such as the center body of a ducted fun. Therefore, we will use a different model for such cases. For the center body, we instead utilize a method similar to those used to approximate fuselage drag on aircraft. We take the drag coefficient for the center body (C_D) to be

$$\begin{aligned} C_D &= \frac{D}{0.5\rho V_\infty^2 S_{\text{ref}}}, \\ &= C_f f_{\text{form}} \frac{S_{\text{wet}}}{S_{\text{ref}}}; \end{aligned} \tag{2.79}$$

where ρ_∞ is the freestream density, V_∞ is the freestream velocity, C_f is the flat-plate skin-friction coefficient, f_{form} is a form factor correction, S_{wet} is the wetted area of the center body, and S_{ref} is a reference area. Setting the two expressions equal, we solve for drag as

$$D = 0.5\rho_\infty V_\infty^2 C_f f_{\text{form}} S_{\text{wet}}. \tag{2.80}$$

We use the form factor expression from Shevell [15] based on fineness-ratio (l/d):

15 Shevell, *Fundamentals of flight*, 1983.

$$f_{\text{form}} = 1 + \frac{2.8}{(l/d)^{1.5}} + \frac{3.8}{(l/d)^3}. \tag{2.81}$$

We take C_f to be the skin friction coefficient from Schlichting for a flat plate of length equal to the length of the center body and the velocity at the body trailing edge:

$$C_f = \frac{0.074}{Re_l^{0.2}}. \tag{2.82}$$

Chapter 2 References

8 Ryall, D. L. and Collins, I. F., "Design and Test of a Series of Annular Aerofoils," Reports and Memoranda 3492, Ministry of Technology Aeronautical Research Council, March 1967. cited on pp. 18, 19

9 Katz, J. and Plotkin, A., *Low speed aerodynamics*, 2nd ed. Cambridge, UK: Cambridge University Press Cambridge, UK, 2001. cited on p. 21

10 Drela, M., Youngren, H., and Sanders, S., *Ducted Fan Design Code (DFDC)*, version 0.70, December 10, 2005.URL: https://web.mit.edu/drela/Public/web/dfdc/. cited on pp. 26, 40

11 Drela, M., "XFOIL: An Analysis and Design System for Low Reynolds Number Airfoils," *Low Reynolds Number Aerodynamics*, Mueller, T. J., Ed., Berlin, Heidelberg: Springer Berlin Heidelberg, 1989, pp. 1–12. cited on p. 28

12 Fidkowski, K. J., "A Coupled Inviscid–Viscous Airfoil Analysis Solver, Revisited," en, *AIAA Journal*, vol. 60, no. 5, May 2022, pp. 2961–2971. DOI: 10.2514/1.j061341 cited on p. 28

13 Head, M. R., "Entrainment in the Turbulent Boundary Layer," Reports and Memoranda 3152, Aeronautical Research Council, September 1958. cited on p. 36

14 Squire, H. B. and Young, A. D., "The Calculation of the Profile Drag of Aerofoils," Reports and Memoranda 1838, Aeronautical Research Committee, November 1937. cited on p. 37

15 Shevell, R. S., *Fundamentals of flight*. Englewood Cliffs, N.J.: Prentice-Hall, 1983, ch. xxiv, 405 pages : illustrations ; 25 cm. cited on p. 38

A Vortex-based Rotor and Wake Model

Chapter 3

As briefly mentioned in Chapter 2, the main application in this work for the panel method is to model ducted rotors. Along with the panel method to model the duct and center body of ducted rotors, we also need to model the rotor and rotor wake. In this chapter, we address both the rotor and wake models which build on some aspects of the previous chapter as well as introduce several additional concepts.

We should note that in the last chapter we indicated the use of some concepts from the Ducted Fan Design Code (DFDC),[10] but for the most part the derivations for the panel method were completed from scratch. In this chapter, we rely heavily on concepts developed in DFDC's theory document;[10] though in many cases we provide more detail in our versions of the derivations. In addition, most of the figures in this chapter, although generated by our own efforts, are also heavily influenced by the excellent figures presented in the DFDC theory document.

10 Drela *et al.*, *Ducted Fan Design Code (DFDC)*, 2005.

10 Drela *et al.*, *Ducted Fan Design Code (DFDC)*, 2005.

3.1 Reference Frames

To begin , we need to start with an explanation of the various reference frames and velocity decompositions used in the rotor and wake models. We introduce multiple reference frames, because we would like to perform our analysis in steady frames. The first frame we will use is the absolute reference frame, which is the reference frame of an observer stationed at a static location on the duct wall (the same reference frame introduced briefly in Chapter 2). Since the aerodynamics of rotors are inherently unsteady, we cannot perfectly model things as steady. If we change our reference frame to be relative to a blade as we pass across the rotor disk, however, we can reasonably approximate the flow across the blade section as steady. In this blade relative—or simply relative—reference frame, the observer is stationed on a blade such that to the observer the blade is stationary.

3.1.1 Absolute Frame

Along with the absolute reference frame, we re-iterate the absolute coordinate system introduced in the previous chapter in figure 3.1 showing a meridional view of the ducted rotor. As can be seen, the duct is defined in a right-handed cylindrical coordinate system. We define the z-axis to be along the axis of symmetry (also the center line/axis of rotation for the rotor(s)), positive in the downstream direction. The

r-axis is positive from the center line outward. Finally, θ is positive about the z-axis according to the right-handed system. We choose the origin to be located on the z axis, aligned with the foremost rotor plane.

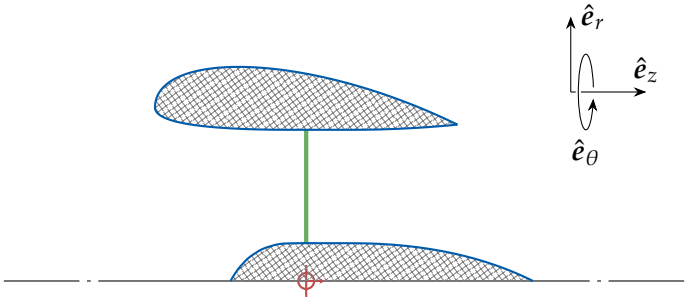

Figure 3.1: Meridional view showing the absolute reference frame. Example duct and center body geometry is shown in blue, the origin location is shown in red, and an example blade lifting line location is shown in green.

3.1.2 Relative Frame

It may be helpful to initially think of the relative reference frame as orthogonal to the slice of the absolute frame shown in figure 3.1. Imagine standing on the blade looking from the direction of the duct wall toward the rotor hub (in the negative r direction). In turbo-machinery conventions, the z-r slice of figure 3.1 is the meridional view, and the m-θ slice of figure 3.2 is the cascade view. We can use this cascade view to understand the various velocity decompositions through which we can relate the absolute and relative reference frames. The blade rotates in the positive θ direction, and the m axis (where $dm^2 = dz^2 + dr^2$) is along a streamline passing through the lifting line representing the blade. That is to say, the m axis is the meridional axis, which may or may not be orthogonal to r for a given blade element.

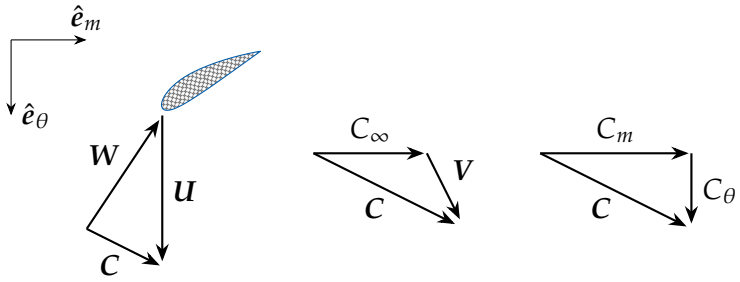

Figure 3.2: Cascade view showing the blade element relative frame with velocity decompositions.

3.1.3 Velocity Decomposition and Definition

The velocity triangles in figure 3.2 show how the various velocity components are combined into useful quantities. The components that give us the absolute local velocity, $\boldsymbol{C}$, include: the freestream velocity, $\boldsymbol{C}_\infty$,[a] and the velocity induced by the rotors and duct, $\boldsymbol{V}$. Together, we have

[a] We will assume according to axisymmetry that $\boldsymbol{C}_\infty = ||\boldsymbol{C}_\infty||\hat{z}$.

$$\boldsymbol{C} = C_\infty \hat{z} + \boldsymbol{V} \tag{3.1}$$

The relative velocity, $\boldsymbol{W}$, is comprised of the absolute velocity, $\boldsymbol{C}$, plus the rotational velocity at the respective radial station along the blade, $\boldsymbol{U} = \Omega r \hat{\theta}$;

$$\begin{aligned} \boldsymbol{W} &= \boldsymbol{C} - \boldsymbol{U} \\ &= \boldsymbol{C} - \Omega r \hat{\theta}. \end{aligned} \tag{3.2}$$

It will be useful to put both $\boldsymbol{C}$ and $\boldsymbol{W}$ in terms of m and r. We get the velocities in terms of m and r by first separating out the various velocity components in the absolute reference frame and applying the definition of the meridional axis. The velocity in the absolute frame is broken down into its various components as

$$\begin{aligned} C_z &= V_z + C_\infty \\ C_r &= V_r \\ C_\theta &= V_\theta. \end{aligned} \tag{3.3}$$

Similarly, the relative velocity is broken down as[b]

$$\boxed{\begin{aligned} W_z &= V_z + C_\infty \\ W_r &= V_r \\ W_\theta &= V_\theta - \Omega r. \end{aligned}} \tag{3.4}$$

[b] In addition to the blue shaded boxes introduced in the last chapter, we will additionally use gray boxes for orientation in this chapter. The gray boxes indicate expressions that are not used immediately in the derivations of this chapter, but will be referenced in later sections of our development. Note that expressions used immediately will not be boxed unless they are also needed later.

These decompositions immediately yield the θ components of the velocities. To obtain the meridional component, we can use the definition of the meridional coordinate, that is, the direction tangent to the mean streamline in the $z - r$ (meridional) plane, to see that

$$\boldsymbol{C}_m = \boldsymbol{W}_m = C_z \hat{z} + C_r \hat{r}. \tag{3.5}$$

Now we have all the pieces to express the relative velocities in terms of the blade element frame (see the right-most velocity triangle in figure 3.2):

$$\boldsymbol{C} = ||\boldsymbol{C_m}||\hat{m} + C_\theta \hat{\theta} \tag{3.6}$$

$$\boldsymbol{W} = ||\boldsymbol{C_m}||\hat{m} + (C_\theta - \Omega r)\hat{\theta} \tag{3.7}$$

3.2 A Blade Element Model

To model the rotor, we use a blade element based model in which we look at elements, or sections, of the blade individually. We take average 2-D section properties for each of these blade elements in order to determine the blade circulation distribution as well as approximate profile drag. For each 2-D section, we use typically use a lookup table (though direct computation is possible) to determine the lift and drag coefficients based on the local blade element geometry and flow as shown in figure 3.3. In

the case of a low-solidity blade element, we can simply use airfoil data based on the aerodynamic angle of attack, α, which is the inflow angle, β_1 minus the local blade element stagger angle, γ_{be}:

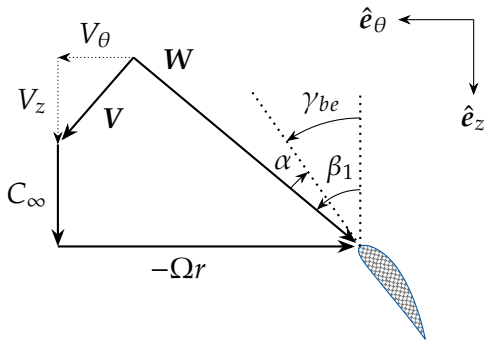

Figure 3.3: Velocity decomposition with angles in the blade element frame.

$$\alpha = \beta_1 - \gamma_{be}, \tag{3.8}$$

where the inflow angle is defined as

$$\beta_1 = \arctan \frac{-W_\theta}{W_z} = \arctan \frac{\Omega r - V_\theta}{C_\infty + V_z}, \tag{3.9}$$

or in other words, the angle from the axis of rotation to the local inflow velocity vector, $\boldsymbol{W}$, as seen in figure 3.3.

For higher solidity rotors, when cascade data is available, we look up the lift and drag coefficients based on the inflow and stagger angles directly. In addition, the section lift and drag coefficients may depend not only on the local angle of attack (or stagger and inflow angles), but may also be a function of the local solidity (σ_{be}), Reynolds number (Re_{be}), and Mach (M_{be}) number which we define in the typical manner:

$$\sigma_{be} = \frac{Bc}{2\pi r}, \tag{3.10}$$

$$Re_{be} = \frac{\rho_\infty W c}{\mu_\infty}, \tag{3.11}$$

and

$$M_{be} = \frac{W}{a_{s_\infty}}, \tag{3.12}$$

where B is the number of rotor blades, and ρ_∞, μ_∞, and a_{s_∞} are the freestream density, dynamic viscosity, and speed of sound, respectively. Also, W and c are the local (at a given radial station, r) inflow magnitude and blade element chord length.

3.2.1 Blade Circulation

To get circulation for each blade element, we treat the rotor blade as a lifting line and assume that:

Assumption 3.1

The rotor can reasonably be modeled as a lifting line such that local blade circulation can be expressed according to the Kutta-Joukowski theorem, which states:

$$\boldsymbol{F} = \rho \boldsymbol{W} \times \boldsymbol{\Gamma}$$

Limitations: We require the blade to be modeled as a single line, and therefore we don't quite capture the full detail of flow turning across the blades.

Justification: This simplification allows for a more straightforward approach to the rotor-wake modeling, again reducing the computational complexity.

Modeling the rotor blades as lifting lines, if we take the velocity to be the local inflow velocity magnitude, $W = \left[W_z^2 + W_\theta^2\right]^{1/2}$ at the radial point of interest, we can take the perpendicular component of the force to be lift also at the radial point of interest. We can then rearrange the expression for the Kutta-Joukowski theorem in assumption 3.1 for the local circulation magnitude, $\Gamma(r)$, along the blade as

$$\Gamma(r) = \frac{L'}{\rho W}. \tag{3.13}$$

As mentioned, for each blade section we prescribe an airfoil polar such that the lift coefficient is known for a given angle of attack. If we then take the expression for the two-dimensional coefficient of lift—

$$c_\ell = \frac{2L'}{\rho W^2 c}, \tag{3.14}$$

where c is the blade element chord length, and c_ℓ is the local blade element lift coefficient— and substitute into our expression for circulation (again using the local meridional velocity), we arrive at

$$\boxed{\Gamma(r) = \frac{1}{2} W c c_\ell,} \tag{3.15}$$

where W, c, and c_ℓ are all functions of the radial position, r, along the rotor.

3.2.2 Rotor Profile Drag

We define the rotor blade section profile drag per unit length in terms of a local airfoil polar drag coefficient using similar logic to how we defined the circulation due to lift. Though we are actually attempting to approximate a viscous effect inviscidly, so we are effectively equating the vorticity that would be introduced into the wake due to viscous profile drag with an approximate inviscid source distribution on the blade.

Assumption 3.2

The rotor blade section profile drag can be approximated by the addition of source elements along the rotor blade.

Limitations: We aren't fully modeling viscous effects in the wake.

Justification: This allows us to model the wake inviscidly (which allows us to simplify the wake model later), while still approximating the viscous effects of the rotor on the wake velocities. It also enables the use of source panels, providing straightforward coupling with the bodies modeled with panel methods.

The inviscid approximation of the profile drag per unit length takes a similar form to the local circulation:

$$\Sigma = \frac{1}{2} W c c_d \tag{3.16}$$

where c_d is the blade element drag coefficient at the angle of attack described in section 3.2.1, and again, each of the terms on the right hand side are functions of the radial position along the blade. To get the total source sheet strength per unit length, we smear the total source strength per unit span of all the blades, B, around the circumference, 2π:

$$\sigma = \frac{B\Sigma}{2\pi}. \tag{3.17}$$

Therefore the expression for the smeared rotor source strength per unit length along the blade is

$$\boxed{\sigma = \frac{B}{4\pi} W c c_d.} \tag{3.18}$$

3.3 A Smeared Vortex Sheet Model

For a given position on a blade producing a circulation change, $\Delta\Gamma$, by conservation of circulation, a helical vortex filament of strength $-\Delta\Gamma$ is shed into the flow. In order to represent 3D vortex filaments in our axisymmetric reference frames, we will also make the approximation that they can be smeared into equivalent axisymmetric vortex sheets in the m and θ directions.

Assumption 3.3

Three-dimensional helical vortex filaments can be represented in a smeared axisymmetric model.

Limitations: We are not caputuring the full 3D and unsteady effects of the wake.

Justification: We will see that we can develop a model that works

very well with the panel method formulation of the solid body aerodynamics.

The smeared axisymmetric vortex sheets then have circulation to length ratios (densities) of γ_m and γ_θ in their respective directions. Because we are modeling the wake internal to the duct, we cannot guarantee a cylindrical wake, and therefore cannot simply model the wake with straight vortex cylinders. Will will still use the concept of a wake cylinder, however to help us model discrete sections of the wake; so we continue with a description of how we smear a helical vortex filament into a cylindrical sheet.

3.3.1 Starting with a Standard Wake Screw

We begin with a shed vortex sheet, the geometry of which we approximate by a left-handed helix such that the helical sheet is defined parametrically in terms of the variable $\bar{t}$ as

$$r(\bar{t}) = r, \quad \theta(\bar{t}) = -\bar{t}, \quad z(\bar{t}) = \bar{t}\ell, \tag{3.19}$$

in polar coordinates; where ℓ is the torsional parameter describing the distance traveled in the z direction relative to the angle traveled in θ:

$$\ell = \frac{h}{2\pi} = \frac{\mathrm{d}z}{-\mathrm{d}\theta}, \tag{3.20}$$

where h is the pitch of the helix, defined as the distance traveled in z for one rotation of the rotor blade, in other words, the distance traveled in z after traveling circumferentially $2\pi r$

$$h = 2\pi r\frac{\ell}{r} = 2\pi r\frac{\mathrm{d}z}{-r\mathrm{d}\theta} = 2\pi\frac{\mathrm{d}z}{-\mathrm{d}\theta}. \tag{3.21}$$

Given the polar coordinates, we can define the pitch angle of the helix such that the tangent of that angle is the ratio of the distance traveled in z to the distance traveled circumferentially

$$\tan\phi = \frac{\mathrm{d}z}{-r\mathrm{d}\theta} = \frac{\ell}{r}. \tag{3.22}$$

From the pitch, we can obtain the apparent pitch, or the distance between the helix sheets created by consecutive blades by dividing the pitch by the number of blades, B,

$$h_B = \frac{2\pi}{B}\frac{\mathrm{d}z}{-\mathrm{d}\theta}. \tag{3.23}$$

If we now assume that:

Assumption 3.4

Vortex filaments are shed parallel to the relative inflow velocity, $\mathbf{W}$.

Limitations: This is a simplified modeling approach that ignores the some of the flow turning of the blade.

Justification: By using this lifting line approach rather than some other approach, such as a lifting surface, we (like many of our other assumptions) simplify the model, allowing for simpler implementation and faster computation.

In other words, we assume that the local $\mathrm{d}z$ is in the direction of $\hat{\boldsymbol{e}}_m$, and likewise $\mathrm{d}\theta$ in the direction of $\hat{\boldsymbol{e}}_\theta$ as per figure 3.2, we obtain the non-dimensional length in the m direction for defining the γ_θ strength density

$$h_B \approx \frac{2\pi}{B}\left(\frac{W_m}{-W_\theta}\right). \tag{3.24}$$

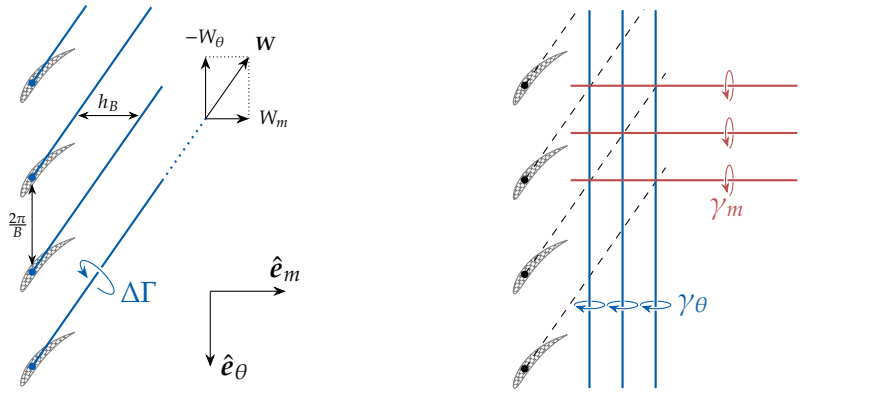

(a) Wake Screw Geometry. **(b)** Axisymmetric Smeared Cylinder.

Figure 3.4: 2D vortex sheets are generated from ratios of circulation to lengths between vortex sheets.

Figure 3.4 shows graphically the wake screw non-dimensional geometry and orientation of the smeared vorticity. To dimensionalize the lengths for a given smeared cylindrical surface, we multiply by the cylinder radius, r, to obtain the dimensional length. In addition, as we have defined our tangential vortices (see equation (2.11)) to be positive in the positive θ direction (the negative $\bar{t}$ direction), we need to apply an additional negative to ensure our vortices are oriented correctly in the context of the wake. Thus

$$\gamma_\theta = -\frac{-\Delta\Gamma}{h_B r} = -\Delta\Gamma\frac{B}{2\pi r}\left(\frac{W_\theta}{W_m}\right). \tag{3.25}$$

To obtain an expression for γ_m we look at the distance between blades in the $\bar{t}$ direction, we know that the non-dimensional distance between the blade sections is the distance about $\bar{t}$ divided by the number of blades (assuming even blade spacing), $2\pi/B$. For a given smeared cylinder of radius, r, we multiply by r to obtain the dimensional distance, $2\pi r/B$. To keep the vortices oriented positively in our reference frame, we need

to apply an additional negative.Applying this additional negative the meridional vortex strength density (strength per unit length), γ_m, is

$$\gamma_m = \Delta\Gamma \frac{B}{2\pi r}. \tag{3.26}$$

Our expression for γ_m is generally applicable for steady state conditions if we use the local circulation jumps across the wake at any given point. Due to conservation of circulation, we know the circulation jumps anywhere downstream. On the other hand, γ_θ would only be generally applicable if we assumed that the Ωr component of W_θ (see equation (3.4)) was constant in the entire wake. In actuality, we only know Ωr right at the rotor lifting line, but not generally in the remainder of the wake. We therefore want to develop a more general expression for γ_θ based on requiring the wake to be force-free, or in other words, we demand static pressure continuity across the vortex sheets. The somewhat lengthy derivation for this more general expression for γ_θ comprises the rest of section 3.3.

The following subsections will gradually assemble the pieces required to arrive at a final expression. As a reminder, we will use blue boxes around equations to indicated expressions that are required for code implementation. As previously noted, we will use gray boxes to indicate expressions that are not used in code implementation, but are referenced later (typically much later) in the derivation.

3.3.2 Piece 1: Swirl/Circulation Relation

The first piece we need is a relationship between the swirl velocity and the circulation. The swirl velocity induced by upstream rotor blades, V_θ, can be determined by applying Stokes'[c] and Kelvin's[d] theorems.

[c] $\iint_S \nabla \times \boldsymbol{V} \mathrm{d}^2\mathcal{S} = \Gamma = \oint_{\delta S} \boldsymbol{V} \mathrm{d}s$

[d] $\frac{D\Gamma}{Dt} = \frac{\partial \Gamma}{\partial t} + \boldsymbol{V} \cdot \nabla\Gamma = 0$

If we define a control volume around a streamtube as shown in figure 3.5, where the first curve is taken about all upstream rotors along a streamline, and the second curve is taken about the axis of rotation, only in the r-θ plane with radius such that the edge of the contour lies on the same streamline upon which the first curve lies (see the dotted line in figure 3.5), we see by Kelvin's theorem (conservation of circulation), that the circulation due to the upstream rotors can be related to the tangential velocity downstream of the rotors through Stokes' theorem:

$$\widetilde{\Gamma} = \oint_0^{2\pi} \boldsymbol{V} \cdot r \mathrm{d}\boldsymbol{\theta}, \tag{3.27}$$

where $\widetilde{\Gamma}$ is the net circulation contribution of all the blades of the upstream rotors:

$$\widetilde{\Gamma} = \sum_{i=1}^{N} B_i \Gamma_i. \tag{3.28}$$

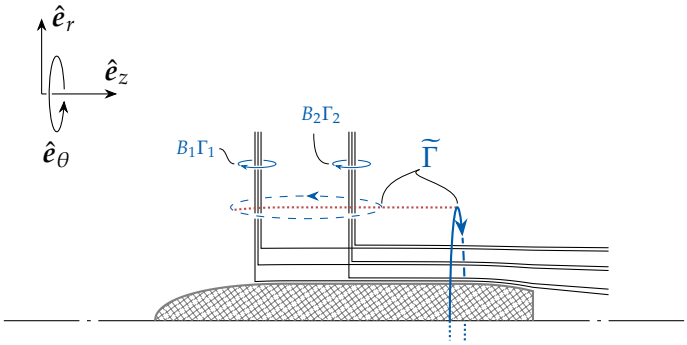

Figure 3.5: Circulation is conserved between the dashed and solid contours, noting the red dotted line indicating the streamline on which the $\widetilde{\Gamma}$ contours align. The integral over the contour about the axis of rotation yields V_θ in terms of $\widetilde{\Gamma}$.

Performing the integration for a give radial position and rearranging for V_θ[e] gives

$$V_\theta = C_\theta = \frac{\widetilde{\Gamma}}{2\pi r}, \tag{3.29}$$

where V_θ in our smeared, axisymmetric model is the circumferentially averaged swirl velocity induced by upstream rotors

For the self-induced case, the contour is placed at the rotor plane. This means that the rotor "sees" infinite trailing vortices from any upstream rotors, but only semi-infinite trailing vortices for itself. Thus the rotor experiences the full swirl induced by upstream rotors, but only half of its own swirl contribution:

$$(V_\theta)_{\text{self}} = \frac{1}{2\pi r}\left(\widetilde{\Gamma} + \frac{1}{2}B\Gamma\right), \tag{3.30}$$

where $B\Gamma$ here is the number of blades and circulation of the rotor itself.

3.3.3 Piece 2: Velocity Jumps

The next piece of the puzzle relates velocity jumps to vorticities per unit length on wake sheets. The smeared sheet strengths of equations (3.25) and (3.26) can be defined in terms of velocity jumps across the sheets.[f] Starting with equation (3.26), we can split the $\Delta\Gamma$ into $\Gamma_2 - \Gamma_1$ (taking $\widetilde{\Gamma} = B\Gamma$ for the single rotor) for a given vortex sheet

$$\begin{aligned}\gamma_m &= \frac{\Delta\widetilde{\Gamma}}{2\pi r} \\ &= \frac{B(\Gamma_2 - \Gamma_1)}{2\pi r}.\end{aligned} \tag{3.31}$$

Then using equation (3.29)

[e] Note that the θ component of V is the only component aligned with $d\boldsymbol{\theta}$ and is circumferentially constant due to our smearing approxmation. In addition the contour is a circle, so the integral is determined immediately.

[f] Assuming here that the velocities in this subsection are the equivalent inviscid flow velocities resulting from replacing viscous rotor pressure drag effects with rotor source distributions in section 3.2.2.

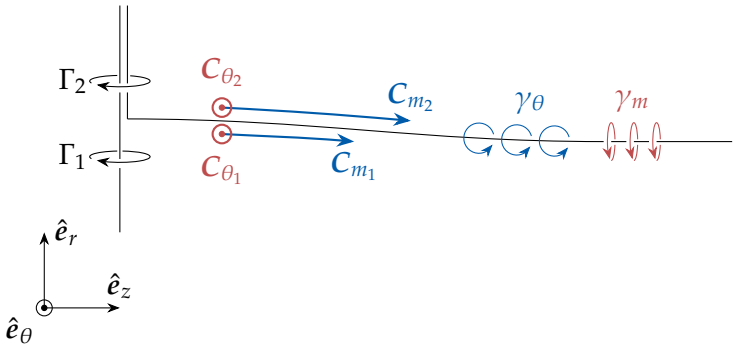

Figure 3.6: Vorticity per unit length can be related to velocity jump across axisymmetric vortex sheets.

$$C_{\theta_2} - C_{\theta_1} = \frac{B(\Gamma_2 - \Gamma_1)}{2\pi r}; \tag{3.32}$$

which we can then substitute in to get the sheet strength in terms of the velocity jump:

$$\boxed{\gamma_m = \frac{B(\Gamma_2 - \Gamma_1)}{2\pi r} = C_{\theta_2} - C_{\theta_1}.} \tag{3.33}$$

As it so happens, in general for inviscid flows, the jump in tangential velocity across a vortex sheet is equal to the sheet vorticity per unit length. Therefore we can similarly equate equation (3.25) to a jump in the meridional velocities across the vortex sheet:

$$\boxed{\gamma_\theta = -\frac{B(\Gamma_2 - \Gamma_1)}{2\pi r}\frac{W_{\theta_{\text{avg}}}}{W_{m_{\text{avg}}}} = C_{m_1} - C_{m_2}.} \tag{3.34}$$

where, to obtain the relative velocity components on the sheet, we combine the blade relative velocities just to either side of the sheet into averages, W_{avg}, as

$$W_{\theta_{\text{avg}}} \equiv \frac{1}{2}(W_{\theta_1} + W_{\theta_2}) = \frac{1}{2}(C_{\theta_1} + C_{\theta_2} - 2\Omega r) \tag{3.35}$$

$$W_{m_{\text{avg}}} \equiv \frac{1}{2}(W_{m_1} + W_{m_2}) = \frac{1}{2}(C_{m_1} + C_{m_2}). \tag{3.36}$$

If we divide equation (3.33) by equation (3.34), we get

$$W_{m_{\text{avg}}}\gamma_\theta + W_{\theta_{\text{avg}}}\gamma_m = 0. \tag{3.37}$$

Substituting in the average velocities from equations (3.35) and (3.36) then gives

$$\frac{1}{2}(C_{m_1} + C_{m_2})\gamma_\theta + \frac{1}{2}(C_{\theta_1} + C_{\theta_2} - 2\Omega r)\gamma_m = 0. \tag{3.38}$$

Then applying the definitions of the vortex strengths from equations (3.33) and (3.34) yields

$$\frac{1}{2}(C_{m_1} + C_{m_2})(C_{m_2} - C_{m_1}) + \frac{1}{2}(C_{\theta_1} + C_{\theta_2} - 2\Omega r)(C_{\theta_2} - C_{\theta_1}) = 0. \quad (3.39)$$

Simplifying

$$\frac{1}{2}\left(C_1^2 - C_2^2\right) = -(C_{\theta_1} - C_{\theta_2})\Omega r \quad (3.40)$$

where $C^2 = C_m^2 + C_\theta^2$. Then applying the definition in equation (3.32) (and multiplying both sides by -1),

$$\boxed{\frac{1}{2}\left(C_2^2 - C_1^2\right) = -\frac{B(\Gamma_2 - \Gamma_1)}{2\pi}\Omega.} \quad (3.41)$$

3.3.4 Piece 3: Thermodynamic Pressure Relationships

The largest piece in assembling a general expression for the tangential vortex sheet strength encompasses thermodynamic pressure relations for total and static pressures.

Total Pressure To determine the pressure relationships, we begin with the understanding that a rotor induces downstream changes in total enthalpy and entropy which are accompanied by changes in total pressure. We can relate these changes in pressure, enthalpy, and entropy through the first and second laws of thermodynamics as follows.

The first law of thermodynamics expressed in terms of enthalpy and in differential form is:

$$\mathrm{d}q = \mathrm{d}h - v\mathrm{d}p_t \quad (3.42)$$

where q is specific heat, h is specific entropy, v is specific volume and p_t is total pressure. The second law of thermodynamics, assuming an idealized (reversible) process, is expressed in differential form as:

$$T\mathrm{d}s = \mathrm{d}q \quad (3.43)$$

where T is total temperature, and s is specific entropy. Plugging the second law (equation (3.43)) into the first law (equation (3.42)) gives:

$$Tds = \mathrm{d}h - v\mathrm{d}p_t \quad (3.44)$$

Which is a form of Gibb's equation in terms of enthalpy and is expression relating pressure, enthalpy, and entropy. We will now, however, work from equation (3.44) to arrive at a simpler and more useful expression for our application. First, we'll isolate entropy on the left hand side for convenience.

$$\mathrm{d}s = \frac{\mathrm{d}h}{T} - \frac{v\mathrm{d}p_t}{T}. \tag{3.45}$$

Moving away from using enthalpy briefly, we will assume:

Assumption 3.5

The fluid is a calorically perfect gas.

Limitations: The specific heat capacity is constant.

Justification: Our application is primarily at low Mach flows in electric ducted fans, for which air can reasonably be modeled as a calorically perfect gas. This allows us to obtain a simple relation between change in enthalpy, entropy, and pressure.

In which case, we can relate enthalpy and temperature in both the following ways:

$$\mathrm{d}h = c_p \mathrm{d}T \tag{3.46}$$
$$h = c_p T, \tag{3.47}$$

where c_p here is the specific heat. Substituting equation (3.46)[g] into equation (3.45), we have

[g] note that since the rest of the terms are still in differential form, we cannot directly use equation (3.47) at this point.

$$\mathrm{d}s = \frac{c_p \mathrm{d}T}{T} - \frac{v\mathrm{d}p_t}{T}. \tag{3.48}$$

If we also apply the ideal gas law,

$$v = \frac{RT}{p_t}, \tag{3.49}$$

to the last term, we have

$$\mathrm{d}s = c_p \frac{\mathrm{d}T}{T} - R\frac{\mathrm{d}p_t}{p_t}. \tag{3.50}$$

We then integrate equation (3.50) from the ambient to local conditions:

$$\begin{aligned} \int_{s_\infty}^{s} \mathrm{d}s &= c_p \int_{T_\infty}^{T} \frac{\mathrm{d}T}{T} - R \int_{p_{t_\infty}}^{p_t} \frac{\mathrm{d}p_t}{p_t} \\ s - s_\infty &= c_p \ln\left(\frac{T}{T_\infty}\right) - R \ln\left(\frac{p_t}{p_{t_\infty}}\right). \end{aligned} \tag{3.51}$$

Next, we want to bring enthalpy back into the picture. To do so, we now utilize equation (3.47), multiplying the temperatures by c_p to get back into terms of specific enthalpy

$$s - s_\infty = c_p \ln\left(\frac{h}{h_\infty}\right) - R \ln\left(\frac{p_t}{p_{t_\infty}}\right). \tag{3.52}$$

If we now define changes relative to the (far upstream) freestream values (∞ subscripts) as:

$$\widetilde{p_t} = p_t - p_{t_\infty} \tag{3.53}$$
$$\widetilde{h} = h - h_\infty \tag{3.54}$$
$$\widetilde{s} = (s - s_\infty)/R, \tag{3.55}$$

then we can express equation (3.52) as[h]

$$\widetilde{s} = \frac{c_p}{R} \ln\left(1 + \frac{\widetilde{h}}{\widetilde{h}_\infty}\right) - \ln\left(1 + \frac{\widetilde{p}_t}{\widetilde{p}_{t_\infty}}\right). \tag{3.56}$$

[h] Remembering that for x/y, subtracting and adding $1 = y/y$ gives $(x-y)/y + y/y = (x-y)/y + 1$

Now we will assume that

Assumption 3.6

The Mach number is sufficiently low such that

$$\frac{\widetilde{p_t}}{p_{t_\infty}} \ll 1 \tag{3.57}$$
$$\frac{\widetilde{h}}{h_\infty} \ll 1 \tag{3.58}$$
$$\widetilde{s} \ll 1, \tag{3.59}$$

Limitations: We are limited to low mach number regimes.

Justification: We can simplify the relationship between entropy, enthalpy, and pressure, again allowing for a simpler methodology and faster computation.

With assumption 3.6 we can simplify equation (3.56) by noting that the Taylor series expansion for a logarithm is

$$\ln(x) = (x-1) + \frac{1}{2}(x-1)^2 + \text{higher order terms}, \tag{3.60}$$

if $x \approx 1$. Therefore, by assumption 3.6, we can simplify equation (3.56) using the first term in Taylor series approximations of each of the logarithm terms. If we then apply equation (3.47) and the ideal gas law, we are left with

$$\boxed{\widetilde{p_t} \simeq \rho\left(\widetilde{h} - \widetilde{S}\right),} \tag{3.61}$$

where

$$\widetilde{S} \equiv \frac{p_{t_\infty}}{\rho_\infty}\widetilde{s}, \tag{3.62}$$

where ρ is the air density, and for our steady, low Mach application, p_{t_∞}/ρ_∞ is nearly constant, so we can convect $\widetilde{S}$ downstream in place of $\widetilde{s}$. Therefore we end up seeing that the total pressure at any point in the rotor wake is the freestream total pressure plus any upstream work or losses:

$$p_t = p_{t_\infty} + \rho\left(\widetilde{h} - \widetilde{S}\right) \tag{3.63}$$

Static Pressure The static pressure, p_s, is the total pressure minus the dynamic pressure:

$$p_s = p_t - \frac{1}{2}\rho V_{visc}^2. \tag{3.64}$$

Substituting in from equation (3.63) gives us

$$p_s = p_{t_\infty} - \frac{1}{2}\rho V_{visc}^2 + \rho\left(\widetilde{h} - \widetilde{S}\right), \tag{3.65}$$

where V_{visc} is the real viscous flow velocity. Rather than finding the full viscous flow field, which (among other things) would require more costly wake treatment, we can use the equivalent inviscid flow velocity, V_{inv}, through the addition of a source sheet at the drag elements in the flow (see assumption 3.2), removing the need for trailing vortex sheets for drag elements. Using the equivalent inviscid flow simply eliminates entropy from equation (3.65)

$$\boxed{p_s = p_{t_\infty} - \frac{1}{2}\rho V_{inv}^2 + \rho\widetilde{h}.} \tag{3.66}$$

3.3.5 Piece 4: Disk and Sheet Jumps

The final piece we need includes the enthalpy jumps across rotor disks and pressure jumps across the wake sheets.

Enthalpy Jumps The specific work, w_c, done by a rotor is related to a jump in enthalpy across the rotor. As such, we can obtain $\widetilde{h}$ as the accumulation of changes in enthalpy across upstream disks.

$$\boxed{\widetilde{h} = \sum_{i=1}^{N} \Delta h_{\text{disk}_m}} \tag{3.67}$$

where the jump relation Δh_{disk} is defined according to the Euler turbine equation:

$$\Delta h_{\text{disk}} = w_c = \Omega\Delta(rC_\theta). \tag{3.68}$$

We can relate the jump in enthalpy to the circulation by applying our lifting line assumption (assumption 3.1), which means that there is no

radial deviation in flow across the blade, as well as substituting in for C_θ from equation (3.29) (for a single disk).

$$\Delta h_{\text{disk}} = \Omega r C_\theta = \Omega \frac{B\Gamma}{2\pi}. \tag{3.69}$$

Pressure Jumps Using equation (3.66), we see the jump in static pressure across a vortex sheet is

$$p_{s_2} - p_{s_1} = -\frac{1}{2}\rho\left(V_{inv_2}^2 - V_{inv_1}^2\right) + \rho\left(\widetilde{h}_2 - \widetilde{h}_1\right). \tag{3.70}$$

If we substitute equation (3.69) in for the enthalpy terms, and equation (3.41) for the velocity terms in equation (3.70), we can simplify as follows

$$p_{s_2} - p_{s_1} = -\rho\frac{B(\Gamma_2 - \Gamma_1)}{2\pi}\Omega + \rho\frac{B(\Gamma_2 - \Gamma_1)}{2\pi}\Omega \tag{3.71}$$

$$p_{s_2} - p_{s_1} = 0 \tag{3.72}$$

which shows that there is no static pressure jump across the sheet, as we originally required to have a force-free wake.

3.3.6 Putting the Pieces Together: The Tangential Vortex Sheet Strength

As promised at the end of section 3.3.1, we are finally posed to obtain a general expression for the tangential vortex sheet strength, γ_θ. Just as a reminder, we've needed all this preparation because the tangential sheet strength at an arbitrary downstream location is not generally equal to the value just behind the rotor disk. This is because we don't automatically know what the Ωr portion of the tangential velocity is anywhere except right at the rotor disk. Thus we have used the zero static pressure jump across the wake sheet as our condition for finding a general term for γ_θ. We'll begin with equation (3.70), setting the pressure jump to zero, as is physical, and divide out the density (assumed to be constant in our low Mach case) to obtain

$$\frac{1}{2}\left(C_2^2 - C_1^2\right) = \widetilde{h}_2 - \widetilde{h}_1. \tag{3.73}$$

Expanding out the left hand side gives

$$C_{m_2}^2 - C_{m_1}^2 + C_{\theta_2}^2 - C_{\theta_1}^2 = 2\left(\widetilde{h}_2 - \widetilde{h}_1\right). \tag{3.74}$$

Applying equation (3.29) for the C_θ terms:

$$C_{m_2}^2 - C_{m_1}^2 = -\left(\frac{1}{2\pi r}\right)^2\left(\widetilde{\Gamma}_2^2 - \widetilde{\Gamma}_1^2\right) + 2\left(\widetilde{h}_2 - \widetilde{h}_1\right). \tag{3.75}$$

To get the general expression for γ_θ, we have two options: if C_{m_2} is known, then using equation (3.34)

$$\gamma_\theta = C_{m_1} - C_{m_2}, \tag{3.34}$$

where from equation (3.75)

$$C_{m_1}^2 = C_{m_2}^2 + \left(\frac{1}{2\pi r}\right)^2 \left(\widetilde{\Gamma}_2^2 - \widetilde{\Gamma}_1^2\right) - 2\left(\widetilde{h}_2 - \widetilde{h}_1\right), \tag{3.76}$$

gives us our general expression. We can march equation (3.76) radially inward, starting with $C_{m_2} = C_\infty$ just outside the outermost vortex sheet. On the other hand, if $C_{m_{\text{avg}}}$ is known instead, we can still use equation (3.75) to obtain γ_θ as follows:

$$C_{m_{\text{avg}}} = \frac{1}{2}\left(C_{m_1} + C_{m_2}\right) \tag{3.77}$$

$$C_{m_2}^2 - C_{m_1}^2 = \left(C_{m_1} + C_{m_2}\right)\left(C_{m_2} - C_{m_1}\right). \tag{3.78}$$

Substituting from equation (3.34)

$$C_{m_2}^2 - C_{m_1}^2 = -\left(C_{m_1} + C_{m_2}\right)\gamma_\theta. \tag{3.79}$$

Substituting from equation (3.77)

$$C_{m_2}^2 - C_{m_1}^2 = -2C_{m_{\text{avg}}}\gamma_\theta. \tag{3.80}$$

Rearranging for γ_θ and substituting from equation (3.75):

$$\boxed{\gamma_\theta = -\frac{1}{2C_{m_{\text{avg}}}}\left(-\left(\frac{1}{2\pi r}\right)^2 \left(\widetilde{\Gamma}_2^2 - \widetilde{\Gamma}_1^2\right) + 2\left(\widetilde{h}_2 - \widetilde{h}_1\right)\right).} \tag{3.81}$$

3.4 A Streamlined Elliptic Grid

The question we must now ask ourselves is *where* is equation (3.81) applied? We may first think to model the rotor wake by integrating equation (3.81) along streamlines, which could be done. Though in each iteration of the solve, the streamline location would need to be determined and then the circulation along the streamline would need to be integrated. An alternative method, which we take, is to determine the approximate locations of the streamlines as a pre-process before the solve and place discretized wake sheets along them, forming a set of vortex panels with strengths determined from equation (3.81). By so doing, we complete a large portion of the computation related to the wake outside of the iterative solver, greatly reducing computational cost. We utilize a method from Thompson *et al.* to determine approximate streamline locations based on the duct and centerbody geometries and blade element positions along the rotor lifting line.

In the method of Thompson *et al.* a transformation is defined between rectangular and arbitrary shaped regions, with the arbitrary shaped

16 Thompson *et al.*, "Automatic numerical generation of body-fitted curvilinear coordinate system for field containing any number of arbitrary two-dimensional bodies," 1974.

region lying on a physical plane.[16] By taking the coordinates of the rectangular region to be the solutions of an appropriate elliptic boundary value problem, with one of the coordinates being constant along the boundaries, we can obtain a transformation from a grid in the rectangular space to a useful grid in the physical space. In our case, we will define a Poisson equation based on the axisymmetric stream function and set one of the rectangular coordinates to be constant along the body boundaries, and therefore the streamlines.

3.4.1 A Poisson Equation from the Axisymmetric Stream Function

The z and r components of absolute velocity can be defined in terms of the axisymmetric stream function, $\psi(z, r)$, as

$$C_z = \frac{1}{\rho r}\frac{\partial \psi}{\partial r} \tag{3.82a}$$

$$C_r = \frac{-1}{\rho r}\frac{\partial \psi}{\partial z} \tag{3.82b}$$

where ρ is the air density. Additionally, the circumferential vorticity is defined as

$$\omega_\theta \equiv \frac{\partial C_z}{\partial r} - \frac{\partial C_r}{\partial z}. \tag{3.83}$$

If we plug equation (3.82) into equation (3.83), and apply the chain rule, we arrive at

$$\omega_\theta = \frac{1}{\rho r}\left(\frac{\partial^2 \psi}{\partial z^2} + \frac{\partial^2 \psi}{\partial r^2}\right) + \frac{\partial \psi}{\partial z}\frac{\partial}{\partial z}\left(\frac{1}{\rho r}\right) + \frac{\partial \psi}{\partial r}\frac{\partial}{\partial r}\left(\frac{1}{\rho r}\right). \tag{3.84}$$

which we can rearrange into a Poisson equation for ψ:

$$\nabla^2 \boldsymbol{\psi} = \frac{1}{r}\frac{\partial \psi}{\partial r} - r\left(\boldsymbol{C}_m \times \nabla \rho\right)\hat{\boldsymbol{e}}_\theta + \rho r \omega_\theta. \tag{3.85}$$

We may also express this Poisson equation as

$$\nabla^2 \boldsymbol{\psi} = Q_0 + Q_1 \tag{3.86}$$

where

$$Q_0 = \frac{1}{r}\frac{\partial \psi}{\partial r} \tag{3.87}$$

The Q_0 term is a result of the axisymmetry of the problem. The remaining terms can be expanded into the transverse circulation gradient, the transverse work gradient, and the transverse loss gradient. For our purposes of initialization, we do not have any information a priori concerning the terms not a part of Q_0 so we set them to zero. Later,

after the non-linear solve, we may choose to update the streamlines and resolve; though at that point there are more direct methods of determining streamlines from the velocity field that may be more desirable to use.

3.4.2 Generation of an Elliptic Grid for Streamline Approximation

We are now ready to generate the solution grid, parametrically defined from our global coordinates through Poisson equations:[i]

$$\xi(z,r) \equiv \nabla^2 \xi = \xi_{zz} + \xi_{rr} = P \tag{3.88}$$

$$\eta(z,r) \equiv \nabla^2 \eta = \eta_{zz} + \eta_{rr} = Q. \tag{3.89}$$

where η and ξ are the coordinates of the rectangular region and z and r are the coordinates of physical space. We will set $Q = Q_0$ and therefore equation (3.89) is equivalent to equation (3.86) and thus $\eta \equiv \psi$. We then let η be the coordinate that is constant on the body boundaries. Thus lines of constant η correspond to physical streamlines as seen in figure 3.7. The ξ values have no physical interpretation, so we set $P = 0$ which allows ξ to be arbitrarily chosen as indicated by Thompson *et al.* For convenience, we will set ξ =constant along radial lines, also seen in figure 3.7.

[i] We change our notation style for partial derivatives here as it proves to be easier to read due to the shear number of derivatives in this section.

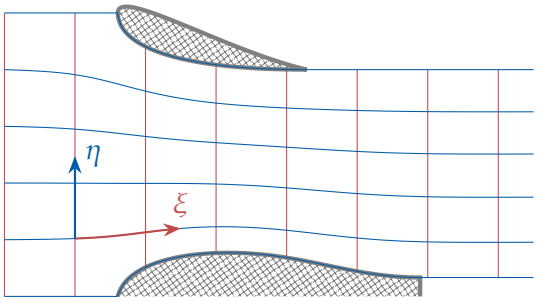

Figure 3.7: Elliptic grid coordinate system showing lines of constant η (blue) coinciding with streamlines, and lines of constant ξ (red) are constant relative to change in radius when the z-coordinates of the upper and lower boundaries are aligned.

In order to solve for the (z,r) coordinates associated with physical streamlines, we need to invert the dependent and independent variables in equations (3.88) and (3.89). In order to do so, we use the following derivative transformations:[16]

$$f_z = \frac{\frac{\partial(f,r)}{\partial(\xi,\eta)}}{\frac{\partial(z,r)}{\partial(\xi,\eta)}} = \frac{r_\eta f_\xi - r_\xi f_\eta}{z_\xi r_\eta - z_\eta r_\xi} \tag{3.90a}$$

$$f_r = \frac{\frac{\partial(z,f)}{\partial(\xi,\eta)}}{\frac{\partial(z,r)}{\partial(\xi,\eta)}} = \frac{-z_\eta f_\xi + z_\xi f_\eta}{z_\xi r_\eta - z_\eta r_\xi} \tag{3.90b}$$

16 Thompson *et al.*, "Automatic numerical generation of body-fitted curvilinear coordinate system for field containing any number of arbitrary two-dimensional bodies," 1974.

The details of the inversion are included in Appendix B. After the inversion, we are left with expressions for z and r with respect to ξ and η.

$$\alpha z_{\xi\xi} - 2\beta z_{\xi\eta} + \gamma z_{\eta\eta} = \frac{J}{r} z_\eta z_\xi \tag{3.91}$$

$$\alpha r_{\xi\xi} - 2\beta r_{\xi\eta} + \gamma r_{\eta\eta} = \frac{J}{r} z_\eta r_\xi \tag{3.92}$$

or equivalently in terms of α, β, γ only:

$$\begin{aligned} \alpha z_{\xi\xi} - 2\beta z_{\xi\eta} + \frac{\gamma}{r}\left(r z_\eta\right)_\eta - \frac{\beta}{r} r_\xi z_\eta = 0 \\ \alpha r_{\xi\xi} - 2\beta r_{\xi\eta} + \frac{\gamma}{r}\left(r r_\eta\right)_\eta - \frac{\beta}{r} r_\xi r_\eta = 0 \end{aligned} \tag{3.93}$$

where

$$\alpha = z_\eta^2 + r_\eta^2 \tag{3.94}$$

$$\beta = z_\xi z_\eta + r_\xi r_\eta \tag{3.95}$$

$$\gamma = z_\xi^2 + r_\xi^2 \tag{3.96}$$

$$J = z_\xi r_\eta - z_\eta r_\xi \tag{3.97}$$

If we set constant ξ and η values on each grid line, we can solve equation (3.93) for the desired z and r positions.

For boundary conditions, we will set fixed geometry (z, r positions) on solid walls and the rotor plane[j], and require that the velocity be aligned with streamlines at the outlet plane. The solid boundary and rotor plane geometry will be known from the user inputs. We can obtain expressions for the velocity in terms of z and r only[k] if we take the differential identities of the transformations

[j] This is a Dirichlet boundary condition.

[k] Therefore the outlet boundary condition is a Neumann type.

$$\begin{bmatrix} z_\xi & z_\eta \\ r_\xi & r_\eta \end{bmatrix} \begin{pmatrix} d\xi \\ d\eta \end{pmatrix} = \begin{pmatrix} dz \\ dr \end{pmatrix} \tag{3.98}$$

$$\begin{bmatrix} \xi_z & \xi_r \\ \eta_z & \eta_r \end{bmatrix} \begin{pmatrix} dz \\ dr \end{pmatrix} = \begin{pmatrix} d\xi \\ d\eta \end{pmatrix} \tag{3.99}$$

and invert one, say equation (3.98),

$$\begin{pmatrix} d\xi \\ d\eta \end{pmatrix} = \frac{1}{J} \begin{bmatrix} r_\eta & -z_\eta \\ -r_\xi & z_\xi \end{bmatrix} \begin{pmatrix} dz \\ dr \end{pmatrix} \tag{3.100}$$

then set them equal to each other

$$\begin{bmatrix} \xi_z & \xi_r \\ \eta_z & \eta_r \end{bmatrix} \begin{pmatrix} dz \\ dr \end{pmatrix} = \frac{1}{J} \begin{bmatrix} r_\eta & -z_\eta \\ -r_\xi & z_\xi \end{bmatrix} \begin{pmatrix} dz \\ dr \end{pmatrix} \tag{3.101}$$

we see that

$$\xi_z = \frac{r_\eta}{J} \tag{3.102}$$

$$\xi_r = \frac{-z_\eta}{J} \tag{3.103}$$

$$\eta_z = \frac{-r_\xi}{J} \tag{3.104}$$

$$\eta_r = \frac{z_\xi}{J}. \tag{3.105}$$

Thus the velocities can be computed from equation (3.82) as

$$C_z = \frac{1}{\rho r}\frac{d\psi}{dr} = \frac{\eta_r}{\rho r} = \frac{z_\xi}{\rho r J} \tag{3.106}$$

$$C_r = \frac{-1}{\rho r}\frac{d\psi}{dx} = \frac{-\eta_z}{\rho r} = \frac{r_\xi}{\rho r J}. \tag{3.107}$$

In practice, we set the outlet boundary condition as

$$\hat{\eta}_z C_z + \hat{\eta}_r C_r = 0. \tag{3.108}$$

where $\hat{\eta}_{(\cdot)}$ indicates a component of the η unit vector. In other words, we require that there be no component of velocity in the η direction.[l]

[l] Said another way, this condition simply requires that the grid be along a streamline at the outlet boundary.

3.4.3 Solution Approach

In the actual implementation, we initialize the grid to have radial lines with constant axial position as shown in figure 3.7. This is a by-product of repaneling the body geometries in such a way that we can ensure a constant number of panels between discrete locations in the wake[m] so that we can avoid any discontinuities if rotor position or body lengths are included as optimization design variables. Because the initial grid points lie on constant radial lines, and we choose to set the ξ values to align with the initial grid z coordinates, the derivatives of z with respect to η, as well as the second derivative of z with respect to ξ, go to zero, which allows us to simplify our residual expression such that only the radial positions of the grid points need be changed to approximate streamlines. Therefore, equation (3.93) becomes

[m] Such as rotor planes, body trailing edges, etc.

$$\alpha r_{\xi\xi} - 2\beta r_{\xi\eta} + \frac{\gamma}{r}\left(r r_\eta\right)_\eta - \frac{\beta}{r} r_\xi r_\eta = 0, \tag{3.109}$$

where

$$\alpha = r_\eta^2, \tag{3.110}$$

$$\beta = r_\xi r_\eta, \tag{3.111}$$

$$\gamma = 1.0 + r_\xi^2. \tag{3.112}$$

To solve, we initialize the grid based on simple conservation of mass, setting the radial positions at the rotor plane to coincide with blade element edges, and then apply a non-linear solver to converge the residual of equation (3.109).

3.4.4 Discretizing the Wake into Panels

The process of discretization into panels follows immediately from the solution of this elliptic grid. We already input discrete "grid" points and after the solver places them at their final locations, we simply take the lines between points along the streamlines to be panels. For each panel, we can compute the vortex strength distribution using equation (3.81). Note that even though we use linear vortex panels in the wake, just like on the bodies, we solve for the wake strengths directly from the rotor circulation and induced velocities rather than having to develop a linear system like we do for the bodies.

Chapter 4 References

10 Drela, M., Youngren, H., and Sanders, S., *Ducted Fan Design Code (DFDC)*, version 0.70, December 10, 2005.URL: https://web.mit.edu/drela/Public/web/dfdc/. cited on pp. 26, 40

16 Thompson, J. F., Thames, F. C., and Mastin, C., "Automatic numerical generation of body-fitted curvilinear coordinate system for field containing any number of arbitrary two-dimensional bodies," en, *Journal of Computational Physics*, vol. 15, no. 3, July 1974, pp. 299–319. DOI: 10.1016/0021-9991(74)90114-4 cited on pp. 56–58

Chapter 4

DuctAPE: A steady-state, axisymmetric ducted fan analysis code designed for gradient-based optimization

4.1 Coupling the Body, Rotor, and Rotor-Wake Aerodynamics

We have introduced the constituent models of which DuctAPE is comprised in Chapters 2 and 3. We now discuss how these individual models are coupled together to make DuctAPE. Coupling the body and rotor-wake aerodynamics is, for the most part, a straightforward process, with only a few particular concerns. Essentially, the coupling takes place through mutually induced velocities. Specifically, the duct bodies, rotor(s), and wake sheets, all induce velocities on themselves and each other. Accounting for these induced velocities is nearly the totality of the coupling methodology.

For the duct bodies, we subtract the induced velocities normal to the panels to the right hand side of the linear system, just as we do for the freestream velocities.[a] In addition, at the wake-body interfaces, or in other words, for the wake elements shed from the rotor hub and tip (assuming the rotor tip "touches" the duct wall), the wake panels lie directly on the boundary being solved by the linear system. This requires the use of the separation of singularity integration when applying the induced velocity of the wake panels onto the body panels on which they lie. In order ease the coupling of wake panels coincident with body surfaces, the geometry is defined from the outset to have the nodes and control points of the overlapping regions of wake and body panels to be exactly coincident. This way we can use exactly the same approach for the body self-induced velocity cases explained in Chapter 2, to compute the wake-on-body and body-on-wake induced velocities across the overlaps. In addition, since the wake panels lie on the boundary being solved, they will also induce a jump in tangential velocity across the boundary which must be accounted for the post-processing step to calculate the body surface velocity, pressure, and thereby thrust/drag. Since the rotor tip and hub wakes interact with the body surfaces, additional consideration is also required for considering the strengths to define along the wake elements inside the duct. In reality, this is a complex, viscous interaction that we cannot properly capture given the inviscid methodologies of DuctAPE. As an approximation, we take the approach used in DFDC and apply a linear interpolation from the body trailing edge, which gets the full

[a] These are included in the $\boldsymbol{V}_{\text{ext}}$ term throughout Chapter 2, and it is for this reason we use the 'ext' subscript rather than the more commonly see ∞ subscript used in other panel method derivations.

rotor wake strength at that point, to the intersection of the rotor plane and wall, which we set to zero just ahead of the rotor.

For the rotor(s) we simply add the induced axial and radial velocities from the bodies and wakes to the relative axial and radial velocities used in determining the inflow angles and magnitudes across the blades. Similarly for the wake, we combine all the induced velocities together to obtain the average meridional velocities required to compute the wake node strengths. As noted in Chapter 3, the wake sheets are informed from the rotor blade section circulation as well, this being the only non-induced velocity term used in coupling the various models together.

4.1.1 Solution Method Exploration and Comparison

During development, we explored several options for solvers that could be used to solve the coupled aerodynamic system. In this section, we show an exploration of two residual formulations and various solver options available in DuctAPE. We begin with with an overview of a DFDC-like residual and solution method, which is specialized for efficient solution of the ducted fan system, but does not allow for the use of external solvers. We continue with an overview of an alternate formulation and approach we have also implemented in DuctAPE that is compatible with external solvers. We then provide an overall comparison of the two approaches including some benchmarking for a variety of solver options.

DFDC-like Solve Approach

The DFDC-like solution approach implemented in DuctAPE solves a non-linear system for the rotor circulation and wake panel strengths using a controlled successive over-relaxation (CSOR) fixed-point solver, taking the rotor circulation, rotor source panel strengths, and wake panel strengths as state variables.

To initialize the states in the DFDC-like approach, we first set the rotor source panel strengths to zero. For the circulation, we perform a set number of iterations applying simple momentum theory to obtain the average axial induced velocity on the rotor, and use equation (3.15) to obtain the circulation strengths along the way. The final induced axial velocity, along with the freestream and circulation strengths are then used to initialize the wake panel strengths using equation (3.81). Note that the tangential induced velocity on the rotors is not included in this process, nor are the body-induced velocities.

The DFDC-like residual function formulation shown algorithmically in Algorithm 4.3 updates the states during the residual evaluation. This leads to efficient convergence, but also precludes the DFDC-like approach from being used with many external solvers as well as ImplicitAD.

In addition, we provide here the methodology for calculating the various relaxation parameters used in DFDC's CSOR method which we have also implemented in DuctAPE. To obtain the relaxation factors for the rotor blade circulation, we look at the difference in the current axisymmetrically smeared blade element circulation states, $B\boldsymbol{\Gamma}$, and the

Algorithm 4.1 DFDC-like Solution Method

Initialize body, rotor, and wake strengths
while unconverged **and** iterator < iteration limit **do**

- Solve the linear system for the body vortex strengths
- Calculate new estimates for the blade element circulation
- Select relaxation factors for each blade element circulation value.
- Update the blade element circulation values.
- Calculate new estimates for the wake vortex strengths
- Select relaxation factors for each wake node.
- Update the wake vortex strengths.
- Update the rotor source panel strengths
- Check for convergence.

end while
Post-process Solution

new estimation, $(B\boldsymbol{\Gamma})_{\text{est}}$, normalized by the current circulation state with the greatest magnitude for the given rotor, $(B\Gamma)_{\text{max}}$:

$$\hat{\boldsymbol{\delta}} = \frac{\boldsymbol{\delta}_{B\Gamma}}{(B\Gamma)_{\text{max}}}, \tag{4.1}$$

where

$$\boldsymbol{\delta}_{B\Gamma} = (B\boldsymbol{\Gamma})_{\text{est}} - B\boldsymbol{\Gamma}. \tag{4.2}$$

To avoid overly large values of $\hat{\boldsymbol{\delta}}$, $(B\Gamma)_{\text{max}}$ is required to have a magnitude greater than or equal to 0.1 with the sign being positive if the average $B\Gamma$ value along the blade is positive and negative if the average along the blade is negative:

$$(B\Gamma)_{\text{max}} = \begin{cases} \max(B\boldsymbol{\Gamma}, 0.1) & \text{if } \overline{B\boldsymbol{\Gamma}} > 0, \\ \min(B\boldsymbol{\Gamma}, -0.1) & \text{otherwise;} \end{cases} \tag{4.3}$$

where $\overline{B\boldsymbol{\Gamma}}$ is the average of $B\boldsymbol{\Gamma}$ for the given rotor. We then take the magnitude of the maximum normalized difference along a blade, $\hat{\delta}_{\text{max}}$, and set the initial relaxation factor for the whole blade, ω_r, to be

$$\omega_r = \begin{cases} \dfrac{0.2}{|\hat{\delta}|_{\text{max}}} & \text{if } \frac{\omega_{r_{\text{nom}}}}{\hat{\delta}_{\text{max}}} < -0.2, \\ \dfrac{0.4}{|\hat{\delta}|_{\text{max}}} & \text{if } \frac{\omega_{r_{\text{nom}}}}{\hat{\delta}_{\text{max}}} > 0.4, \\ \omega_{r_{\text{nom}}} & \text{otherwise;} \end{cases} \tag{4.4}$$

where the nominal relaxation factor value, $\omega_{r_{\text{nom}}} = 0.4$, and the various relaxation factors (here and those described below) may be set as desired by the user; though the defaults presented here are identical to the values hard-coded into DFDC. Also note that in DuctAPE, the calculation of $\hat{\boldsymbol{\delta}}$ is implemented so that if $\hat{\boldsymbol{\delta}}$ happened to be zero, it is instead set to a magnitude of 1 to avoid a division by zero.

We then apply an additional scaling factor to the individual blade element relaxation factors, $\boldsymbol{\omega}_{be}$, based on whether the current and previous iteration difference values along the blade ($\boldsymbol{\delta}_{B\Gamma}$ and $\boldsymbol{\delta}_{B\Gamma_{\text{prev}}}$, respectively) are in the same or opposite directions. If the current and previous differences for a given blade element are of different signs, meaning the solver has moved the estimated and previous values in opposite directions, we apply an additional scaling factor of 0.6 to the overall relaxation factor to obtain the relaxation factor for that blade element. If the current and previous differences are of the same sign (direction), then we apply an additional scaling factor of 0.5.

$$\omega_{be_i} = \begin{cases} 0.6\omega_r & \text{if } \text{sign}(\delta_{B\Gamma_{\text{prev}_i}}) \neq \text{sign}(\delta_{B\Gamma_i}), \\ 0.5\omega_r & \text{otherwise.} \end{cases} \tag{4.5}$$

The relaxation factor selection is very similar for the wake vortex strengths. For all wake panel nodes, the nominal relaxation factor is set to $\omega_{\gamma_{\text{nom}}} = 0.4$. If the difference between current and previous iteration's differences in estimated and previous strength ($\boldsymbol{\delta}_{\gamma_{\text{prev}}}$ and $\boldsymbol{\delta}_{\gamma}$, respectively) are of the same sign, we apply a scaling factor of 1.2, and if not, we apply a scaling factor of 0.6:

$$\omega_{\gamma_i} = \begin{cases} 0.6\omega_{\gamma_{\text{nom}}} & \text{if } \text{sign}(\delta_{\gamma_{\text{prev}_i}}) \neq \text{sign}(\delta_{\gamma_i}), \\ 1.2\omega_{\gamma_{\text{nom}}} & \text{otherwise.} \end{cases} \tag{4.6}$$

We choose the new values for circulation and vortex strength to be the previous values plus the relaxation factors multiplied by the differences between the new estimates and current states:

$$B\boldsymbol{\Gamma} \stackrel{+}{=} \boldsymbol{\omega}_{be}\boldsymbol{\delta}_{B\Gamma}, \tag{4.7}$$

$$\boldsymbol{\gamma}_{\theta} \stackrel{+}{=} \boldsymbol{\omega}_{\gamma}\boldsymbol{\delta}_{\gamma}. \tag{4.8}$$

The nominal DFDC-like, relative convergence criteria for the solver is assembled with a combination of the maximum differences used in the relaxation factor selection:

$$\begin{aligned} \text{converged if } &|\delta_{\gamma}|_{\max} < 2 \cdot 10^{-4} V_{\text{ref}}, \\ &\text{and } |\delta_{B\Gamma}|_{\max} < 10^{-3} |B\Gamma|_{\max}; \end{aligned} \tag{4.9}$$

where V_{ref} is a reference velocity set by the user. Though in DuctAPE, we often use (especially for optimization) an absolute convergence criteria:

$$\begin{aligned} &\text{converged if } |\delta_\gamma|_{\max} < f_{\delta_\gamma}, \\ &\qquad\qquad \text{and } |\delta_{B\Gamma}|_{\max} < f_{\delta_{B\Gamma}}; \end{aligned} \tag{4.10}$$

where we typically set $f_{\delta_\gamma} = f_{\delta_{B\Gamma}} = 1e-12$.

Additional Solve Approach in DuctAPE

We have implemented an alternate solution approach in DuctAPE that solves a non-linear system for the rotor induced axial and tangential velocities and the wake absolute velocities using a generalized residual compatible with external solvers.

To choose initial states for the non-linear solve, we start by solving the panel method for the isolated bodies (without any rotors) first. We then take the induced velocities from the body and apply them (along with the freestream velocity) to the blade elements within CCBlade, a blade element momentum theory (BEMT) formulation with guaranteed convergence [17]. From the BEMT solution, we obtain the rotor induced axial and tangential velocities. With the freestream velocity, body panel strengths, and initialized rotor states, we initialize the absolute velocities in the wake.

17 Ning, "Using blade element momentum methods with gradient-based design optimization," 2021.

A summary of our additional solution approach is shown algorithmically in Algorithm 4.2 with references to relevant equations and figures. The underlying purpose of this additional solve approach is to add greater flexibility in using DuctAPE with external solvers. As the DFDC-like approach updates the state variables inside the residual function call, it is somewhat difficult to use that formulation with external solvers. We found that our reformulated residual performed better with external solvers than simply altering the DFDC-like residual to not update the state variables internally.

Differences in Approaches

The respective residual functions are similar. Indeed, under the hood, the residual calculation process is more or less a re-ordering of the internals and the states of each approach are intermediate values of the other (as can be seen from Algorithms 4.2 and 4.3). The DFDC-like approach converges on the rotor circulation and wake strengths, and also includes the rotor source panel strengths as state variables. The alternate approach converges on the rotor induced velocities and the absolute wake velocities which slightly fewer states than the DFDC approach.

Both state initialization approaches apply some sort of momentum theory, and that is where the similarities end. The approach we take as default in DuctAPE utilizes the body-induced velocities from the rotor-off case, as well as fully converges the blade element induced axial and tangential velocities. In contrast, the DFDC-like approach ignores tangential induced velocity, looks only at the average (rather than local blade element) induced axial velocity, and does not require convergence of induced velocity, opting instead for a set number of iterations. Both approaches are reasonable and avoid any issues that could be present

Algorithm 4.2 Alternate Solution Method

Initialize induced rotor velocities, and absolute wake velocities.
while unconverged **and** iterator < iteration limit **do**

- Calculate the blade element inflow angles and magnitudes
- Look up the blade element local lift and drag.
- Calculate the blade circulation and rotor source panel strengths
- Estimate the tangential induced velocity on the rotor
- Calculate the wake vortex strengths from the current wake velocity states and rotor circulation
- Solve the linear system for the body vortex strengths
- Estimate the axial induced velocity on the rotor
- Calculate the axial and radial induced velocities on the wake
- Estimate the wake absolute meridional velocities
- Check for convergence.

end while
Post-process Solution

with a method that requires, but does not guarantee, convergence. In practice, however, the DFDC-like method ends up not being suitable for optimization settings as the implementation is susceptible to conditions leading to the square root of a negative number, which is not defined for real numbers. This is typically not an issue for manual analysis when the user is providing a reasonable design, but an optimizer is generally not constrained to explore only reasonable designs in the search for the optimum.

As mentioned, the solution methods for both approaches use the same underlying equations. The largest difference between them is that the CSOR solver is constructed in a vaguely Gauss-Seidel way in that in each iteration the rotor circulation strengths are updated before being used to update the wake panel strengths, which in turn are updated before being used to update the rotor source panel strengths. This leads to a highly efficient, but also specialized solver.

On the other hand, the additional method is formulated in such a way that nearly any external solver can be used to converge the residual, which will be showcased somewhat later in section 4.1.1. Therefore, despite lacking specialization for inherent efficiency, the additional approach allows the user to select among various solvers depending on the desired usage.

Benchmarking Solver Implementations

To compare the solve methods, we benchmarked various solvers against the CSOR solver. Included in our comparison are the following external solvers:

- Fixed-point Solvers
  - NLsolve's[18] Anderson accelerated fixed-point method.[19]
  - SpeedMapping.jl[b] which uses an alternating cyclic extrapolation algorithm.[20]
  - Fixedpoint.jl[c] which is a Nesterov accelerated fixed-point method.
- Quasi-Newton Solvers
  - The modified Powell Method[21] implemented in MINPACK's HYBRJ method,[d] accessed through the Julia wrapper package, MINPACK.jl[e] which wraps a C++ re-write of MINPACK.
- Newton Solvers
  - NLsolve's Newton method using automatic differentiation for the Jacobian calculation and the Moré-Thuente line search method[22] option available through the LineSearches Julia package.[f]
  - The Newton-Raphson method implemented in the SimpleNonlinearSolve.jl package.[g][23]

Other than those specifically noted in this list, all solvers were set to use their default settings and given absolute convergence tolerances of 1e-12.

To perform the benchmarks, we used the same geometry and operating points used in the verification case below. For each advance ratio, we used BenchmarkTools.jl,[h] a benchmarking package in the Julia language, to run 200 samples, then calculated the median computational time across all samples and all advance ratios. We allowed the fixed-point solvers an iteration limit of 1000, the quasi-Newton solvers an iteration limit of 100, and the Newton solvers an iteration limit of 25. These iteration limits were sufficiently large that all solvers were able to converged on every analysis. We also ran each advance ratio one additional time, saving the solve iteration counts and taking the mean number of iterations across the advance ratios in order to determine solver efficiency.

Table 4.1 includes comparisons of the median solve times and mean number of iterations across all advance ratios for each of the benchmarked solvers. From Table 4.1, we first see that the default DFDC-like CSOR solve approach with loose, relative tolerances was very fast and efficient. We should expect this as the default convergence criteria is between 1e-3 and 2e-4, depending on the residual value. In contrast, all other solvers were given an absolute convergence tolerance of 1e-12, including the CSOR solver with absolute convergence criteria. Therefore, for tight, absolute tolerances, an Anderson accelerated fixed-point solver may be considered in favor of the CSOR solver if speed is the absolute priority, though a much broader set of benchmarks would need to be run before making that a general recommendation. In addition, selecting non-default options for the various solvers may lead to increases in speed

18 Mogensen *et al.*, *JuliaNLSolvers/NLsolve.jl: v4.5.1*, 2020.

19 Walker *et al.*, "Anderson Acceleration for Fixed-Point Iterations," 2011.

[b] https://github.com/NicolasL-S/SpeedMapping.jl

20 Lepage-Saucier, *Alternating cyclic extrapolation methods for optimization algorithms*, 2021.

[c] https://github.com/francescoaleman no/FixedPoint.jl

21 D., "A hybrid method for nonlinear equations," 1970.

[d] https://www.netlib.org/minpack/

[e] https://github.com/sglyon/MINPAC K.jl

22 Moré *et al.*, "Line search algorithms with guaranteed sufficient decrease," 1994.

[f] https://github.com/JuliaNLSolvers/Li neSearches.jl

[g] https://github.com/SciML/SimpleN onlinearSolve.jl

23 Pal *et al.*, "NonlinearSolve. jl: High-Performance and Robust Solvers for Systems of Nonlinear Equations in Julia," 2024.

[h] https://github.com/JuliaCI/Benchma rkTools.jl

Table 4.1: Comparison of benchmarked solver method median times and mean iterations. blue indicates fixed-point solvers, red indicates quasi-Newton solvers, and green indicates Newton solvers. In all cases, except for CSOR Default, the solvers were given absolute convergence criteria of 1e-12. (Note that the SimpleNonlinearSolve.jl package does not have any iteration tracing functionality and so that information is missing from this table.)

Method	Median Time (seconds)	Mean Iterations
CSOR Default	0.0042	15.571
CSOR Absolute	0.0183	76.476
NLSolve's Anderson Acceleration	0.0097	36.429
SpeedMapping.jl	0.0300	139.333
FixedPoint.jl (Nesterov Acceleration)	0.1399	592.286
MINPACK's HYBRJ	3.0528	14.238
SimpleNonlinearSolve's Newton Raphson	10.7100	
NLSolve's Newton Method	22.0116	16.714

or efficiency, again requiring a broader set of benchmarks before general recommendations can be made.

Another important result to notice here is the cost of computing the Jacobian of the residual. Looking at the quasi- and full Newton methods, we see several orders of magnitude increase in time, despite the lower number of overall iterations. As expected, the Jacobian-based methods are more efficient in iterations, but the cost to compute the Jacobian is so high that it outweighs any inherent efficiency of the method.

4.1.2 Final Solve Approach

After substantial usage in analysis and optimization settings, we found that despite the potential speed increases of some of the external solve methods, the DFDC-like CSOR method was overall more robust across a wider range of inputs. We therefore took the best of both worlds, reformulating the DFDC-like solver to perform all state updates outside of the residual which kept the robustness of the CSOR solver, but also allowed us to implement the solve using ImplicitAD for efficient automatic differentiation through the solver in optimization settings. The final solution approach takes the following form, beginning with state initialization.

State Initialization

We have also modified the state initialization method somewhat in order to increase the robustness of DuctAPE relative to DFDC. To initialize the states in a robust manner, we first solve the panel method given

a user defined uniform freestream. We then run a fast blade element momentum theory (BEMT) solver with guaranteed convergence, namely CCBlade [17] using the uniform freestream and body induced velocities. From the BEMT solution, we set the rotor source panel strengths and compute the blade element circulation. We then initialize the wake strengths from the freestream and induced velocities and blade element circulations.

17 Ning, "Using blade element momentum methods with gradient-based design optimization," 2021.

Solver Method

The solve algorithm we use is a fixed-point iteration method using controlled successive over-relaxation outlined in Algorithm 4.3. The method we have selected for this work is similar to the approach taken in DFDC, but we have modified and reorganized most of the steps in order to allow for implementation using ImplicitAD. The most notable difference in architecture is that the DFDC implementation updates states inside the residual before estimating other states in a vaguely Gauss-Sidel manner. We have moved all of the state updates outside of the residual enabling the use of implicit automatic differentiation methods. Doing so leads to slightly longer convergence times for individual analyses, but ends up being faster overall in a gradient-based optimization setting by avoiding having to pass derivatives through every iteration of the solve.

Algorithm 4.3 Solution Method

Initialize body, rotor, and wake strengths
while unconverged **and** iterator < iteration limit **do**

- Solve the for the body vortex strengths ▹ *using equation* (2.13).
- Estimate the blade element circulation ▹ *using equation* (3.15).
- Estimate the wake vortex strengths ▹ *using equation* (3.81).
- Estimate the rotor source strengths ▹ *using equation* (3.18).
- Calculate relaxation factors for each each state variable.
- Update states according to relaxation factors.
- Check for convergence.

end while
Post-process Solution

Summary of Novelty

As DuctAPE is so heavily based and the methods comprising DFDC, a summary of the novel contributions related to DuctAPE may be helpful. There are three main aspects of novelty in DuctAPE relative to DFDC. The first contribution is the re-derivation of the theory underpinning DFDC to ensure compatibility with AD and gradient-based optimization, along with the many minor implementation details that realize AD and gradient-based optimization compatibility. As a side benefit, DuctAPE exposes nearly all of the internal options to the user, whereas many

of those options are hard-coded in the DFDC implementation. By exposing internal options to the user, DuctAPE not only becomes usable in gradient-based optimization (by allowing sufficiently tight convergence tolerances), but also allows the user to fine tune settings for their specific optimization application. The second contribution is the re-formulation and implementation modifications of the various solver residuals in DFDC. Our modifications allow the solvers to be implemented using an adjoint method which makes differentiating through the solvers much more efficient than using direct differentiation methods. Using adjoint methods for differentiation enables even more efficient optimization than already experienced by using gradient-based methods. As part of the modification of the solvers, we additionally implemented a more robust state initialization approach for the coupled aerodynamics solve, allowing DuctAPE a greater level of robustness in an optimization setting. The third main contribution is the addition of viscous drag models for the duct and center body which are required in order to not over-estimate the duct-induced thrust of the system as will be seen in section 4.2.2. In addition, this work contains the application of DuctAPE in gradient-based optimization studies (see **??**) including studies comparing and contrasting electric ducted fans and airborne wind energy dual-purpose rotors with applications to distributed electric vertical take-off and landing concepts. These optimization studies showcase that the above contributions are sufficient and effective in enabling the gradient based optimization of electric ducted fans and related technologies across a range of applications.

4.2 Verification and Validation

In this section we present verification and validation of DuctAPE, showing outputs compared to DFDC, as well as characterizing some of the limitations of DuctAPE through a comparison with experimental data.

4.2.1 Verification Against DFDC

As we have established, the methodology behind DuctAPE is based heavily on DFDC. Therefore, we present a set of comparisons between DuctAPE and DFDC. We compare with an example available in the DFDC source code using a single ducted rotor across a range of operating conditions, specifically across a range of advance ratios including a hover condition.

The geometry used is shown in figure 4.1. For this verification case, we used a rotor with tip radius of 0.15572 meters located 0.12 meters aft of the center body leading edge. The wake extended 0.8 times the length of the duct (roughly 0.25 meters) past the duct trailing edge. We used 10 blade elements associated with 11 wake sheets to model the rotor. We set the rotor rotation rate constant at 8000 revolutions per minute and adjusted the freestream velocity in order to sweep across advance ratios from 0.0 to 2.0 by increments of 0.1.

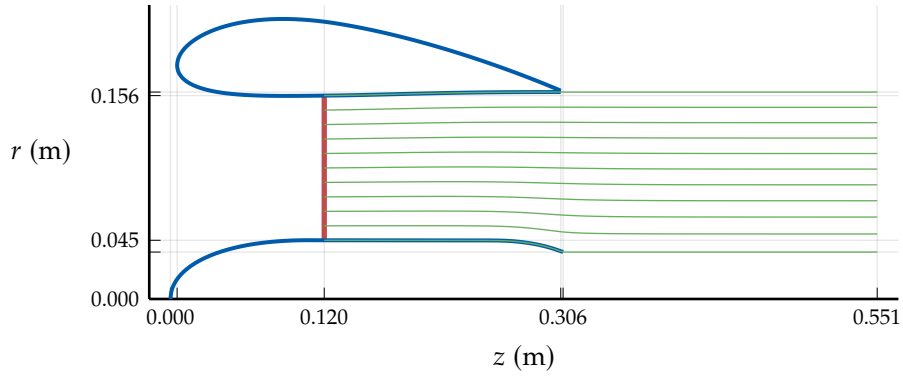

Figure 4.1: Single rotor verification case geometry generated in DuctAPE. Duct and center body geometry in blue, rotor lifting line location in red, and approximate wake streamlines in green, where markers indicate panel egdes.

As part of the myriad minor implementation variations enabling smooth gradients, we note here that DuctAPE differs from DFDC in the geometry re-paneling approach as part of the pre-processing of inputs. The DuctAPE geometry re-paneling approach aligns the duct, center body, and wake panels aft of the rotor and distributes them linearly. We align the panels so that there is a consistent number of panels between discrete locations (such as rotor positions and body trailing edges) in the geometry, thereby avoiding discontinuities that would be incompatible with a gradient-based optimizer. For example, the number of center body and duct panels ahead of and behind the rotor need to stay constant if the rotor position is selected as a design variable in an optimization. Without the number of panels ahead of and behind the rotor staying constant, there would be discontinuities as the rotor passed over panels along the solid bodies.

Scanning Table 4.2, we see that the differences between DFDC and DuctAPE are generally less than 1/2% for major output values for both a hover and a cruise case. Figure 4.2 shows comparisons of total thrust and power coefficients (figure 4.2(a)) and total efficiency (figure 4.2(b)), across the range of advance ratios, showing excellent matching across the entire range.

Table 4.2: Comparison of solver outputs for a cruise (J = 1.0) and hover (J = 0.0) case. Errors relative to DFDC.

Values at J=1.0	DFDC	DuctAPE	% Error
Rotor Thrust (N)	70.0	70.21	0.3
Body Thrust (N)	6.99	6.98	-0.1
Torque (N·m)	5.5	5.52	0.32
Rotor Efficiency	0.63	0.63	0.1
Total Efficiency	0.69	0.69	0.06

Values at J=0.0	DFDC	DuctAPE	% Error
Rotor Thrust (N)	91.8	91.83	0.03
Body Thrust (N)	106.45	107.02	0.53
Torque (N·m)	6.58	6.58	0.04

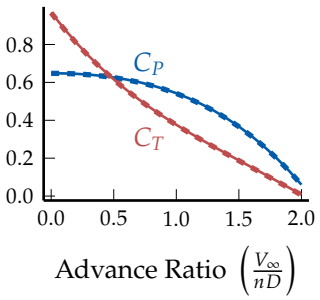

(a) Power (blue) and thrust (red) comparison.

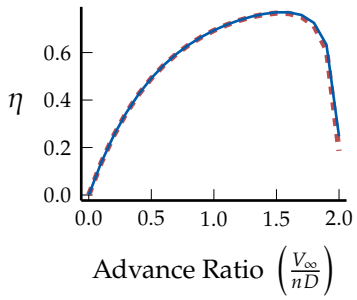

(b) Efficiency comparison.

Figure 4.2: Comparison of power and thrust coefficients and efficiency for DFDC (dashed) and the DuctAPE implementation (solid) across a range of advance ratios.

4.2.2 Validation with Experimental Data

Note that the data digitization and validation analysis in this subsection was performed by Nathan Lehnhof using the analysis and plotting code from Judd Mehr and the uncertainty analysis code of Ayden Bennett.

For validation, we compare DuctAPE outputs with data from a series of experiments performed by Hamilton Standard in the late 1960s [24]. The geometry for the experiments is shown in figure 4.3. Coordinates for the duct and center body, as well as the location of the rotor are provided in the Hamilton Standard report [24]. Details on the axial location of the center body leading edge are missing, so we have somewhat arbitrarily chosen the geometry shown here based on photographs in the report. We determined, however, that the location of the center body leading

edge has negligible impact on the results of the DuctAPE analysis for this case. We discretized the geometry and wake to allow both for numerical stability (avoiding too many panels), while also being sufficiently refined to keep relative changes in thrust and power coefficients below 1%. As with the verification case above, the specific geometry details and run scripts for this validation case—as well as digitized versions of the data tabulated in the Hamilton Standard report—are available in the companion repository to this work.

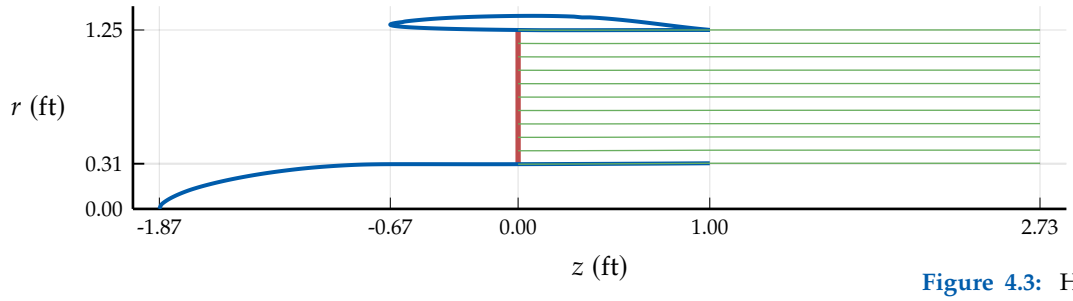

Figure 4.3: High-speed validation case geometry generated in DuctAPE. Duct and center body geometry in blue, rotor lifting line location in red, and approximate wake streamlines in green, where markers indicate panel edges.

We present here a comparison with one of the more complete test sets from the Hamilton Standard Report. For each test in this portion of the campaign, the ratio of the exit area to propeller area was 1.0. The tests were performed at Mach 0.2 with a narrow-tip, 3-blade propeller with a 3/4 radius twist angle of 43 degrees. Detailed rotor blade geometry information is also provided in the Hamilton Standard report for each of the cases, but some details are lacking in the definition of the blade section airfoil geometry. Based on the provided thickness and ideal lift coefficient distributions, we determined sets of NACA 16-series airfoils for which we ran XFOIL analyses. We then applied rotational (Du-Selig[25] and Eggers[26]) corrections to the resulting lift and drag polars which we also smoothed using B-Spline regressions to smooth out non-physical artifacts in the polars. Since the exact airfoil is unknown, we took minor liberties in applying additional pitch (within 2 degrees) to the rotor blades in an attempt to better match the rotor power.

We begin with rotor power and thrust coefficients compared in figure 4.4(a). We use faded markers for cases in which the rotor tip speed exceeded a critical Mach number of 0.7, and may therefore experience transonic effects not captured by XFOIL. We also include first-order uncertainty approximations based on measurement uncertainty and variable definitions provided in the Hamilton Standard report.[24] We see generally good matching of DuctAPE outputs compared with the experimental rotor data. Comparing with the average experimental values, we have an average absolute error of 3.7% for power coefficient and 1.5% error for thrust coefficient. Figure 4.4(b) shows comparisons of the total power and thrust coefficients (including duct forces). We note that general good matching remains. Specifically, the power coefficients are identical and the total thrust coefficient has an average absolute error of 2.1%. This indicates that our viscous drag model approximates the duct drag sufficiently well; which in this case balances almost completely

24 Rohrbach *et al.*, "Variable Geometry ducted Propeller Test Program: Final Report, Volume II," 1968.

with the duct-induced thrust. Thus very little difference is seen in the thrust between the rotor and total thrust.

These results are encouraging as we see DuctAPE able to capture the aerodynamics of ducted rotor systems well, even when stretching the underlying low Mach assumption of the methods. Though as noted, the low Mach assumption can only be stretched so far, as the accuracy is shown here to be dependent on the blade element polars provided to DuctAPE. If blade sections see transonic effects, it may still be possible for DuctAPE to model those cases accurately, provided that the polars are generated with a tool suitable for capturing transonic aerodynamics.

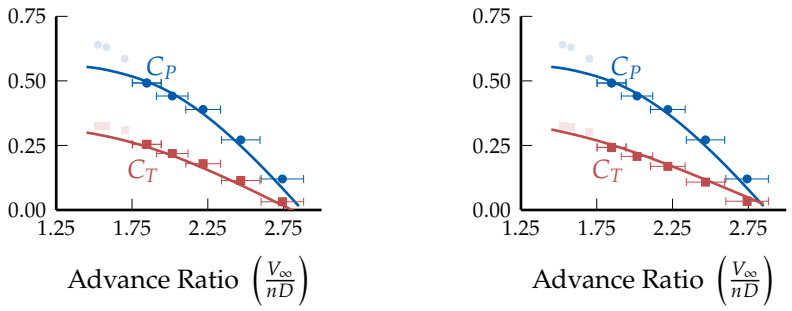

(a) Rotor power (blue) and thrust (red) comparison.

(b) Total (rotor + duct) power (blue) and thrust (red) comparison.

Figure 4.4: Comparison of rotor and rotor + duct power and thrust coefficients for DuctAPE (solid lines) and Hamilton Standard data (markers), where the cases with tip Mach number above 0.7 are faded.

The Hamilton-Standard experiments also included lower speed experiments with a bell-mouth inlet duct geometry. We found that DuctAPE struggled to match the experimental data in this case, notably due to large separation of the nacelle at higher speeds. This failure to model cases where viscous effects dominate highlights one of the limitations of DuctAPE—namely, the aerodynamic models are inviscid and therefore cannot model the coupled effects of separated flows, even when the integral boundary layer of **??** is applied. Therefore DuctAPE analyses become increasingly inaccurate the more severe separation becomes. This point will become important later in **??**.

Chapter 4 References

4 Fredholm, I., "Sur une classe d'équations fonctionnelles," *Acta Mathematica*, vol. 27, no. none, 1903, pp. 365–390. DOI: 10.1007/bf02421317 cited on p. 15

5 Lewis, R. I., *Vortex Element Methods for Fluid Dynamic Analysis of Engineering Systems*, ser. Cambridge engine technology series 1. Cambridge ; New York: Cambridge University Press, 1991. cited on pp. 17–19

6 Martensen, E., "Die Berechnung der Druckverteilung an dicken Gitterprofilen mit Hilfe von Fredholmschen Integralgleichungen zweiter Art," *Archive for Rational Mechanics and Analysis*, vol. 3, 1959, pp. 235–270. cited on pp. 17, 30

7 Courant, R. and Hilbert, D., *Methods of Mathematical Physics*. Interscience Publishers, 1962, vol. 2. cited on p. 17

11 Drela, M., "XFOIL: An Analysis and Design System for Low Reynolds Number Airfoils," *Low Reynolds Number Aerodynamics*, Mueller, T. J., Ed., Berlin, Heidelberg: Springer Berlin Heidelberg, 1989, pp. 1–12. cited on p. 28

16 Thompson, J. F., Thames, F. C., and Mastin, C., "Automatic numerical generation of body-fitted curvilinear coordinate system for field containing any number of arbitrary two-dimensional bodies," en, *Journal of Computational Physics*, vol. 15, no. 3, July 1974, pp. 299–319. DOI: 10.1016/0021-9991(74)90114-4 cited on pp. 56–58

17 Ning, A., "Using blade element momentum methods with gradient-based design optimization," en, *Structural and Multidisciplinary Optimization*, vol. 64, no. 2, August 2021, pp. 991–1014. DOI: 10.1007/s00158-021-02883-6 cited on pp. 66, 70

18 Mogensen, P. K., Carlsson, K., Villemot, S., Lyon, S., Gomez, M., Rackauckas, C., Holy, T., Widmann, D., Kelman, T., Karrasch, D., Levitt, A., Riseth, A. N., Lucibello, C., Kwon, C., Barton, D., TagBot, J., Baran, M., Lubin, M., Choudhury, S., Byrne, S., Christ, S., Arakaki, T., Bojesen, T. A., benneti, and Macedo, M. R. G., *JuliaNLSolvers/NLsolve.jl: V4.5.1*, version v4.5.1, December 2020URL: https://doi.org/10.5281/zenodo.4404703 cited on p. 68

19 Walker, H. F. and Ni, P., "Anderson Acceleration for Fixed-Point Iterations," *SIAM Journal on Numerical Analysis*, vol. 49, no. 4, 2011, pp. 1715–1735. DOI: 10.1137/10078356x cited on p. 68

20 Lepage-Saucier, N., *Alternating cyclic extrapolation methods for optimization algorithms*, 2021. cited on p. 68

21 D., P. M. J., "A hybrid method for nonlinear equations," *Numerical Methods for Nonlinear Algebraic Equations*, 1970, pp. 87–161. cited on p. 68

22 Moré, J. J. and Thuente, D. J., "Line search algorithms with guaranteed sufficient decrease," *ACM Trans. Math. Softw.*, vol. 20, no. 3, September 1994, pp. 286–307. DOI: 10.1145/192115.192132 cited on p. 68

23 Pal, A., Holtorf, F., Larsson, A., Loman, T., Schaefer, F., Qu, Q., Edelman, A., Rackauckas, C., *et al.*, "NonlinearSolve. jl: High-Performance and Robust Solvers for Systems of Nonlinear Equations in Julia," *ArXiv preprint arXiv:2403.16341*, 2024. cited on p. 68

24 Rohrbach, C., Fortmann, W., and Croxall, A., "Variable Geometry ducted Propeller Test Program: Final Report, Volume II," Report AD835090, United Aircraft Research Laboratories, May 1968. cited on pp. 73, 74

25 Du, Z. and Selig, M., "A 3-d stall-delay model for horizontal axis wind turbine performance prediction," *1998 ASME Wind Energy Symposium*. DOI: 10.2514/6.1998-21 cited on p. 74

26 Eggers, A., Chaney, K., and Digumarthi, R., "An Assessment of Approximate Modeling of Aerodynamic Loads on the UAE Rotor," January 2003. DOI: 10.1115/wind2003-868 cited on p. 74

References

1 Wengert, R. E., "A simple automatic derivative evaluation program," *Commun. ACM*, vol. 7, no. 8, August 1964, pp. 463–464. DOI: 10.1145/355586.364791 cited on p. 10

2 Martins, J. R. R. A. and Ning, A., *Engineering Design Optimization*. Cambridge University Press, January 2022. DOI: 10.1017/9781108980647 cited on p. 11

3 Ning, A. and McDonnell, T., *Automating Steady and Unsteady Adjoints: Efficiently Utilizing Implicit and Algorithmic Differentiation*, 2023.URL: https://arxiv.org/abs/2306.15243. cited on p. 11

4 Fredholm, I., "Sur une classe d'équations fonctionnelles," *Acta Mathematica*, vol. 27, no. none, 1903, pp. 365–390. DOI: 10.1007/bf02421317 cited on p. 15

5 Lewis, R. I., *Vortex Element Methods for Fluid Dynamic Analysis of Engineering Systems*, ser. Cambridge engine technology series 1. Cambridge ; New York: Cambridge University Press, 1991. cited on pp. 17–19

6 Martensen, E., "Die Berechnung der Druckverteilung an dicken Gitterprofilen mit Hilfe von Fredholmschen Integralgleichungen zweiter Art," *Archive for Rational Mechanics and Analysis*, vol. 3, 1959, pp. 235–270. cited on pp. 17, 30

7 Courant, R. and Hilbert, D., *Methods of Mathematical Physics*. Interscience Publishers, 1962, vol. 2. cited on p. 17

8 Ryall, D. L. and Collins, I. F., "Design and Test of a Series of Annular Aerofoils," Reports and Memoranda 3492, Ministry of Technology Aeronautical Research Council, March 1967. cited on pp. 18, 19

9 Katz, J. and Plotkin, A., *Low speed aerodynamics*, 2nd ed. Cambridge, UK: Cambridge University Press Cambridge, UK, 2001. cited on p. 21

10 Drela, M., Youngren, H., and Sanders, S., *Ducted Fan Design Code (DFDC)*, version 0.70, December 10, 2005.URL: https://web.mit.edu/drela/Public/web/dfdc/. cited on pp. 26, 40

11 Drela, M., "XFOIL: An Analysis and Design System for Low Reynolds Number Airfoils," *Low Reynolds Number Aerodynamics*, Mueller, T. J., Ed., Berlin, Heidelberg: Springer Berlin Heidelberg, 1989, pp. 1–12. cited on p. 28

12 Fidkowski, K. J., "A Coupled Inviscid–Viscous Airfoil Analysis Solver, Revisited," en, *AIAA Journal*, vol. 60, no. 5, May 2022, pp. 2961–2971. DOI: 10.2514/1.j061341 cited on p. 28

13 Head, M. R., "Entrainment in the Turbulent Boundary Layer," Reports and Memoranda 3152, Aeronautical Research Council, September 1958. cited on p. 36

14 Squire, H. B. and Young, A. D., "The Calculation of the Profile Drag of Aerofoils," Reports and Memoranda 1838, Aeronautical Research Committee, November 1937. cited on p. 37

15 Shevell, R. S., *Fundamentals of flight*. Englewood Cliffs, N.J.: Prentice-Hall, 1983, ch. xxiv, 405 pages : illustrations ; 25 cm. cited on p. 38

16 Thompson, J. F., Thames, F. C., and Mastin, C., "Automatic numerical generation of body-fitted curvilinear coordinate system for field containing any number of arbitrary two-dimensional bodies," en, *Journal of Computational Physics*, vol. 15, no. 3, July 1974, pp. 299–319. DOI: 10.1016/0021-9991(74)90114-4 cited on pp. 56–58

17 Ning, A., "Using blade element momentum methods with gradient-based design optimization," en, *Structural and Multidisciplinary Optimization*, vol. 64, no. 2, August 2021, pp. 991–1014. DOI: 10.1007/s00158-021-02883-6 cited on pp. 66, 70

18 Mogensen, P. K., Carlsson, K., Villemot, S., Lyon, S., Gomez, M., Rackauckas, C., Holy, T., Widmann, D., Kelman, T., Karrasch, D., Levitt, A., Riseth, A. N., Lucibello, C., Kwon, C., Barton, D., TagBot, J., Baran, M., Lubin, M., Choudhury, S., Byrne, S., Christ, S., Arakaki, T., Bojesen, T. A., benneti, and Macedo, M. R. G., *JuliaNLSolvers/NLsolve.jl: V4.5.1*, version v4.5.1, December 2020URL: https://doi.org/10.5281/zenodo.4404703 cited on p. 68

19 Walker, H. F. and Ni, P., "Anderson Acceleration for Fixed-Point Iterations," *SIAM Journal on Numerical Analysis*, vol. 49, no. 4, 2011, pp. 1715–1735. DOI: 10.1137/10078356x cited on p. 68

20 Lepage-Saucier, N., *Alternating cyclic extrapolation methods for optimization algorithms*, 2021. cited on p. 68

21 D., P. M. J., "A hybrid method for nonlinear equations," *Numerical Methods for Nonlinear Algebraic Equations*, 1970, pp. 87–161. cited on p. 68

22 Moré, J. J. and Thuente, D. J., "Line search algorithms with guaranteed sufficient decrease," *ACM Trans. Math. Softw.*, vol. 20, no. 3, September 1994, pp. 286–307. DOI: 10.1145/192115.192132 cited on p. 68

23 Pal, A., Holtorf, F., Larsson, A., Loman, T., Schaefer, F., Qu, Q., Edelman, A., Rackauckas, C., *et al.*, "NonlinearSolve. jl: High-Performance and Robust Solvers for Systems of Nonlinear Equations in Julia," *ArXiv preprint arXiv:2403.16341*, 2024. cited on p. 68

24 Rohrbach, C., Fortmann, W., and Croxall, A., "Variable Geometry ducted Propeller Test Program: Final Report, Volume II," Report AD835090, United Aircraft Research Laboratories, May 1968. cited on pp. 73, 74

25 Du, Z. and Selig, M., "A 3-d stall-delay model for horizontal axis wind turbine performance prediction," *1998 ASME Wind Energy Symposium*. DOI: 10.2514/6.1998-21 cited on p. 74

26 Eggers, A., Chaney, K., and Digumarthi, R., "An Assessment of Approximate Modeling of Aerodynamic Loads on the UAE Rotor," January 2003. DOI: 10.1115/wind2003-868 cited on p. 74

Detailed derivation of vortex ring induced velocity

Appendix **A**

This appendix covers the derivation of the induced velocity due to ring vortices, or in other words, axisymmetric free vortices. To derive an expression for the unit induced velocity due to a ring vortex, let us begin at equation (1.36), the solution to the Poisson equation for vorticity, to set up the form of the Biot-Savart law that will be convenient for our axisymmetric reference frame.

$$\psi = \frac{1}{4\pi}\int_{\mathcal{V}} \frac{\omega(q)}{|r|}\mathrm{d}^3 s. \tag{A.1}$$

We re-state some assumptions about the vortex ring that follow from our axisymmetric assumption:

Assumption A.1

The vortex ring is circular, such that the ring radius is constant.

$$r_o = constant$$

Assumption A.2

The vortex ring circulation is constant and in the tangential direction

$$\boldsymbol{\Gamma} = \gamma \hat{\boldsymbol{e}}_\theta$$

These assumptions formalize our axisymmetric assumption, and from them we can conclude that the vortex ring has no influence in the tangential direction, $\hat{\boldsymbol{e}}_\theta$.

In figure 2.2 we show again the coordinate system we will be using going forward. Without loss of generality, we will set the field point, $\boldsymbol{p}$, to be on the $\theta = 0$ plane.

Putting the solution to Poisson's equation in terms of our coordinate system gives

$$\psi = \frac{1}{4\pi}\int_{\mathcal{V}} \frac{\omega(x')}{|p - p'|} r_o \mathrm{d}\theta' \mathrm{d}r' \mathrm{d}z'. \tag{A.2}$$

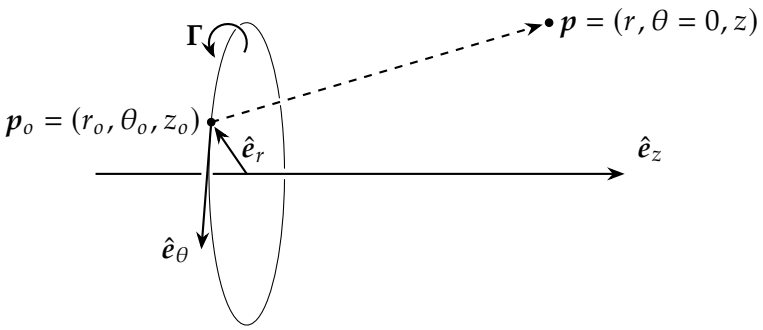

Figure A.1: Coordinate system for vortex ring induced velocity.

For a vortex ring, which is infinitesimally thin in the $\hat{\boldsymbol{e}}_r$ and $\hat{\boldsymbol{e}}_z$ directions, we can define the vorticity of the ring to be

$$\boldsymbol{\omega}(\boldsymbol{p}) = \gamma\delta(z - z_o)\delta(r - r_o)\hat{\boldsymbol{e}}_\theta. \tag{A.3}$$

where δ is the Dirac delta function. Plugging this expression in for vorticity, gives

$$\begin{aligned} \boldsymbol{\psi} &= \frac{1}{4\pi}\int_{\mathcal{V}} \frac{\gamma\delta(z - z_o)\delta(r - r_o)\hat{\boldsymbol{e}}_\theta(\theta')}{|\boldsymbol{p} - \boldsymbol{p}'|} r_o \mathrm{d}\theta'\mathrm{d}r'\mathrm{d}z' \\ \boldsymbol{\psi} &= \frac{1}{4\pi}\int_{-\pi}^{\pi} \frac{\gamma\hat{\boldsymbol{e}}_\theta(\theta')}{|\boldsymbol{p} - \boldsymbol{p}'|} r_o \mathrm{d}\theta', \end{aligned} \tag{A.4}$$

which we can simplify by taking the constants out of the integral:

$$\boldsymbol{\psi} = \frac{\gamma r_o}{4\pi}\int_{-\pi}^{\pi} \frac{\hat{\boldsymbol{e}}_\theta(\theta')}{|\boldsymbol{p} - \boldsymbol{p}'|}\mathrm{d}\theta'. \tag{A.5}$$

Next, let us tackle the denominator of the integrand, which is the Euclidean distance between a point on the vortex ring and a point we have chosen to be on the $\theta = 0$ plane. We apply the distance formula, for which we need to find the individual differences in each coordinate position. To obtain the Euclidean distance, it may be easier to momentarily think in terms of Cartesian coordinates, keeping the z-direction the same. Thus the length in the z-direction is simply the difference in the z-coordinates, $z - z_o$. To get the x and y distances, we require slightly more consideration. If we let the y-direction be normal to the $x - z$ plane (the $\theta = 0$ plane) on which the field point is defined, then we let the y component of the field point be $y = 0$, which means the distance in the y-direction is simply the position of the point on the ring, y_o. At a given θ_o, the distance in the y-direction will be $y_o = r_o \sin\theta_o$; θ being right hand positive taken about the z-axis. In the x-direction, we see that at the field point, the x-position is simply r, since the point lies on the $x - z$ plane. For the point on the vortex ring, we see that similar to the y-direction, the x-position is $x_o = r_o \cos\theta_o$. Before putting everything together, let us apply a normalization that will prove to be convenient in our notation later. We will normalize the positions of the points by the vortex ring

radius. We do this by multiplying by $r_o/r_o = 1$ giving the points in Cartesian coordinates as

$$\boldsymbol{p} = r_o \left[\frac{z}{r_o}\hat{\boldsymbol{e}}_z,\ 0\hat{\boldsymbol{e}}_y,\ \frac{r}{r_o}\hat{\boldsymbol{e}}_x \right] \tag{A.6}$$

$$\boldsymbol{p}_o = r_o \left[\frac{z_o}{r_o}\hat{\boldsymbol{e}}_z,\ \sin\theta_o\hat{\boldsymbol{e}}_y,\ \cos\theta_o\hat{\boldsymbol{e}}_x \right] \tag{A.7}$$

Putting all of these together we have

$$|\boldsymbol{p} - \boldsymbol{p}_o| = r_o \left[\left(\frac{z - z_o}{r_o} \right)^2 + (\sin\theta_o)^2 + \left(\frac{r}{r_o} - \cos\theta_o \right)^2 \right]^{1/2}. \tag{A.8}$$

To help clean up the notation, we will introduce the following normalized variables.

$$\xi = \frac{z - z_o}{r_o} \tag{A.9}$$

$$\rho = \frac{r}{r_o}. \tag{A.10}$$

In addition, we can simplify the radicand of our Euclidean distance expression by expanding the last term and applying the trigonometric identity $\sin^2\theta + \cos^2\theta = 1$:

$$\begin{aligned} &\xi^2 + \sin^2\theta_o + \left(\rho - \cos\theta_o\right)^2 \\ &\xi^2 + \sin^2\theta_o + \rho^2 + \cos^2\theta_o - 2\rho\cos\theta_o \\ &\xi^2 + \underbrace{\left(\sin^2\theta_o + \cos^2\theta_o\right)}_{1} + \rho^2 - 2\rho\cos\theta_o \quad \text{(trig identity)} \\ &\xi^2 + \rho^2 + 1 - 2\rho\cos\theta_o \end{aligned} \tag{A.11}$$

With this simplified radicand, equation (A.8) becomes

$$|\boldsymbol{p} - \boldsymbol{p}_o| = r_o \left[\xi^2 + \rho^2 + 1 - 2\rho\cos\theta_o \right]^{1/2}, \tag{A.12}$$

which if we plug back in to our full expression for $\boldsymbol{\psi}$ (equation (A.5)) we have

$$\boldsymbol{\psi} = \frac{\gamma}{4\pi} \int_{-\pi}^{\pi} \frac{\hat{\boldsymbol{e}}_\theta(\theta')}{\left[\xi^2 + \rho^2 + 1 - 2\rho\cos\theta' \right]^{1/2}} \mathrm{d}\theta'. \tag{A.13}$$

We now will apply one more advantage of our axisymmetric assumption, which is that both the potential and velocity fields are axisymmetric. Because the field point is set, without loss of generality, on the $x - z$ (or $\theta = 0$) plane, we can take the radially induced velocity at the field point to be only in the x-direction, and the tangential component to be only

in the y-direction. Therefore we make take $\hat{\boldsymbol{e}}_\theta$ to be its y component: $\cos\theta\hat{\boldsymbol{e}}_y$. Likewise, $\hat{\boldsymbol{e}}_r$ can be replaced with its x-component: $\cos\theta\hat{\boldsymbol{e}}_x$. Conveniently, this allows us to perform one integration over θ as the single variable rather than having to perform a double integration of x and y thereby reducing our expression for $\boldsymbol{\psi}$ to only the tangential component, ψ_θ. Therefore we replace the $\hat{\boldsymbol{e}}_\theta(\theta')$ in the numerator of equation (A.13) with $\cos(\theta')$ to arrive at the expression for the tangential component of $\boldsymbol{\psi}$,

$$\psi_\theta(\boldsymbol{x},\boldsymbol{x}_o) = \frac{\gamma}{4\pi}\int_{-\pi}^{\pi} \frac{\cos(\theta')}{\left[\xi^2+\rho^2+1-2\rho\cos\theta'\right]^{1/2}}\mathrm{d}\theta'. \tag{A.14}$$

We are now left with a simplified expression for ψ, but that is still a relatively difficult integral to implement numerically, and perhaps more difficult to approach analytically. To make our lives easier, we are going to get our expression in terms of elliptic integrals, which are far simpler to implement numerically. We can make this transformation by first making a slight change to the bounds of integration, taking advantage of the fact that the integrand is an even function.

$$\psi_\theta(\boldsymbol{x},\boldsymbol{x}_o) = \frac{\gamma}{2\pi}\int_{0}^{\pi} \frac{\cos(\theta')}{\left[\xi^2+\rho^2+1-2\rho\cos\theta'\right]^{1/2}}\mathrm{d}\theta'. \tag{A.15}$$

Next, we will apply the substitution

$$\theta' = 2\varphi \tag{A.16}$$
$$\mathrm{d}\theta' = 2\mathrm{d}\varphi, \tag{A.17}$$

noting the bounds of integration need to be divided by 2 as well, and changed to $[0,\ \pi/2]$. Applying equation (A.16) and the trigonometric identity $\cos(2\varphi) = 2\cos^2(\varphi) - 1$ gives

$$\begin{aligned}\psi_\theta(\boldsymbol{x},\boldsymbol{x}_o) &= \frac{\gamma}{\pi}\int_{0}^{\frac{\pi}{2}} \frac{2\cos^2(\varphi)-1}{\left[\xi^2+\rho^2+1-4\rho\cos^2\varphi+2\rho\right]^{1/2}}\mathrm{d}\varphi \\ &= \frac{\gamma}{\pi}\int_{0}^{\frac{\pi}{2}} \frac{2\cos^2(\varphi)-1}{\left[\xi^2+(\rho+1)^2-4\rho\cos^2\varphi\right]^{1/2}}\mathrm{d}\varphi.\end{aligned} \tag{A.18}$$

We will immediately apply another substitution

$$\cos\varphi = t \tag{A.19}$$

$$\begin{aligned} \mathrm{d}\varphi &= \frac{\mathrm{d}t}{-\sin\varphi} \\ &= -\frac{\mathrm{d}t}{\sqrt{1-\cos^2\varphi}} \\ &= -\frac{\mathrm{d}t}{\sqrt{1-t^2}}, \end{aligned} \tag{A.20}$$

where $\cos(\pi/2) = 0$ and $\cos(0) = 1$ so we will flip the bounds and cancel out the negative in equation (A.20):

$$\psi_\theta(\boldsymbol{p}, \boldsymbol{p}_o) = \frac{\gamma}{\pi}\int_0^1 \frac{2t^2-1}{\left[\xi^2+(\rho+1)^2-4\rho t^2\right]^{1/2}\left[1-t^2\right]^{1/2}}\mathrm{d}t. \tag{A.21}$$

Next we multiply by the top and bottom of the integrand by $\left[(\rho+1)^2+\xi^2\right]^{-1/2}$, noting that this term is constant relative to the integral and can therefore be brought outside.

$$\psi_\theta(\boldsymbol{p}, \boldsymbol{p}_o) = \frac{\gamma}{\pi\left[(\rho+1)^2+\xi^2\right]^{1/2}}\int_0^1 \frac{2t^2-1}{\left[1-\frac{4\rho t^2}{(\rho+1)^2+\xi^2}\right]^{1/2}\left[1-t^2\right]^{1/2}}\mathrm{d}t. \tag{A.22}$$

we now let

$$m = \frac{4\rho}{(\rho+1)^2+\xi^2} \tag{A.23}$$

which cleans things up to be

$$\psi_\theta(\boldsymbol{p}, \boldsymbol{p}_o) = \frac{\gamma}{\pi\left[(\rho+1)^2+\xi^2\right]^{1/2}}\int_0^1 \frac{2t^2-1}{\left[1-mt^2\right]^{1/2}\left[1-t^2\right]^{1/2}}\mathrm{d}t. \tag{A.24}$$

Our integrand is now almost matching to elliptic integrals. We just need to apply some algebraic manipulations to the numerator to match elliptic integral expressions of the form

$$\mathcal{K}(m) = \int_0^1 \frac{\mathrm{d}t}{\sqrt{(1-t^2)(1-mt^2)}} \tag{A.25}$$

$$\mathcal{E}(m) = \int_0^1 \frac{\sqrt{1-mt^2}}{\sqrt{(1-t^2)}}\mathrm{d}t \tag{A.26}$$

where $\mathcal{K}(m)$ and $\mathcal{E}(m)$ are elliptic integrals of the first and second kind, respectively. Making the required algebraic manipulations yields

$$\psi_\theta(\boldsymbol{p}, \boldsymbol{p}_o) = -\frac{\gamma}{\pi\left[(\rho+1)^2+\xi^2\right]^{1/2}} \int_0^1 \frac{1-\frac{2}{m}+\frac{2}{m}(1-mt^2)}{\left[1-mt^2\right]^{1/2}\left[1-t^2\right]^{1/2}} \mathrm{d}t. \quad \text{(A.27)}$$

Splitting the integrand up we have

$$\psi_\theta(\boldsymbol{p}, \boldsymbol{p}_o) = -\frac{\gamma}{\pi\left[(\rho+1)^2+\xi^2\right]^{1/2}} \left[\left(1-\frac{2}{m}\right) \int_0^1 \frac{\mathrm{d}t}{\left[1-mt^2\right]^{1/2}\left[1-t^2\right]^{1/2}} + \frac{2}{m} \int_0^1 \frac{\left[1-mt^2\right]^{1/2}}{\left[1-t^2\right]^{1/2}} \mathrm{d}t \right]. \quad \text{(A.28)}$$

Each of the integrals is now in the form of an elliptic integral. Making the substitution for elliptic integrals gives

$$\psi_\theta(\boldsymbol{p}, \boldsymbol{p}_o) = -\frac{\gamma}{\pi\left[(\rho+1)^2+\xi^2\right]^{1/2}} \left[\frac{2}{m}\mathcal{E}(m) - \left(\frac{2}{m}-1\right)\mathcal{K}(m) \right]. \quad \text{(A.29)}$$

A.1 General Form of Induced Velocities

The next step is to obtain the induced velocity from the vector potential, $\psi_\theta(\boldsymbol{p}, \boldsymbol{p}_o)$. Remember from our basic derivation of the Biot-Savart law that we need to take the curl of the vector potential to get the velocity induced by a vortex filament. In cylindrical coordinates, $\boldsymbol{V} = \nabla \times \boldsymbol{\psi}$ expands to:

$$\begin{aligned} \boldsymbol{V} = &\left(\frac{1}{r}\frac{\partial \psi_z}{\partial \theta} - \frac{\partial \psi_\theta}{\partial z}\right)\hat{\boldsymbol{e}}_r \\ &+ \left(\frac{\partial \psi_r}{\partial z} - \frac{\partial \psi_z}{\partial r}\right)\hat{\boldsymbol{e}}_\theta \\ &+ \frac{1}{r}\left(\frac{\partial (r\psi_\theta)}{\partial r} - \frac{\psi_r}{\theta}\right)\hat{\boldsymbol{e}}_z. \end{aligned} \quad \text{(A.30)}$$

Since our axisymmetric assumption allowed us to eliminate all but the tangential component of the vector potential, all but the ψ_θ components in equation (A.30) disappear, leaving us with the following induced velocities in the r- and z-directions.

$$v_z = \frac{1}{r}\frac{\partial (r\psi_\theta)}{\partial r}, \quad \text{(A.31a)}$$

$$v_r = -\frac{\partial \psi_\theta}{\partial z}. \quad \text{(A.31b)}$$

Now we need to take these partial derivatives to arrive at our final expressions of induced velocity. Because our current vector potential expressions are in terms of m and normalized values, we will require the application of the chain rule. Therefore it will be important to have the expressions for the various partial derivatives along the way. The derivative of the elliptic integral of the first kind with respect to m is

$$\frac{\partial \mathcal{K}(m)}{\partial m} = \frac{\mathcal{E}(m)}{2m(1-m)} - \frac{\mathcal{K}(m)}{2m}. \tag{A.32}$$

The derivative of the elliptic integral of the second kind is

$$\frac{\partial \mathcal{E}(m)}{\partial m} = \frac{\mathcal{E}(m)}{2m} - \frac{\mathcal{K}(m)}{2m}. \tag{A.33}$$

The partial of m with respect to ξ is

$$\frac{\partial m}{\partial \xi} = -\frac{8\rho\xi}{\left((\rho+1)^2+\xi^2\right)^2}. \tag{A.34}$$

The partial of ξ with respect to z is

$$\frac{\partial \xi}{\partial z} = \frac{1}{r_o}. \tag{A.35}$$

The partial of m with respect to ρ is

$$\frac{\partial m}{\partial \rho} = \frac{4\left(-\rho^2+\xi^2+1\right)}{\left((\rho+1)^2+\xi^2\right)^2}. \tag{A.36}$$

The partial of ρ with respect to r is

$$\frac{\partial \rho}{\partial r} = \frac{1}{r_o}. \tag{A.37}$$

Though simple to write symbolically, the overall derivatives become very cumbersome. To keep things manageable, let us separate out the expression for ψ_θ into the constant (C), numerator ($\mathcal{N}$), and denominator ($\mathcal{D}$) portions, respectively:

$$\begin{aligned} C &= -\frac{\Gamma}{\pi} \\ \mathcal{N} &= \frac{2}{m}\mathcal{E}(m) - \frac{2}{m}\mathcal{K}(m) + \mathcal{K}(m) \\ \mathcal{D} &= \left[(\rho+1)^2+\xi^2\right]^{1/2}. \end{aligned} \tag{A.38}$$

The partial of the numerator with respect to z is

$$\begin{aligned} \frac{\partial \mathcal{N}}{\partial z} = -\frac{\partial m}{\partial \xi}\frac{\partial \xi}{\partial z}\Bigg[&\frac{\mathcal{K}(m)+\mathcal{E}(m)}{m^2} \\ &- \frac{3\mathcal{K}(m)(m-1)+\mathcal{E}(m)}{m^2(m-1)} \\ &+ \frac{\mathcal{K}(m)(m-1)+\mathcal{E}(m)}{2m(m-1)}\Bigg]. \end{aligned} \tag{A.39}$$

The partial of the denominator with respect to z is

$$\frac{\partial \mathcal{D}}{\partial z} = \frac{\partial \xi}{\partial z}\frac{\xi}{\mathcal{D}} = \frac{\xi}{r_o \mathcal{D}}. \tag{A.40}$$

The partial of the numerator with respect to r is

$$\begin{aligned}\frac{\partial \mathcal{N}}{\partial r} =& \frac{\partial m}{\partial \rho}\frac{\partial \rho}{\partial r}\left[-\frac{3\mathcal{E}(m) + (m-5)\mathcal{K}(m)}{2m(m-1)} \right. \\ &\left. + \frac{2\mathcal{E}(m) - 2\mathcal{K}(m)}{m^2(m-1)} \right]\end{aligned} \tag{A.41}$$

The partial of the denominator with respect to r is

$$\frac{\partial \mathcal{D}}{\partial r} = \frac{\partial \rho}{\partial r}\frac{\rho+1}{\mathcal{D}} = \frac{\rho+1}{r_o \mathcal{D}}. \tag{A.42}$$

Putting things together for v_r with the quotient rule gives

$$v_r = -\frac{\partial \psi_\theta}{\partial z} = -C\frac{\frac{\partial \mathcal{N}}{\partial z}\mathcal{D} - \mathcal{N}\frac{\partial \mathcal{D}}{\partial z}}{\mathcal{D}^2}. \tag{A.43}$$

Putting things together for v_z we start with the quotient rule, then apply the product rule to arrive at

$$\begin{aligned} v_z =& \frac{1}{r}\frac{\partial (r\psi_\theta)}{\partial r} \\ =& \frac{C}{r}\frac{\frac{\partial (\mathcal{N}r)}{\partial r}\mathcal{D} - (\mathcal{N}r)\frac{\partial \mathcal{D}}{\partial r}}{\mathcal{D}^2} \\ =& C\frac{\left(\mathcal{N} + r\frac{\partial \mathcal{N}}{\partial r}\right)\mathcal{D} - (\mathcal{N}r)\frac{\partial \mathcal{D}}{\partial r}}{r\mathcal{D}^2}. \end{aligned} \tag{A.44}$$

A.2 Radially Induced Velocity Component

Now let's see what we can do about simplifying these expressions. We'll start with equation (A.43). To get started, we'll split up the fraction, and expand out the partial of $\mathcal{D}$,

$$v_r = -C\left[\underbrace{\frac{\frac{\partial \mathcal{N}}{\partial z}}{\mathcal{D}}}_{\text{Term 1}} - \underbrace{\frac{\mathcal{N}\xi}{r_o D^3}}_{\text{Term 2}}\right] \tag{A.45}$$

We are going to look at each term in the brackets of equation (A.45) separately first, then bring them together. We'll start with Term 2. Expanding gives

$$\frac{N\xi}{r_o D^3} = \frac{\xi}{r_o D^3}\left[\frac{2}{m}\mathcal{E}(m) + \left(1 - \frac{2}{m}\right)\mathcal{K}(m)\right] \tag{A.46}$$

Let us address the m's in the denominators by realizing that a comparison of equations (A.23) and (A.38) indicates that

$$\mathcal{D}^2 = \frac{4\rho}{m}. \tag{A.47}$$

Making this replacement in equation (A.46) gives

$$\begin{aligned}\frac{N\xi}{r_o D^3} &= \frac{\xi \cancel{m}}{4\rho r_o D}\left[\frac{2}{\cancel{m}}\mathcal{E}(m) + \left(\cancel{1}\frac{\cancel{m}}{} - \frac{2}{\cancel{m}}\right)\mathcal{K}(m)\right] \\ &= \frac{\xi/\rho}{4r_o D}\left[2\mathcal{E}(m) + (m-2)\,\mathcal{K}(m)\right]\end{aligned} \tag{A.48}$$

Now let's look at Term 1 from equation (A.43). Expanding out gives

$$\begin{aligned}\frac{\frac{\partial \mathcal{N}}{\partial z}}{\mathcal{D}} =& \frac{8\rho\xi}{r_o D\left((\rho+1)^2+\xi^2\right)^2}\left[\frac{\mathcal{K}(m)+\mathcal{E}(m)}{m^2}\right. \\ &- \frac{3\mathcal{K}(m)(m-1)+\mathcal{E}(m)}{m^2(m-1)} \\ &\left.+ \frac{\mathcal{K}(m)(m-1)+\mathcal{E}(m)}{2m(m-1)}\right].\end{aligned} \tag{A.49}$$

We can see right away that part of the fraction outside of the brackets closely resembles the parameter m^2, all we're missing is 2ρ in the numerator, so we'll multiply and divide by 2ρ.

$$\begin{aligned}\frac{\frac{\partial \mathcal{N}}{\partial z}}{\mathcal{D}} =& \frac{(2\rho)8\rho\xi}{2\rho r_o D\left((\rho+1)^2+\xi^2\right)^2}\left[\frac{\mathcal{K}(m)+\mathcal{E}(m)}{m^2}\right. \\ &- \frac{3\mathcal{K}(m)(m-1)+\mathcal{E}(m)}{m^2(m-1)} \\ &\left.+ \frac{\mathcal{K}(m)(m-1)+\mathcal{E}(m)}{2m(m-1)}\right].\end{aligned} \tag{A.50}$$

which allows us to remove some of the m^2 denominators inside the brackets

$$\begin{aligned}\frac{\frac{\partial \mathcal{N}}{\partial z}}{\mathcal{D}} =& \frac{\xi \cancel{m^2}}{2\rho r_o D}\left[\frac{\mathcal{K}(m)+\mathcal{E}(m)}{\cancel{m^2}}\right. \\ &- \frac{3\mathcal{K}(m)(m-1)+\mathcal{E}(m)}{\cancel{m^2}(m-1)} \\ &\left.+ \frac{m(\mathcal{K}(m)(m-1)+\mathcal{E}(m))}{2\cancel{m}(m-1)}\right].\end{aligned} \tag{A.51}$$

$$\begin{aligned}\frac{\frac{\partial \mathcal{N}}{\partial z}}{\mathcal{D}} =& \frac{\xi/\rho}{2r_o D}\Bigg[\mathcal{K}(m) + \mathcal{E}(m) \\ &- \frac{3\mathcal{K}(m)(m-1) + \mathcal{E}(m)}{m-1} \\ &+ \frac{m(\mathcal{K}(m)(m-1) + \mathcal{E}(m))}{2(m-1)}\Bigg].\end{aligned} \tag{A.52}$$

Splitting up the fractions inside the brackets will let us simplify further.

$$\begin{aligned}\frac{\frac{\partial \mathcal{N}}{\partial z}}{\mathcal{D}} =& \frac{\xi/\rho}{2r_o D}\Bigg[\mathcal{K}(m) + \mathcal{E}(m) \\ &- \frac{3\mathcal{K}(m)\cancel{(m-1)}}{\cancel{m-1}} - \frac{\mathcal{E}(m)}{m-1} \\ &+ \frac{m\mathcal{K}(m)\cancel{(m-1)}}{2\cancel{(m-1)}} + \frac{m\mathcal{E}(m)}{2(m-1)}\Bigg].\end{aligned} \tag{A.53}$$

$$\begin{aligned}\frac{\frac{\partial \mathcal{N}}{\partial z}}{\mathcal{D}} =& \frac{\xi/\rho}{2r_o D}\Bigg[\mathcal{K}(m) + \mathcal{E}(m) - 3\mathcal{K}(m) - \frac{1}{m-1}\mathcal{E}(m) \\ &+ \frac{m}{2}\mathcal{K}(m) + \frac{m}{2(m-1)}\mathcal{E}(m)\Bigg].\end{aligned} \tag{A.54}$$

Grouping like terms

$$\begin{aligned}\frac{\frac{\partial \mathcal{N}}{\partial z}}{\mathcal{D}} =& \frac{\xi/\rho}{2r_o D}\Bigg[\left(1 - \frac{1}{m-1} + \frac{m}{2(m-1)}\right)\mathcal{E}(m) \\ &+ \left(\frac{m}{2} - 2\right)\mathcal{K}(m)\Bigg].\end{aligned} \tag{A.55}$$

Simplifying the gathered terms for $\mathcal{E}(m)$

$$\begin{aligned}\frac{\frac{\partial \mathcal{N}}{\partial z}}{\mathcal{D}} =& \frac{\xi/\rho}{2r_o D}\Bigg[\left(\frac{2(m-1) - 2 + m}{2(m-1)}\right)\mathcal{E}(m) \\ &- \left(\frac{m}{2} - 2\right)\mathcal{K}(m)\Bigg].\end{aligned} \tag{A.56}$$

$$\begin{aligned}\frac{\frac{\partial \mathcal{N}}{\partial z}}{\mathcal{D}} =& \frac{\xi/\rho}{2r_o D}\Bigg[\left(\frac{3m-4}{2(m-1)}\right)\mathcal{E}(m) \\ &- \left(\frac{m}{2} - 2\right)\mathcal{K}(m)\Bigg].\end{aligned} \tag{A.57}$$

Multiplying and dividing by 2

$$\frac{\frac{\partial \mathcal{N}}{\partial z}}{\mathcal{D}} = \frac{\xi/\rho}{4r_o D}\left[\left(\frac{3m-4}{m-1}\right)\mathcal{E}(m) - (m-4)\mathcal{K}(m)\right]. \tag{A.58}$$

Noting that the fractions outside of the brackets are now the same for both of the simplified expressions for Term 1 (see equation (A.58)) and Term 2 (see equation (A.48), we'll substitute the expression for Term 2 in equation (A.48) and the expression for Term 1 in equation (A.58) back in to equation (A.45).

$$\begin{aligned}\frac{\frac{\partial \mathcal{N}}{\partial z}\mathcal{D} - \mathcal{N}\frac{\partial \mathcal{D}}{\partial z}}{\mathcal{D}^2} = \frac{\xi/\rho}{4r_o D}&\left[\left(\frac{3m-4}{m-1}\right)\mathcal{E}(m) - (m-4)\mathcal{K}(m)\right] \\ &-\frac{\xi/\rho}{4r_o D}\left[2\mathcal{E}(m) + (m-2)\,\mathcal{K}(m)\right].\end{aligned} \tag{A.59}$$

Let's first look at just the difference of the $\mathcal{K}(m)$ terms:

$$((m-1)-(m-2))K = (m-4-m+2)\mathcal{K}(m) = -2\mathcal{K}(m) \tag{A.60}$$

Now just looking at the $\mathcal{E}(m)$ terms:

$$\begin{aligned}&\left(\frac{3m-4}{m-1} - 2\right)\mathcal{E}(m) && \\ &\left(\frac{3m-4-2(m-1)}{m-1}\right)\mathcal{E}(m) && \text{(common denominators)} \\ &\left(\frac{3m-4-2m+2}{m-1}\right)\mathcal{E}(m) && \text{(expand)} \\ &\left(\frac{m-2}{m-1}\right)\mathcal{E}(m) && \text{(simplify)}\end{aligned} \tag{A.61}$$

Applying the definition of m in equation (A.23)

$$\begin{aligned}&\left(\frac{\frac{4\rho}{\mathcal{D}^2} - 2}{\frac{4\rho}{\mathcal{D}^2} - 1}\right)\mathcal{E}(m) && \\ &\left(\frac{\frac{4\rho-2\mathcal{D}^2}{\cancel{\mathcal{D}^2}}}{\frac{4\rho-\mathcal{D}^2}{\cancel{\mathcal{D}^2}}}\right)\mathcal{E}(m) && \text{(common denominators)} \\ &\left(\frac{4\rho-2\mathcal{D}^2}{4\rho-\mathcal{D}^2}\right)\mathcal{E}(m) && \text{(divide)} \\ &2\left(\frac{2\rho-\mathcal{D}^2}{4\rho-\mathcal{D}^2}\right)\mathcal{E}(m) && \text{(pull out a 2)}\end{aligned} \tag{A.62}$$

Expanding out the $\mathcal{D}$ terms

$$
\begin{aligned}
&2\left(\frac{2\rho-((\rho+1)^2+\xi^2)}{4\rho-((\rho+1)^2+\xi^2)}\right)\mathcal{E}(m)\\
&2\left(\frac{\cancel{2\rho}-\rho^2-\cancel{2\rho}-1-\xi^2}{\cancel{4\rho}^{2\rho}-\rho^2-\cancel{2\rho}-1-\xi^2}\right)\mathcal{E}(m) && \text{(expand and cancel)}\\
&2\left(\frac{-\rho^2-1-\xi^2}{2\rho-\rho^2-1-\xi^2}\right)\mathcal{E}(m)\\
&-2\left(\frac{-\rho^2-1-\xi^2}{(\rho-1)^2+\xi^2}\right)\mathcal{E}(m) && \text{(multiply by -1 and simplify)}\\
&-2\left(\frac{-\rho^2-1-\xi^2+2\rho-2\rho}{(\rho-1)^2+\xi^2}\right)\mathcal{E}(m) && \text{(add and subtract } 2\rho)\\
&2\left(\frac{(\rho-1)^2+\xi^2+2\rho}{(\rho-1)^2+\xi^2}\right)\mathcal{E}(m) && \text{(consolidate numerator)}\\
&2\left(\frac{\cancel{(\rho-1)^2+\xi^2}^{1}}{\cancel{(\rho-1)^2+\xi^2}}+\frac{2\rho}{(\rho-1)^2+\xi^2}\right)\mathcal{E}(m) && \text{(split fraction and cancel)}\\
&2\left(1+\frac{2\rho}{\xi^2+(\rho-1)^2}\right)\mathcal{E}(m)
\end{aligned}
\tag{A.63}
$$

Now putting the $\mathcal{K}(m)$ terms from equation (A.60) and the $\mathcal{E}(m)$ terms from equation (A.63) together in the difference, remembering the fraction out front of both Term 1 and Term 2:

$$
v_r = -\mathcal{C}\left[\frac{\xi/\rho}{\cancel{4}^{2}\mathcal{D}r_o}\left(-\cancel{2}\mathcal{K}(m)+\cancel{2}\left[1+\frac{2\rho}{\xi^2+(\rho-1)^2}\right]\mathcal{E}(m)\right)\right] \tag{A.64}
$$

And finally expanding out $\mathcal{C}$ and $\mathcal{D}$ as well as some minor cleanup and rearranging we have the expression presented in equation (A.126b):

$$
\boxed{v_r = -\frac{\Gamma}{2\pi r_o}\frac{\xi/\rho}{[\xi^2+(\rho+1)^2]^{1/2}}\left(\mathcal{K}(m)-\left[1+\frac{2\rho}{\xi^2+(\rho-1)^2}\right]\mathcal{E}(m)\right)} \tag{A.65}
$$

A.3 Axially Induced Velocity Component

Next let's simplify equation (A.44)

$$v_z = C\left[\underbrace{\frac{\mathcal{N}\mathcal{D}}{r\mathcal{D}^2}}_{\text{Term 1}} + \underbrace{\frac{r\frac{\partial\mathcal{N}}{\partial r}\mathcal{D}}{rD^2}}_{\text{Term 2}} - \underbrace{\frac{(\mathcal{N}r)\frac{\partial\mathcal{D}}{\partial r}}{r\mathcal{D}^2}}_{\text{Term 3}}\right]. \tag{A.66}$$

We'll first expand the partials. Term 1 has no partials to expand:

$$\text{Term 1} = \frac{\mathcal{N}\mathcal{D}}{r\mathcal{D}^2}. \tag{A.67}$$

Term 2 has several sets of partials to expand:

$$\begin{aligned}\text{Term 2} = &\frac{r\mathcal{D}}{r\mathcal{D}^2}\frac{\partial m}{\partial\rho}\frac{\partial\rho}{\partial r}\left[-\frac{3\mathcal{E}(m)+(m-5)\mathcal{K}(m)}{2m(m-1)}\right.\\ &\left.+\frac{2\mathcal{E}(m)-2\mathcal{K}(m)}{m^2(m-1)}\right],\end{aligned} \tag{A.68}$$

$$\begin{aligned}\text{Term 2} = &\frac{r\mathcal{D}}{r\mathcal{D}^2}\frac{4(-\rho^2+\xi^2+1)}{\mathcal{D}^4}\frac{1}{r_o}\left[-\frac{3\mathcal{E}(m)+(m-5)\mathcal{K}(m)}{2m(m-1)}\right.\\ &\left.+\frac{2\mathcal{E}(m)-2\mathcal{K}(m)}{m^2(m-1)}\right].\end{aligned} \tag{A.69}$$

Term 3 also has a couple sets of partials to expand:

$$\text{Term 3} = -\frac{\mathcal{N}r}{r\mathcal{D}^2}\frac{\partial\rho}{\partial r}\frac{\rho+1}{\mathcal{D}}, \tag{A.70}$$

$$\text{Term 3} = -\frac{\mathcal{N}r}{r\mathcal{D}^2}\frac{1}{r_o}\frac{\rho+1}{\mathcal{D}}. \tag{A.71}$$

Next let's expand out the $\mathcal{N}$'s. For Term 1

$$\text{Term 1} = \frac{\mathcal{D}}{r\mathcal{D}^2}\left[\frac{2}{m}\mathcal{E}(m)+\frac{m-2}{m}\mathcal{K}(m)\right]. \tag{A.72}$$

Term 2 is already expanded, but let us gather the $\mathcal{E}(m)$ and $\mathcal{K}(m)$ terms.

$$\begin{aligned}\text{Term 2} = \frac{r\mathcal{D}}{r\mathcal{D}^2}\frac{4(-\rho^2+\xi^2+1)}{\mathcal{D}^4}\frac{1}{r_o}\left[-\frac{3m-4}{2m^2(m-1)}\mathcal{E}(m)\right.\\ \left.-\frac{(m-4)(m-1)}{2m^2(m-1)}\mathcal{K}(m)\right].\end{aligned} \tag{A.73}$$

For Term 3:

$$\text{Term 3} = -\frac{r}{r\mathcal{D}^2}\frac{1}{r_o}\frac{\rho+1}{\mathcal{D}}\left[\frac{2}{m}\mathcal{E}(m)+\frac{m-2}{m}\mathcal{K}(m)\right]. \tag{A.74}$$

In order to add the terms together, we require a common denominator. Let us gather the multipliers of each of the terms to see what we're working with and decide what common denominator to choose.

$$\text{Term 1 Multiplier} = \frac{\mathcal{D}}{r\mathcal{D}^2 m}; \tag{A.75}$$

$$\text{Term 2 Multiplier} = \frac{4r\mathcal{D}(-\rho^2+\xi^2+1)}{2rr_o\mathcal{D}^6 m^2(m-1)}; \tag{A.76}$$

$$\text{Term 3 Multiplier} = \frac{r(\rho+1)}{rr_o\mathcal{D}^3 m}. \tag{A.77}$$

We may expect our final expression to look similar to the expression for v_r, so we may want to make sure to keep a $r_o D$ in the denominator as we go forward. Therefore we'll start by multiplying Term 1 by r_o/r_o:

$$\text{Term 1 Multiplier} = \frac{\mathcal{D}r_o}{rr_o\mathcal{D}^2 m}; \tag{A.78}$$

$$\text{Term 2 Multiplier} = \frac{4r\mathcal{D}(-\rho^2+\xi^2+1)}{2rr_o\mathcal{D}^6 m^2(m-1)}; \tag{A.79}$$

$$\text{Term 3 Multiplier} = \frac{r(\rho+1)}{rr_o\mathcal{D}^3 m}. \tag{A.80}$$

Term 2 seems to have some extraneous values, so let's divide out the 2 and one of the $\mathcal{D}$'s,

$$\text{Term 1 Multiplier} = \frac{\mathcal{D}r_o}{rr_o\mathcal{D}^2 m}; \tag{A.81}$$

$$\text{Term 2 Multiplier} = \frac{2r(-\rho^2+\xi^2+1)}{rr_o\mathcal{D}^5 m^2(m-1)}; \tag{A.82}$$

$$\text{Term 3 Multiplier} = \frac{r(\rho+1)}{rr_o\mathcal{D}^3 m}. \tag{A.83}$$

Now we just need to multiply the top and bottom of Term 1 by $\mathcal{D}^3 m(m-1)$ and the top and bottom of Term 3 by $\mathcal{D}^2 m(m-1)$ to get a common denominator between the terms.

$$\text{Term 1 Multiplier} = \frac{r_o\mathcal{D}^4 m(m-1)}{rr_o\mathcal{D}^5 m^2(m-1)}; \tag{A.84}$$

$$\text{Term 2 Multiplier} = \frac{2r(-\rho^2+\xi^2+1)}{rr_o\mathcal{D}^5 m^2(m-1)}; \tag{A.85}$$

$$\text{Term 3 Multiplier} = \frac{r(\rho+1)\mathcal{D}^2 m(m-1)}{rr_o\mathcal{D}^5 m^2(m-1)}. \tag{A.86}$$

With a common denominator in place, we can start to add the various terms together. Let us try to begin with the $\mathcal{K}(m)$ terms:

$$\frac{\mathcal{K}(m)}{r r_o \mathcal{D}^5 m^2 (m-1)}\Big[r_o \mathcal{D}^4 m(m-1)(m-2) \quad \text{(from Term 1)}$$
$$- 2r(-\rho^2+\xi^2+1)(m-4)(m-1) \quad \text{(from Term 2)}$$
$$- r(\rho+1)\mathcal{D}^2 m(m-1)(m-2)\Big]. \quad \text{(from Term 3)} \tag{A.87}$$

We see immediately that we can cancel out the $(m-1)$ from all the terms.

$$\frac{\mathcal{K}(m)}{r r_o \mathcal{D}^5 m^2}\Big[r_o \mathcal{D}^4 m(m-2) \quad \text{(from Term 1)}$$
$$- 2r(-\rho^2+\xi^2+1)(m-4) \quad \text{(from Term 2)} \tag{A.88}$$
$$- r(\rho+1)\mathcal{D}^2 m(m-2)\Big]. \quad \text{(from Term 3)}$$

Unfortunately, that appears to be the only obvious cancellation to make right away. Perhaps expanding things out more will help. Let us expand the m's out next, remembering that $m = 4\rho/\mathcal{D}^2$.

$$\frac{\mathcal{K}(m)\cancel{\mathcal{D}^4}}{r r_o \cancel{\mathcal{D}^5} \cancel{16}\cancel{\rho^2}}\Big[r_o \cancel{\mathcal{D}^4}\frac{\cancel{4}\rho}{\cancel{\mathcal{D}^2}}\left(\frac{4\rho}{\mathcal{D}^2}-2\right) \quad \text{(from Term 1)}$$
$$- 2r(-\rho^2+\xi^2+1)\left(\frac{\cancel{4}\rho}{\mathcal{D}^2}-\cancel{4}\right) \quad \text{(from Term 2)} \tag{A.89}$$
$$- r(\rho+1)\cancel{\mathcal{D}^2}\frac{\cancel{4}\rho}{\cancel{\mathcal{D}^2}}\left(\frac{4\rho}{\mathcal{D}^2}-2\right)\Big]; \quad \text{(from Term 3)}$$

then canceling out the obvious items and cleaning up:

$$\frac{\mathcal{K}(m)}{4\rho^2 r r_o \mathcal{D}}\Big[\rho r_o \mathcal{D}^2\left(\frac{4\rho}{\mathcal{D}^2}-2\right) \quad \text{(from Term 1)}$$
$$- 2r(-\rho^2+\xi^2+1)\left(\frac{\rho}{\mathcal{D}^2}-1\right) \quad \text{(from Term 2)} \tag{A.90}$$
$$- \rho r(\rho+1)\left(\frac{4\rho}{\mathcal{D}^2}-2\right)\Big]. \quad \text{(from Term 3)}$$

We see that $r_o\rho = r$, which gives us a mutual r that we can cancel out of all the terms.

$$\frac{\mathcal{K}(m)}{4\rho^2 r_o \mathcal{D}}\Big[\mathcal{D}^2\left(\frac{4\rho}{\mathcal{D}^2}-2\right) \quad \text{(from Term 1)}$$
$$- 2(-\rho^2+\xi^2+1)\left(\frac{\rho}{\mathcal{D}^2}-1\right) \quad \text{(from Term 2)} \tag{A.91}$$
$$- \rho(\rho+1)\left(\frac{4\rho}{\mathcal{D}^2}-2\right)\Big]. \quad \text{(from Term 3)}$$

We also see that we can cancel out an additional 2 from everything.

$$\frac{\mathcal{K}(m)}{2\mathcal{D}r_o\rho^2}\Bigg[\mathcal{D}^2\left(\frac{2\rho}{\mathcal{D}^2}-1\right) \quad \text{(from Term 1)}$$
$$-(-\rho^2+\xi^2+1)\left(\frac{\rho}{\mathcal{D}^2}-1\right) \quad \text{(from Term 2)} \tag{A.92}$$
$$-\rho(\rho+1)\left(\frac{2\rho}{\mathcal{D}^2}-1\right)\Bigg]. \quad \text{(from Term 3)}$$

We've found ourselves with some more uncommon denominators, so let's expand and gather terms.

$$\frac{\mathcal{K}(m)}{2\mathcal{D}r_o\rho^2}\Bigg[2\rho-\mathcal{D}^2 \quad \text{(from Term 1)}$$
$$-\frac{-\rho^3+\rho\xi^2+\rho}{\mathcal{D}^2}-\rho^2+\xi^2+1 \quad \text{(from Term 2)} \tag{A.93}$$
$$-\frac{2\rho^3+2\rho^2}{\mathcal{D}^2}+\rho^2+\rho\Bigg]; \quad \text{(from Term 3)}$$

$$\frac{\mathcal{K}(m)}{2\mathcal{D}r_o\rho^2}\Bigg[2\rho-\mathcal{D}^2-\cancel{\rho^2}+\xi^2+1+\cancel{\rho^2}+\rho$$
$$-\frac{-\rho^3+\rho\xi^2+\rho}{\mathcal{D}^2}-\frac{2\rho^3+2\rho^2}{\mathcal{D}^2}\Bigg]. \tag{A.94}$$

Expanding out the $\mathcal{D}$ in the numerator:

$$\frac{\mathcal{K}(m)}{2\mathcal{D}r_o\rho^2}\Bigg[\cancel{3}\rho+\cancel{\xi^2}+\cancel{1}-(\rho^2+\cancel{2\rho}+\cancel{1}+\cancel{\xi^2})$$
$$-\frac{-\rho^3+\rho\xi^2+\rho}{\mathcal{D}^2}-\frac{2\rho^3+2\rho^2}{\mathcal{D}^2}\Bigg]. \tag{A.95}$$

Now let's get a common denominator again, pulling the ρ^2 inside the brackets.

$$\frac{\mathcal{K}(m)}{2\mathcal{D}r_o}\left[\frac{\rho\mathcal{D}^2-\rho^2\mathcal{D}^2+\cancel{\rho^3}-\rho\xi^2-\rho-\cancel{2}\rho^3-2\rho^2}{\mathcal{D}^2\rho^2}\right]. \tag{A.96}$$

We can immediately cancel out a ρ:

$$\frac{\mathcal{K}(m)}{2\mathcal{D}r_o}\left[\frac{\mathcal{D}^2-(\rho^2+2\rho+1+\xi^2)-\rho\mathcal{D}^2}{\mathcal{D}^2\rho}\right]. \tag{A.97}$$

We also see that $\mathcal{D}^2=\rho^2+2\rho+1+\xi^2$, which cancels in the numerator.

$$\frac{\mathcal{K}(m)}{2\mathcal{D}r_o}\left[\frac{-\rho\mathcal{D}^2}{\rho\mathcal{D}^2}\right]. \tag{A.98}$$

We are finally left with

$$-\frac{\mathcal{K}(m)}{2\mathcal{D}r_o}. \tag{A.99}$$

Now let's look at the $\mathcal{E}(m)$ terms start back with the term multipliers with common denominators: equations (A.84) to (A.86).

$$\begin{aligned}\frac{\mathcal{E}(m)}{rr_o\mathcal{D}^5m^2(m-1)}\Big[&2r_o\mathcal{D}^4m(m-1) && \text{(from Term 1)}\\ &-2r(-\rho^2+\xi^2+1)(3m-4) && \text{(from Term 2)}\\ &-2r(\rho+1)\mathcal{D}^2m(m-1)\Big]. && \text{(from Term 3)}\end{aligned} \tag{A.100}$$

Unlike the $\mathcal{K}(m)$ terms, it doesn't appear as though anything will cancel out immediately. Let's take a similar approach as before and expand out the m terms.

$$\begin{aligned}\frac{\mathcal{E}(m)}{rr_o\mathcal{D}^5m^2(m-1)}\Big[&2r_o\mathcal{D}^4\left(\frac{4\rho}{\mathcal{D}^2}\right)\left(\frac{4\rho}{\mathcal{D}^2}\right)-1) && \text{(from Term 1)}\\ &-2r(-\rho^2+\xi^2+1)\left(3\left(\frac{4\rho}{\mathcal{D}^2}\right)-4\right) && \text{(from Term 2)}\\ &-2r(\rho+1)\mathcal{D}^2\left(\frac{4\rho}{\mathcal{D}^2}\right)\left(\frac{4\rho}{\mathcal{D}^2}\right)-1)\Big]. && \text{(from Term 3)}\end{aligned} \tag{A.101}$$

Again noting that $r_o\rho = r$, we can cancel out an r.

$$\begin{aligned}\frac{\mathcal{E}(m)}{r_o\mathcal{D}^5m^2(m-1)}\Big[&2\mathcal{D}^4\left(\frac{4}{\mathcal{D}^2}\right)\left(\frac{4\rho}{\mathcal{D}^2}\right)-1) && \text{(from Term 1)}\\ &-2(-\rho^2+\xi^2+1)\left(3\left(\frac{4\rho}{\mathcal{D}^2}\right)-4\right) && \text{(from Term 2)}\\ &-2(\rho+1)\mathcal{D}^2\left(\frac{4\rho}{\mathcal{D}^2}\right)\left(\frac{4\rho}{\mathcal{D}^2}\right)-1)\Big]. && \text{(from Term 3)}\end{aligned} \tag{A.102}$$

We may also want to expand the m^2 on the outside—

$$\frac{1}{r_o\mathcal{D}^5m^2(m-1)} = \frac{\cancel{\mathcal{D}^4}}{r_o\mathcal{D}^{\cancel{5}}16\rho^2(m-1)} \tag{A.103}$$

—which leaves us with

$$\frac{\mathcal{E}(m)}{r_o \mathcal{D} 16\rho^2(m-1)}\Bigg[2\mathcal{D}^4\left(\frac{4}{\mathcal{D}^2}\right)\left(\frac{4\rho}{\mathcal{D}^2}\right)-1) \quad \text{(from Term 1)}$$
$$-2(-\rho^2+\xi^2+1)\left(3\left(\frac{4\rho}{\mathcal{D}^2}\right)-4\right) \quad \text{(from Term 2)}$$
$$-2(\rho+1)\mathcal{D}^2\left(\frac{4\rho}{\mathcal{D}^2}\right)\left(\frac{4\rho}{\mathcal{D}^2}\right)-1)\Bigg]. \quad \text{(from Term 3)} \tag{A.104}$$

We can now take an 8 out of everything:

$$\frac{\mathcal{E}(m)}{2\mathcal{D} r_o \rho^2(m-1)}\Bigg[\mathcal{D}^{\cancel{4}^{\,2}}\left(\frac{1}{\cancel{\mathcal{D}^2}}\right)\left(\frac{4\rho}{\mathcal{D}^2}\right)-1) \quad \text{(from Term 1)}$$
$$-(-\rho^2+\xi^2+1)\left(3\left(\frac{\rho}{\mathcal{D}^2}\right)-1\right) \quad \text{(from Term 2)}$$
$$-(\rho+1)\cancel{\mathcal{D}^2}\left(\frac{\rho}{\cancel{\mathcal{D}^2}}\right)\left(\frac{4\rho}{\mathcal{D}^2}\right)-1)\Bigg]. \quad \text{(from Term 3)} \tag{A.105}$$

Cleaning up a bit:

$$\frac{\mathcal{E}(m)}{2\mathcal{D} r_o \rho^2(m-1)}\Bigg[\mathcal{D}^2\left(\frac{4\rho}{\mathcal{D}^2}\right)-1) \quad \text{(from Term 1)}$$
$$-(-\rho^2+\xi^2+1)\left(3\left(\frac{\rho}{\mathcal{D}^2}\right)-1\right) \quad \text{(from Term 2)}$$
$$-(\rho+1)\rho\left(\frac{4\rho}{\mathcal{D}^2}\right)-1)\Bigg]. \quad \text{(from Term 3)} \tag{A.106}$$

Let's next expand out the multiplications.

$$\frac{\mathcal{E}(m)}{2\mathcal{D} r_o \rho^2(m-1)}\Bigg[4\rho-\mathcal{D}^2 \quad \text{(from Term 1)}$$
$$-\frac{-3\rho^3+3\rho\xi^2+3\rho}{\mathcal{D}^2}-\cancel{\rho^2}+\xi^2+1 \quad \text{(from Term 2)}$$
$$-\frac{4\rho^3+4\rho^2}{\mathcal{D}^2}+\cancel{\rho^2}+\rho\Bigg]. \quad \text{(from Term 3)} \tag{A.107}$$

Gathering terms:

$$\frac{\mathcal{E}(m)}{2\mathcal{D} r_o \rho^2(m-1)}\left[5\rho+\xi+1-\mathcal{D}^2 \quad -\frac{-3\rho^3+3\rho\xi^2+3\rho}{\mathcal{D}^2}-\frac{4\rho^3+4\rho^2}{\mathcal{D}^2}\right]. \tag{A.108}$$

Expanding the $\mathcal{D}$ in the numerator:

$$\frac{\mathcal{E}(m)}{2\mathcal{D}r_o\rho^2(m-1)}\left[\cancel{3}\rho+\cancel{\xi}+\cancel{1}-(\rho^2+\cancel{2\rho}+\cancel{1}+\cancel{\xi}) \quad -\frac{-\cancel{3\rho^3}+3\rho\xi^2+3\rho+\cancel{4}\rho^3+4\rho^2}{\mathcal{D}^2}\right]. \tag{A.109}$$

We can take a ρ out of everything now as well.

$$\frac{\mathcal{E}(m)}{2\mathcal{D}r_o\rho(m-1)}\left[3-\rho \quad -\frac{3\xi^2+3+\rho^2+4\rho}{\mathcal{D}^2}\right]. \tag{A.110}$$

Let's move the 3 into the fraction and expand the $\mathcal{D}$ that will appear in the numerator.

$$\frac{\mathcal{E}(m)}{2\mathcal{D}r_o\rho(m-1)}\left[-\rho-\frac{-\cancel{3}\rho^2-\cancel{6}\rho-\cancel{3}-\cancel{3\xi}+\cancel{3\xi^2}+\cancel{3}+\cancel{\rho^2}+\cancel{4\rho}}{\mathcal{D}^2}\right]. \tag{A.111}$$

After cleaning up the various cancelations, we can take another ρ out of everything.

$$\frac{\mathcal{E}(m)}{2\mathcal{D}r_o(m-1)}\left[-1+\frac{2(\rho+1)}{\mathcal{D}^2}\right]. \tag{A.112}$$

Now let's move the $(m-1)$ into the inside and expand out the m and $\mathcal{D}$ terms.

$$\frac{\mathcal{E}(m)}{2\mathcal{D}r_o}\left[\frac{-1}{\frac{4\rho}{(\rho+1)^2+\xi^2}-1}+\frac{2(\rho+1)}{\left(\frac{4\rho}{(\rho+1)^2+\xi^2}-1\right)\left((\rho+1)^2+\xi^2\right)}\right]. \tag{A.113}$$

Combining fractions:

$$\frac{\mathcal{E}(m)}{2\mathcal{D}r_o}\left[\frac{2\rho+2-(\rho+1)^2-\xi^2}{\left(\frac{4\rho}{(\rho+1)^2+\xi^2}-1\right)\left((\rho+1)^2+\xi^2\right)}\right]. \tag{A.114}$$

Expanding the numerator:

$$\frac{\mathcal{E}(m)}{2\mathcal{D}r_o}\left[\frac{\cancel{2\rho}+\cancel{2}-\rho^2-\cancel{2\rho}-\cancel{1}-\xi^2}{\left(\frac{4\rho}{(\rho+1)^2+\xi^2}-1\right)\left((\rho+1)^2+\xi^2\right)}\right]; \tag{A.115}$$

$$\frac{\mathcal{E}(m)}{2\mathcal{D}r_o}\left[\frac{1-\rho^2-\xi^2}{\left(\frac{4\rho}{(\rho+1)^2+\xi^2}-1\right)\left((\rho+1)^2+\xi^2\right)}\right]. \tag{A.116}$$

Getting a common denominator in the denominator:

$$\frac{\mathcal{E}(m)}{2\mathcal{D}r_o}\left[\frac{1-\rho^2-\xi^2}{4\rho-(\rho+1)^2-\xi^2}\right]. \tag{A.117}$$

Expanding then simplifying the denominator:

$$\frac{\mathcal{E}(m)}{2\mathcal{D}r_o}\left[\frac{1-\rho^2-\xi^2}{\cancel{4}^{2}\rho-\rho^2-\cancel{2\rho}-1-\xi^2}\right]; \tag{A.118}$$

$$\frac{\mathcal{E}(m)}{2\mathcal{D}r_o}\left[\frac{\rho^2-1+\xi^2}{(\rho-1)^2+\xi^2}\right]. \tag{A.119}$$

Adding and subtracting $2\rho+1$ to the numerator:

$$\frac{\mathcal{E}(m)}{2\mathcal{D}r_o}\left[\frac{\rho^2-2\rho+1+\xi^2+2\rho-2}{(\rho-1)^2+\xi^2}\right]. \tag{A.120}$$

Simplifying:

$$\frac{\mathcal{E}(m)}{2\mathcal{D}r_o}\left[\frac{(\rho-1)^2+\xi^2+2(\rho-1)}{(\rho-1)^2+\xi^2}\right]. \tag{A.121}$$

Splitting the fraction:

$$\frac{\mathcal{E}(m)}{2\mathcal{D}r_o}\left[\frac{\cancel{(\rho-1)^2+\xi^2}}{\cancel{(\rho-1)^2+\xi^2}}+\frac{2(\rho-1)}{(\rho-1)^2+\xi^2}\right]. \tag{A.122}$$

Finally, we are left with

$$\frac{\mathcal{E}(m)}{2\mathcal{D}r_o}\left[1+\frac{2(\rho-1)}{(\rho-1)^2+\xi^2}\right]. \tag{A.123}$$

Now combining our $\mathcal{K}(m)$ and $\mathcal{E}(m)$ terms from equation (A.99) and equation (A.123), respectively, we arrive at

$$v_z = C\frac{1}{2\mathcal{D}r_o}\left[-\mathcal{K}(m)+\left(1+\frac{2(\rho-1)}{(\rho-1)^2+\xi^2}\right)\mathcal{E}(m)\right]. \tag{A.124}$$

Expanding out C and $\mathcal{D}$ gives us our final expression as presented in equation (A.126a):

$$v_z = \frac{\Gamma}{2\pi r_o}\frac{1}{\left[\xi^2+(\rho+1)^2\right]^{1/2}}\left[\mathcal{K}(m)-\left(1+\frac{2(\rho-1)}{\xi^2+(\rho-1)^2}\right)\mathcal{E}(m)\right]. \tag{A.125}$$

After some tedious algebra (see Appendix A), we arrive at the following expressions for the unit[a] induced velocity due to a vortex ring.

[a] In other words, we have set $\gamma = 1$

$$v_z^\gamma = \frac{1}{2\pi r_o}\frac{1}{D_1}\left[\mathcal{K}(m) - \left(1 + \frac{2(\rho-1)}{D_2}\right)\mathcal{E}(m)\right] \tag{A.126a}$$

$$v_r^\gamma = -\frac{1}{2\pi r_o}\frac{\xi/\rho}{D_1}\left[\mathcal{K}(m) - \left(1 + \frac{2\rho}{D_2}\right)\mathcal{E}(m)\right] \tag{A.126b}$$

where the superscript, γ, indicates a unit vortex induced velocity. In addition, $\mathcal{K}(m)$ and $\mathcal{E}(m)$ are complete elliptic integrals of the first and second kind, respectively, and

$$m = \left(\frac{4\rho}{\xi^2 + (\rho+1)^2}\right) \tag{A.127}$$

$$\xi = \frac{z - z_o}{r_o} \tag{A.128}$$

$$\rho = \frac{r}{r_o} \tag{A.129}$$

$$D_1 = \left[\xi^2 + (\rho+1)^2\right]^{1/2} \tag{A.130}$$

$$D_2 = \xi^2 + (\rho-1)^2. \tag{A.131}$$

Transformation of Poisson Equations for Wake Elliptic Grid Residual

Appendix **B**

In order to interchange the dependent and independent variables of

$$\xi(z,r) \equiv \xi_{zz} + \xi_{rr} = 0 \tag{B.1a}$$

$$\eta(z,r) \equiv \eta_{zz} + \eta_{rr} = \frac{\psi_r}{r}, \tag{B.1b}$$

where $\eta = \psi$ = constant along streamlines (thus η coordinates correspond to the physical location of streamlines) and ξ is constant along radial lines and can be arbitrarily chosen, we apply the derivative transformations:

$$f_z = \frac{r_\eta f_\xi - r_\xi f_\eta}{J} \tag{B.2a}$$

$$f_r = \frac{-z_\eta f_\xi + z_\xi f_\eta}{J}, \tag{B.2b}$$

where $J = z_\xi r_\eta - z_\eta r_\xi$.

Let's look first at the ξ_{zz} term. We will begin by applying equation (B.2a):

$$\xi_z = \frac{r_\eta \xi_\xi - r_\xi \xi_\eta}{J} \tag{B.3}$$

$$\xi_{zz} = \frac{r_\eta \left(\frac{r_\eta \xi_\xi - r_\xi \xi_\eta}{J}\right)_\xi - r_\xi \left(\frac{r_\eta \xi_\xi - r_\xi \xi_\eta}{J}\right)_\eta}{J}. \tag{B.4}$$

Recognizing that $\xi_\xi = 1$, and $\xi_\eta = 0$ (by orthogonality), we can simplify.

$$\xi_{zz} = \frac{r_\eta \left(\frac{r_\eta}{J}\right)_\xi - r_\xi \left(\frac{r_\eta}{J}\right)_\eta}{J}.$$

Applying the quotient rule:

$$\begin{aligned}\xi_{zz} &= \frac{r_\eta \left(\frac{r_{\eta\xi} J - r_\eta J_\xi}{J^2}\right) - r_\xi \left(\frac{r_{\eta\eta} J - r_\eta J_\eta}{J^2}\right)}{J} \\ &= \frac{r_\eta \left(r_{\eta\xi} J - r_\eta J_\xi\right) - r_\xi \left(r_{\eta\eta} J - r_\eta J_\eta\right)}{100 J^3}.\end{aligned}$$

Expanding:

$$\xi_{zz} = \frac{r_\eta r_{\eta\xi} J - r_\eta^2 J_\xi - r_\xi r_{\eta\eta} J + r_\xi r_\eta J_\eta}{J^3}. \tag{B.5}$$

We'll leave ξ_{zz} here for now and follow the same procedure for ξ_{rr}—beginning by applying equation (B.2b):

$$\xi_r = \frac{-z_\eta \xi_\xi + z_\xi \xi_\eta}{J} \tag{B.6}$$

$$\xi_{rr} = \frac{-z_\eta \left(\frac{-z_\eta \xi_\xi + z_\xi \xi_\eta}{J}\right)_\xi + z_\xi \left(\frac{-z_\eta \xi_\xi + z_\xi \xi_\eta}{J}\right)_\eta}{J}. \tag{B.7}$$

Again recognizing that $\xi_\xi = 1$, and $\xi_\eta = 0$ (by orthogonality), we can simplify:

$$\xi_{rr} = \frac{-z_\eta \left(\frac{-z_\eta}{J}\right)_\xi + z_\xi \left(\frac{-z_\eta}{J}\right)_\eta}{J}. \tag{B.8}$$

Applying the quotient rule:

$$\xi_{rr} = \frac{-z_\eta \left(\frac{-z_{\eta\xi} J + z_\eta J_\xi}{J^2}\right) + z_\xi \left(\frac{-z_{\eta\eta} J + z_\eta J_\eta}{J^2}\right)}{J}. \tag{B.9}$$

Expanding:

$$\xi_{rr} = \frac{z_\eta z_{\eta\xi} J - z_\eta^2 J_\xi - z_\xi z_{\eta\eta} J + z_\xi z_\eta J_\eta}{J^3}. \tag{B.10}$$

Now that we have both ξ_{zz} and ξ_{rr}, let us perform similar transformations for η_{zz} and η_{rr}. Let us begin with equation (B.2a):

$$\eta_z = \frac{r_\eta \eta_\xi - r_\xi \eta_\eta}{J} \tag{B.11}$$

$$\eta_{zz} = \frac{r_\eta \left(\frac{r_\eta \eta_\xi - r_\xi \eta_\eta}{J}\right)_\xi - r_\xi \left(\frac{r_\eta \eta_\xi - r_\xi \eta_\eta}{J}\right)_\eta}{J}. \tag{B.12}$$

Here, $\eta_\xi = 0$ (by orthogonality), and $\eta_\eta = 1$. So we simplify as follows

$$\eta_{zz} = \frac{r_\eta \left(\frac{-r_\xi}{J}\right)_\xi - r_\xi \left(\frac{-r_\xi}{J}\right)_\eta}{J}. \tag{B.13}$$

Applying the quotient rule:

$$\eta_{zz} = \frac{r_\eta \left(\frac{-r_{\xi\xi} J + r_\xi J_\xi}{J^2}\right) - r_\xi \left(\frac{-r_{\xi\eta} J + r_\xi J_\eta}{J^2}\right)}{J}. \tag{B.14}$$

Expanding:

$$\eta_{zz} = \frac{-r_\eta r_{\xi\xi} J + r_\eta r_\xi J_\xi + r_\xi r_{\xi\eta} J - r_\xi^2 J_\eta}{J^3}. \tag{B.15}$$

As we saw above, the expression for η_{rr} will be nearly identical to that for η_{zz}

$$\eta_r = \frac{-z_\eta \eta_\xi + z_\xi \eta_\eta}{J} \tag{B.16}$$

$$\eta_{rr} = \frac{-z_\eta \left(\frac{-z_\eta \eta_\xi + z_\xi \eta_\eta}{J}\right)_\xi + z_\xi \left(\frac{-z_\eta \eta_\xi + z_\xi \eta_\eta}{J}\right)_\eta}{J}. \tag{B.17}$$

Again recognizing that $\eta_\xi = 0$, and $\eta_\eta = 1$, we simplify:

$$\eta_{rr} = \frac{-z_\eta \left(\frac{z_\xi}{J}\right)_\xi + z_\xi \left(\frac{z_\xi}{J}\right)_\eta}{J}. \tag{B.18}$$

Applying the quotient rule:

$$\eta_{rr} = \frac{-z_\eta \left(\frac{z_{\xi\xi} J - z_\xi J_\xi}{J^2}\right) + z_\xi \left(\frac{z_{\xi\eta} J - z_\xi J_\eta}{J^2}\right)}{J}. \tag{B.19}$$

Expanding:

$$\eta_{rr} = \frac{-z_\eta z_{\xi\xi} J + z_\eta z_\xi J_\xi + z_\xi z_{\xi\eta} J - z_\xi^2 J_\eta}{J^3}. \tag{B.20}$$

Before putting everything together, we also need to transform the right hand side of equation (B.1b) using equation (B.2b) as we have done, noting in this case that we only have a single, rather than a double, derivative.

$$\frac{1}{r}\psi_r = \frac{-z_\eta \psi_\xi + z_\xi \psi_\eta}{rJ}. \tag{B.21}$$

Remembering that we have chosen $\psi = \eta$, and making similar simplifications with the derivitives we have thus far ($\eta_\eta = 1,\ \eta_\xi = 0$), we are left with

$$\frac{1}{r}\psi_r = \frac{z_\xi}{rJ}. \tag{B.22}$$

Let's now bring it all together in the Poisson equations to see where we are, multiplying everything by J^3 to remove all the fractions. For convenience and clarity, we'll also note that $(\cdot)_{\xi\eta} = (\cdot)_{\eta\xi}$ and put every instance in the $\xi\eta$ order.

$$\left[r_\eta r_{\xi\eta} J - r_\eta^2 J_\xi - r_\xi r_{\eta\eta} J + r_\xi r_\eta J_\eta\right] + \left[z_\eta z_{\xi\eta} J - z_\eta^2 J_\xi - z_\xi z_{\eta\eta} J + z_\xi z_\eta J_\eta\right] = 0 \tag{B.23a}$$

$$\left[-r_\eta r_{\xi\xi} J + r_\eta r_\xi J_\xi + r_\xi r_{\xi\eta} J - r_\xi^2 J_\eta\right] + \left[-z_\eta z_{\xi\xi} J + z_\eta z_\xi J_\xi + z_\xi z_{\xi\eta} J - z_\xi^2 J_\eta\right] = \frac{z_\xi J^2}{r}. \tag{B.23b}$$

In order to get the final $z(\xi, \eta)$ and $r(\xi, \eta)$ relations, we'll first need to do some more expanding, specifically of the jacobian (and its derivatives, applying the product rule):

$$J = z_\xi r_\eta - z_\eta r_\xi \tag{B.24a}$$
$$J_\xi = z_{\xi\xi} r_\eta + z_\xi r_{\xi\eta} - z_{\xi\eta} r_\xi - z_\eta r_{\xi\xi} \tag{B.24b}$$
$$J_\eta = z_{\xi\eta} r_\eta + z_\xi r_{\eta\eta} - z_{\eta\eta} r_\xi - z_\eta r_{\xi\eta}. \tag{B.24c}$$

Now we just need to expand everything out. Let's start with the transformation of the ξ_{zz} term (first term on the left hand side of equation (B.23a)). As we expand things out, we'll also rearrange terms to facilitate easier comparison.

$$\begin{aligned}
\xi_{zz} =& r_\eta r_{\xi\eta}(z_\xi r_\eta - z_\eta r_\xi) \\
& - r_\eta^2(z_{\xi\xi} r_\eta + z_\xi r_{\xi\eta} - z_{\xi\eta} r_\xi - z_\eta r_{\xi\xi}) \\
& - r_\xi r_{\eta\eta}(z_\xi r_\eta - z_\eta r_\xi) \\
& + r_\xi r_\eta(z_{\xi\eta} r_\eta + z_\xi r_{\eta\eta} - z_{\eta\eta} r_\xi - z_\eta r_{\xi\eta}) \\
=& \cancel{z_\xi r_{\xi\eta} r_\eta^2} - z_\eta r_\xi r_{\xi\eta} r_\eta \\
& - z_{\xi\xi} r_\eta^3 - \cancel{z_\xi r_{\xi\eta} r_\eta^2} + z_{\xi\eta} r_\xi r_\eta^2 + z_\eta r_{\xi\xi} r_\eta^2 \\
& - \cancel{z_\xi r_\xi r_{\eta\eta} r_\eta} + z_\eta r_\xi^2 r_{\eta\eta} \\
& + z_{\xi\eta} r_\xi r_\eta^2 + \cancel{z_\xi r_\xi r_{\eta\eta} r_\eta} - z_{\eta\eta} r_\xi^2 r_\eta - z_\eta r_\xi r_{\xi\eta} r_\eta \\
=& - z_{\xi\xi} r_\eta^3 - z_{\eta\eta} r_\xi^2 r_\eta \\
& - 2 z_\eta r_\xi r_{\xi\eta} r_\eta + 2 z_{\xi\eta} r_\xi r_\eta^2 \\
& + z_\eta r_{\xi\xi} r_\eta^2 + z_\eta r_\xi^2 r_{\eta\eta}.
\end{aligned} \tag{B.25}$$

Now ξ_{rr} (second term in equation (B.23a)):

$$\begin{aligned}
\xi_{rr} =& z_\eta z_{\xi\eta}(z_\xi r_\eta - z_\eta r_\xi) \\
&- z_\eta^2(z_{\xi\xi} r_\eta + z_\xi r_{\xi\eta} - z_{\xi\eta} r_\xi - z_\eta r_{\xi\xi}) \\
&- z_\xi z_{\eta\eta}(z_\xi r_\eta - z_\eta r_\xi) \\
&+ z_\xi z_\eta(z_{\xi\eta} r_\eta + z_\xi r_{\eta\eta} - z_{\eta\eta} r_\xi - z_\eta r_{\xi\eta}) \\
=& z_\xi z_{\xi\eta} z_\eta r_\eta - \cancel{z_{\xi\eta} z_\eta^2 r_\xi} \\
&- z_{\xi\xi} z_\eta^2 r_\eta - z_\xi z_\eta^2 r_{\xi\eta} + \cancel{z_{\xi\eta} z_\eta^2 r_\xi} + z_\eta^3 r_{\xi\xi} \\
&- z_\xi^2 z_{\eta\eta} r_\eta + \cancel{z_\xi z_{\eta\eta} z_\eta r_\xi} \\
&+ z_\xi z_{\xi\eta} z_\eta r_\eta + z_\xi^2 z_\eta r_{\eta\eta} - \cancel{z_\xi z_{\eta\eta} z_\eta r_\xi} - z_\xi z_\eta^2 r_{\xi\eta} \\
=& - z_{\xi\xi} z_\eta^2 r_\eta - z_\xi^2 z_{\eta\eta} r_\eta \\
&+ 2 z_\xi z_{\xi\eta} z_\eta r_\eta - 2 z_\xi z_\eta^2 r_{\xi\eta} \\
&+ z_\eta^3 r_{\xi\xi} + z_\xi^2 z_\eta r_{\eta\eta}.
\end{aligned} \tag{B.26}$$

Next η_{zz} (first term in equation (B.23b)):

$$\begin{aligned}
\eta_{zz} =& - r_\eta r_{\xi\xi}(z_\xi r_\eta - z_\eta r_\xi) \\
&+ r_\eta r_\xi(z_{\xi\xi} r_\eta + z_\xi r_{\xi\eta} - z_{\xi\eta} r_\xi - z_\eta r_{\xi\xi}) \\
&+ r_\xi r_{\xi\eta}(z_\xi r_\eta - z_\eta r_\xi) \\
&- r_\xi^2(z_{\xi\eta} r_\eta + z_\xi r_{\eta\eta} - z_{\eta\eta} r_\xi - z_\eta r_{\xi\eta}) \\
=& - z_\xi r_{\xi\xi} r_\eta^2 + \cancel{z_\eta r_{\xi\xi} r_\xi r_\eta} \\
&+ z_{\xi\xi} r_\xi r_\eta^2 + z_\xi r_\xi r_{\xi\eta} r_\eta - z_{\xi\eta} r_\xi^2 r_\eta - \cancel{z_\eta r_{\xi\xi} r_\xi r_\eta} \\
&+ z_\xi r_\xi r_{\xi\eta} r_\eta - \cancel{z_\eta r_\xi^2 r_{\xi\eta}} \\
&- z_{\xi\eta} r_\xi^2 r_\eta - z_\xi r_\xi^2 r_{\eta\eta} + z_{\eta\eta} r_\xi^3 + \cancel{z_\eta r_\xi^2 r_{\xi\eta}} \\
=& z_{\xi\xi} r_\xi r_\eta^2 + z_{\eta\eta} r_\xi^3 \\
&+ 2 z_\xi r_\xi r_{\xi\eta} r_\eta - 2 z_{\xi\eta} r_\xi^2 r_\eta \\
&- z_\xi r_{\xi\xi} r_\eta^2 - z_\xi r_\xi^2 r_{\eta\eta}.
\end{aligned} \tag{B.27}$$

Then η_{rr} (second term in equation (B.23b)):

$$\begin{aligned}
\eta_{rr} =& - z_\eta z_{\xi\xi}(z_\xi r_\eta - z_\eta r_\xi) \\
&+ z_\eta z_\xi(z_{\xi\xi} r_\eta + z_\xi r_{\xi\eta} - z_{\xi\eta} r_\xi - z_\eta r_{\xi\xi}) \\
&+ z_\xi z_{\xi\eta}(z_\xi r_\eta - z_\eta r_\xi) \\
&- z_\xi^2(z_{\xi\eta} r_\eta + z_\xi r_{\eta\eta} - z_{\eta\eta} r_\xi - z_\eta r_{\xi\eta}) \\
=& - \cancel{z_{\xi\xi} z_\xi z_\eta r_\eta} + z_{\xi\xi} z_\eta^2 r_\xi \\
&+ \cancel{z_{\xi\xi} z_\xi z_\eta r_\eta} + z_\xi^2 z_\eta r_{\xi\eta} - z_\xi z_{\xi\eta} z_\eta r_\xi - z_\xi z_\eta^2 r_{\xi\xi} \\
&+ \cancel{z_\xi^2 z_{\xi\eta} r_\eta} - z_\xi z_{\xi\eta} z_\eta r_\xi \\
&- \cancel{z_\xi^2 z_{\xi\eta} r_\eta} - z_\xi^3 r_{\eta\eta} + z_\xi^2 z_{\eta\eta} r_\xi + z_\xi^2 z_\eta r_{\xi\eta} \\
=& z_{\xi\xi} z_\eta^2 r_\xi + z_\xi^2 z_{\eta\eta} r_\xi \\
&+ 2 z_\xi^2 z_\eta r_{\xi\eta} - 2 z_\xi z_{\xi\eta} z_\eta r_\xi \\
&- z_\xi z_\eta^2 r_{\xi\xi} - z_\xi^3 r_{\eta\eta}.
\end{aligned} \tag{B.28}$$

Finally, we'll partially expand the right hand side term of equation (B.23b):

$$\frac{z_\xi J^2}{r} = \frac{J}{r} z_\xi (z_\xi r_\eta - z_\eta r_\xi). \tag{B.29}$$

Let's first look at the case where both parametric expressions are Laplace equations, that is to say, if the right hand side of equation (B.1b) was zero. We can put our expanded expressions back together, gathering like terms.

$$\begin{aligned}
\xi_{zz} + \xi_{rr} =& - z_{\xi\xi}(z_\eta^2 + r_\eta^2) r_\eta \\
&- z_{\eta\eta}(z_\xi^2 + r_\xi^2) r_\eta \\
&+ 2 z_{\xi\eta}(z_\xi z_\eta + r_\xi r_\eta) r_\eta \\
&- 2 r_{\xi\eta}(z_\xi z_\eta + r_\xi r_\eta) z_\eta \\
&+ r_{\xi\xi}(z_\eta^2 + r_\eta^2) z_\eta \\
&+ r_{\eta\eta}(z_\xi^2 + r_\xi^2) z_\eta
\end{aligned} \tag{B.30a}$$

$$\begin{aligned}
\eta_{zz} + \eta_{rr} =& z_{\xi\xi}(z_\eta^2 + r_\eta^2) r_\xi \\
&+ z_{\eta\eta}(z_\xi^2 + r_\xi^2) r_\xi \\
&- 2 z_{\xi\eta}(z_\xi z_\eta + r_\xi r_\eta) r_\xi \\
&+ 2 r_{\xi\eta}(z_\xi z_\eta + r_\xi r_\eta) z_\xi \\
&- r_{\xi\xi}(z_\eta^2 + r_\eta^2) z_\xi \\
&- r_{\eta\eta}(z_\xi^2 + r_\xi^2) z_\xi.
\end{aligned} \tag{B.30b}$$

What we actually need from the above equations is $z(\xi, \eta)$ and $r(\xi, \eta)$, so we'll equate the two expressions and put the z terms together, and the r terms together.

$$\begin{aligned} 0 =& z_{\xi\xi}(z_\eta^2 + r_\eta^2)(r_\xi - r_\eta) \\ & - 2z_{\xi\eta}(z_\xi z_\eta + r_\xi r_\eta)(r_\xi - r_\eta) \\ & + z_{\eta\eta}(z_\xi^2 + r_\xi^2)(r_\xi - r_\eta) \end{aligned} \tag{B.31a}$$

$$\begin{aligned} 0 =& r_{\xi\xi}(z_\eta^2 + r_\eta^2)(z_\xi - z_\eta) \\ & - 2r_{\xi\eta}(z_\xi z_\eta + r_\xi r_\eta)(z_\xi - z_\eta) \\ & + r_{\eta\eta}(z_\xi^2 + r_\xi^2)(z_\xi - z_\eta). \end{aligned} \tag{B.31b}$$

Since both of the expressions equal zero, we can divide out the common terms and we are left with

$$z(\xi, \eta) \equiv \alpha z_{\xi\xi} - 2\beta z_{\xi\eta} + \gamma z_{\eta\eta} = 0 \tag{B.32a}$$

$$r(\xi, \eta) \equiv \alpha r_{\xi\xi} - 2\beta r_{\xi\eta} + \gamma r_{\eta\eta} = 0. \tag{B.32b}$$

where

$$\alpha = z_\eta^2 + r_\eta^2 \tag{B.33a}$$

$$\beta = z_\xi z_\eta + r_\xi r_\eta \tag{B.33b}$$

$$\gamma = z_\xi^2 + r_\xi^2. \tag{B.33c}$$

Now in the case where the right hand side of equation (B.1b) is not zero, we need to apply some more considerations rather than simply equating things and dividing out terms. Putting things together with the full Poisson equations we have

$$\begin{aligned}\xi_{zz} + \xi_{rr} =& - z_{\xi\xi}(z_\eta^2 + r_\eta^2)r_\eta \\ & - z_{\eta\eta}(z_\xi^2 + r_\xi^2)r_\eta \\ & + 2z_{\xi\eta}(z_\xi z_\eta + r_\xi r_\eta)r_\eta \\ & - 2r_{\xi\eta}(z_\xi z_\eta + r_\xi r_\eta)z_\eta \\ & + r_{\xi\xi}(z_\eta^2 + r_\eta^2)z_\eta \\ & + r_{\eta\eta}(z_\xi^2 + r_\xi^2)z_\eta\end{aligned} \tag{B.34a}$$

$$\begin{aligned}\eta_{zz} + \eta_{rr} - \frac{\eta_r}{r} =& z_{\xi\xi}(z_\eta^2 + r_\eta^2)r_\xi \\ & + z_{\eta\eta}(z_\xi^2 + r_\xi^2)r_\xi \\ & - 2z_{\xi\eta}(z_\xi z_\eta + r_\xi r_\eta)r_\xi \\ & + 2r_{\xi\eta}(z_\xi z_\eta + r_\xi r_\eta)z_\xi \\ & - r_{\xi\xi}(z_\eta^2 + r_\eta^2)z_\xi \\ & - r_{\eta\eta}(z_\xi^2 + r_\xi^2)z_\xi \\ & - \frac{J}{r}z_\xi(r_\eta)z_\xi \\ & + \frac{J}{r}z_\xi(z_\eta)r_\xi.\end{aligned} \tag{B.34b}$$

To help combine things, we'll add and subtract the same expression from equation (B.35).

$$\begin{aligned}\xi_{zz} + \xi_{rr} =& - z_{\xi\xi}(z_\eta^2 + r_\eta^2)r_\eta \\ & - z_{\eta\eta}(z_\xi^2 + r_\xi^2)r_\eta \\ & + 2z_{\xi\eta}(z_\xi z_\eta + r_\xi r_\eta)r_\eta \\ & - 2r_{\xi\eta}(z_\xi z_\eta + r_\xi r_\eta)z_\eta \\ & + r_{\xi\xi}(z_\eta^2 + r_\eta^2)z_\eta \\ & + r_{\eta\eta}(z_\xi^2 + r_\xi^2)z_\eta \\ & + \frac{J}{r}z_\xi r_\eta z_\eta \\ & - \frac{J}{r}z_\xi r_\eta z_\eta.\end{aligned} \tag{B.35}$$

Now adding equation (B.35) to equation (B.34b) gives

$$\begin{aligned}
0 =& z_{\xi\xi}(z_\eta^2 + r_\eta^2)(r_\xi - r_\eta) \\
&- 2z_{\xi\eta}(z_\xi z_\eta + r_\xi r_\eta)(r_\xi - r_\eta) \\
&+ z_{\eta\eta}(z_\xi^2 + r_\xi^2)(r_\xi - r_\eta) \\
&- \frac{J}{r} z_\xi (z_\eta)(r_\xi - r_\eta) \\
&- r_{\xi\xi}(z_\eta^2 + r_\eta^2)(z_\xi - z_\eta) \\
&+ 2r_{\xi\eta}(z_\xi z_\eta + r_\xi r_\eta)(z_\xi - z_\eta) \\
&- r_{\eta\eta}(z_\xi^2 + r_\xi^2)(z_\xi - z_\eta) \\
&+ \frac{J}{r} z_\xi (r_\eta)(z_\xi - z_\eta).
\end{aligned} \tag{B.36}$$

Separating out expressions for z and r gives

$$\begin{aligned}
0 =& z_{\xi\xi}(z_\eta^2 + r_\eta^2)(r_\xi - r_\eta) \\
&- 2z_{\xi\eta}(z_\xi z_\eta + r_\xi r_\eta)(r_\xi - r_\eta) \\
&+ z_{\eta\eta}(z_\xi^2 + r_\xi^2)(r_\xi - r_\eta) \\
&- \frac{J}{r} z_\xi (z_\eta)(r_\xi - r_\eta)
\end{aligned} \tag{B.37a}$$

$$\begin{aligned}
0 =& - r_{\xi\xi}(z_\eta^2 + r_\eta^2)(z_\xi - z_\eta) \\
&+ 2r_{\xi\eta}(z_\xi z_\eta + r_\xi r_\eta)(z_\xi - z_\eta) \\
&- r_{\eta\eta}(z_\xi^2 + r_\xi^2)(z_\xi - z_\eta) \\
&+ \frac{J}{r} z_\xi (r_\eta)(z_\xi - z_\eta).
\end{aligned} \tag{B.37b}$$

Dividing out common terms leaves

$$\begin{aligned}
0 =& z_{\xi\xi}(z_\eta^2 + r_\eta^2) \\
&- 2z_{\xi\eta}(z_\xi z_\eta + r_\xi r_\eta) \\
&+ z_{\eta\eta}(z_\xi^2 + r_\xi^2) \\
&- \frac{J}{r} z_\xi (z_\eta)
\end{aligned} \tag{B.38a}$$

$$\begin{aligned}
0 =& - r_{\xi\xi}(z_\eta^2 + r_\eta^2) \\
&+ 2r_{\xi\eta}(z_\xi z_\eta + r_\xi r_\eta) \\
&- r_{\eta\eta}(z_\xi^2 + r_\xi^2) \\
&+ \frac{J}{r} z_\xi (r_\eta).
\end{aligned} \tag{B.38b}$$

After final rearranging, we are left with

$$z(\xi,\eta) \equiv \alpha z_{\xi\xi} - 2\beta z_{\xi\eta} + \gamma z_{\eta\eta} = \frac{J}{r} z_\xi z_\eta \tag{B.39a}$$

$$r(\xi,\eta) \equiv \alpha r_{\xi\xi} - 2\beta r_{\xi\eta} + \gamma r_{\eta\eta} = \frac{J}{r} z_\xi r_\eta, \tag{B.39b}$$

where again (repeated for convenience),

$$\alpha = z_\eta^2 + r_\eta^2 \tag{B.40a}$$

$$\beta = z_\xi z_\eta + r_\xi r_\eta \tag{B.40b}$$

$$\gamma = z_\xi^2 + r_\xi^2 \tag{B.40c}$$

$$J = z_\xi r_\eta - z_\eta r_\xi. \tag{B.40d}$$